UNIVERSIDAD Ð LA LAGUNA
Departamento de Astrofísica

Universidad de La Laguna

Search and characterization of exo-Earths orbiting solar-type stars

Memoria que presenta
Don Borja Toledo Padrón
para optar al grado de
Doctor por la Universidad de La Laguna

INSTITUTO Ð ASTROFISICA Ð CANARIAS
agosto de 2021

Examination date: Octubre, 2021
Thesis supervisor: Dr. Jonay Isaí González Hernández

A mi hermano Altai,
mi vida es tuya.
A mis padres,
por habernos colmado de amor y cariño.

Abstract

An exoplanet is an astronomical object that orbits one or more stars different from the Sun and has a mass lower than that necessary to produce the thermonuclear fusion of deuterium. Among the variety of techniques implemented to discover these objects, one of the most reliable is the radial velocity (RV) method. This technique is based on measuring the Doppler effect experienced by the spectral lines of a star, searching for signals caused by the gravitational field of a planet. The search of low-mass exoplanets through this technique requires high-resolution spectrographs such as HARPS or CARMENES, that achieve an RV precision around 1 $\mathrm{m\,s^{-1}}$, or ESPRESSO, which provides an improved RV precision up to 10 $\mathrm{cm\,s^{-1}}$. The RV precision will determine the minimum amplitude of the planetary signals that can be detected by the instrument, and therefore, the mass of the possible planetary companions.

The wavelength calibration of the spectrographs is key to take advantage of the resolution and stability of these instruments and thus be able to maximize the precision limit. Currently, the Laser Frequency Comb (LFC) is considered one of the most accurate calibration systems, providing a short-term repeatability of 1 $\mathrm{cm\,s^{-1}}$ through a regular pattern of spectral lines referred to an atomic clock.

Regardless of the RV precision achieved, the detection of planetary signals is hampered by the short-term and long-term stellar activity signals. The former are caused by the stellar rotation along with the presence of spots and plages in the stellar surface, while the latter are related to the magnetic cycle of the star. The modeling and subtraction of these signals are fundamental to detect and characterize correctly the planetary signals, especially in M dwarfs, in which the periodicity of the short-term activity signals is compatible with the habitable zone of these stars, where liquid water could potentially exist on the surface of a planet. To distinguish which is the origin of the RV signals detected, different chromospheric activity indicators are used, along with relations between the

stellar rotation and other properties of the star.

In this thesis, we develop a calibration pipeline for the LFC in order to achieve the most precise wavelength solution possible. We compare the LFC results with those obtained by a ThAr lamp (the most commonly used calibration instrument) using more than nine thousand HARPS spectra from the LFC commissioning and previous testing campaigns. The pipeline includes an RV calculation module that allows the user to self-build Cross-Correlation Functions (CCFs) using different stellar masks. We perform an RV accuracy study comparing our results with those reported by NASA's Jet Propulsion Laboratory (JPL), and finally broaden the module's availability to other spectrographs.

We contribute to the HADES (HArps-n red Dwarf Exoplanet Survey) and RoPES (Rocky Planets in Equatorial Stars) programs, which are focused on the search and characterization of rocky exoplanets with the ultimate goal of detecting Earth-like planets in the habitability zone. The first program is based on a sample of 79 M dwarfs observed with HARPS-N, while the second one contains a sample of 30 G- and K-type stars observed with HARPS-N and HARPS with the aim of taking advantage of the LFC features in this last spectrograph. We conducted a stellar activity study of the sample from both programs. The most prolific is the one carried out on Barnard's Star (the closest single star to the Solar system) based on a 15 yr dataset coming from eight different spectrographs and four photometric sources. We computed different activity indicators to characterize the rotation of the star (including its differential rotation) and its long-term magnetic cycle, both being key elements for the discovery of the first planetary companion detected around this star. The analyses of the remaining stars served to cross-correlate the detection of 33 new rotation signals and 18 new cycle signals within the M-type star sample.

The detailed stellar activity analysis of the star sample considered in this thesis led to the discovery of a super-Earth around the M-dwarf GJ 740 using HARPS-N and CARMENES data. The planet has a minimum mass of $2.96^{+0.50}_{-0.48}$ $M_\oplus$, it is located at $0.029^{+0.001}_{-0.001}$ AU from its parent star, and presumably has a rocky composition. Additionally, we contributed to the detection of eight other new exoplanets around seven different stars from our sample: GJ 625 b, GJ 3942 b, Gl 15 A c, Gl 686 b, Gl 49 b, GJ 685 b, HD 176986 b, and HD 176986 c.

The extremely high RV precision provided by the new-generation spectrograph ESPRESSO has expanded the limits to reach planetary signals with lower amplitudes. We combine ESPRESSO spectroscopy with K2 photometry to characterize the two-planet system orbiting the K2-38 star, in one of the first published works within the ESPRESSO GTO. We find that K2-38 b is an

iron-rich super-Earth with a size of 1.54 ± 0.14 $R_\oplus$ and a mass of $7.3^{+1.1}_{-1.0}$ $M_\oplus$ (and therefore, one of the greatest densities reported to date) while K2-38 c is a rocky sub-Neptune with an H2 envelope that has a 2.29 ± 0.26 $R_\oplus$ and a mass of $8.3^{+1.3}_{-1.3}$ $M_\oplus$. Each planet is located on each side of the radius valley (a region that lacks detected planets because of photoevaporation effects) due to the different irradiation levels and evaporation processes that they are exposed to, along with core-powered mass-loss mechanisms.

Resumen

Un exoplaneta es un objeto astronómico que orbita una o más estrellas diferentes al Sol y tiene una masa menor a la necesaria para producir la fusión termonuclear del deuterio. Entre la variedad de técnicas que se han implementado para descubrir estos objetos, una de las más fiables es el método de velocidad radial (RV). Esta técnica se basa en medir el efecto Doppler que experimentan las líneas espectrales de una estrella, buscando señales provocadas por el campo gravitatorio de un planeta. La búsqueda de exoplanetas de baja masa mediante esta técnica requiere espectrógrafos de alta resolución como HARPS o CARMENES, que alcancen una precisión en RV en torno o superior a 1 $\mathrm{m\,s^{-1}}$, o ESPRESSO, que proporciona una precisión en RV mejorada de hasta 10 $\mathrm{cm\,s^{-1}}$. La precisión en RV determinará la amplitud mínima de las señales planetarias que se puedan detectar con el instrumento y, por tanto, la masa de los posibles compañeros planetarios.

La calibración en longitud de onda de los espectrógrafos es clave para aprovechar la resolución y estabilidad de estos instrumentos y así poder maximizar la precisión límite. Actualmente, el Laser Frequency Comb (LFC) es considerado uno de los sistemas de calibración más precisos, ya que proporciona una repetibilidad a corto plazo de 1 $\mathrm{cm\,s^{-1}}$ a través de un patrón regular de líneas espectrales referidas a un reloj atómico.

Independientemente de la precisión en RV alcanzada, la detección de señales planetarias se ve obstaculizada por las señales de actividad estelar a corto y largo plazo. Las primeras son provocadas por la rotación estelar así como la presencia de manchas y plagas en la superficie estelar, mientras que las segundas están relacionadas con el ciclo magnético de la estrella. El modelado y sustracción de estas señales son fundamentales para detectar y caracterizar correctamente las señales planetarias, especialmente en enanas rojas, en las que la periodicidad de las señales de actividad a corto plazo es compatible con la zona habitable de estas estrellas, donde potencialmente podría existir agua líquida

en la superficie de un planeta. Para distinguir cuál es el origen de las señales detectadas en RV se utilizan distintos indicadores de actividad cromosférica, así como relaciones entre la rotación estelar y otras propiedades de la estrella.

En esta tesis desarrollamos una pipeline de calibración para el LFC con el fin de alcanzar la solución de longitud de onda más precisa posible. Comparamos los resultados del LFC con los obtenidos por una lámpara ThAr (el instrumento de calibración más utilizado) usando más de nueve mil espectros de HARPS provenientes del commissioning del LFC y de campañas de prueba anteriores. La pipeline incluye un módulo para el cálculo de RV que permite al usuario autoconstruir funciones de correlación cruzada (CCF) utilizando diferentes máscaras estelares. Realizamos un estudio de precisión de RV comparando nuestros resultados con los reportados por el Jet Propulsion Laboratory (JPL) de la NASA, y finalmente ampliamos la disponibilidad del módulo a otros espectrógrafos.

Contribuimos a los programas HADES (HArps-n red Dwarf Exoplanet Survey) y RoPES (Rocky Planets in Equatorial Stars), los cuales se centran en la búsqueda y caracterización de exoplanetas rocosos con el objetivo final de detectar planetas similares a la Tierra en la zona de habitabilidad. El primer programa se basa en una muestra de 79 enanas M observada con HARPS-N, mientras que el segundo contiene una muestra de 30 estrellas de tipo G y K observada con HARPS-N y HARPS con el objetivo de aprovechar las características del LFC en este último espectrógrafo. Realizamos un estudio de actividad estelar de la muestra de ambos programas. El más prolífico es el llevado a cabo sobre la estrella de Barnard (la estrella individual más cercana al sistema Solar) basado en un conjunto de datos de 15 años procedente de ocho espectrógrafos diferentes y cuatro fuentes fotométricas distintas. Calculamos diferentes indicadores de actividad para caracterizar la rotación de la estrella (incluyendo su rotación diferencial) y su ciclo magnético a largo plazo, siendo ambos elementos clave para el descubrimiento del primer planeta detectado alrededor de esta estrella. Los análisis de las estrellas restantes sirvieron para confirmar la detección de 33 nuevas señales de rotación y 18 nuevas señales de ciclo dentro de la muestra de estrella tipo M.

El análisis detallado de actividad estelar de la muestra de estrellas consideradas en esta tesis llevó al descubrimiento de una súper-Tierra alrededor de la enana roja GJ 740 usando de datos de HARPS-N y CARMENES. El planeta tiene una masa mínima de $2.96\ ^{+0.50}_{-0.48}\ M_\oplus$, se encuentra ubicado a $0.029\ ^{+0.001}_{-0.001}$ AU de su estrella progenitora y presumiblemente tiene una composición rocosa. Adicionalmente, contribuimos a la detección de otros ocho nuevos exoplanetas alrededor de siete estrellas diferentes de nuestra muestra: GJ 625 b, GJ 3942 b, Gl 15 A c, Gl 686 b, Gl 49 b, GJ 685 b, HD 176986 b y HD 176986 c.

La precisión extremadamente alta en RV proporcionada por el espectrógrafo de nueva generación ESPRESSO ha expandido los límites para alcanzar señales planetarias de amplitud baja. Combinamos la espectroscopia de ESPRESSO con la fotometría de K2 para caracterizar el sistema de dos planetas que orbita la estrella K2-38, en uno de los primeros trabajos publicados dentro del GTO de ESPRESSO. Encontramos que K2-38 b es una súper-Tierra rica en hierro con un tamaño de 1.54 ± 0.14 $R_\oplus$ y una masa de $7.3^{+1.1}_{-1.0}$ $M_\oplus$ (y por lo tanto, una de las densidades planetarias más grandes reportadas hasta la fecha), mientras que K2-38 c es un sub-Neptuno rocoso con una envoltura de H2 que tiene 2.29 ± 0.26 $R_\oplus$ y una masa de $8.3^{+1.3}_{-1.3}$ $M_\oplus$. Cada planeta está ubicado a cada lado del radius valley (una región que carece de planetas detectados debido a efectos de fotoevaporación) por los diferentes niveles de irradiación y procesos de evaporación a los que están expuestos, junto con otros mecanismos de pérdida de masa.

Contents

1

Introduction

Granted, then, that empty space extends without limit in every direction and that innumerable seeds are rushing on countless courses through an unfathomable universe... it is in the highest degree unlikely that this earth and sky is the only one to have been created
Lucretius (99–55 B.C.)

1.1 Historical evolution of the exoplanetary science

The fundamental question regarding the meaning of the human race's existence within the universe has always brought with it speculations about the presence of other worlds similar to ours. In the times of ancient Greece, philosophers like Epicurus (341–270 BC) theorized about the possibility of the existence of other planets aside from the Earth. This view of the universe contrasts with the one provided by Aristotle (382–322 BC), who despite his reasoning about the possibility of the existence of other worlds, did not accommodate this idea within the geocentric conception that was held at that time.

This conception of the Earth as the only planet in the universe would be the dominant model during the next millennium. Throughout this period some important figures such as the theologian Alberto Magno (1193–1280) and his disciple Thomas Aquinas (1295–1358) raised the importance of this question as an object of study, while others like the French Jean Buridan (1295–1358), rector of the University of Paris, or the Englishman William of Ockam (1280–1347), a Franciscan friar and philosopher of great renown, kept alive the idea

of a plurality of worlds in the universe.

In the 16th century, the vision of the universe changed drastically with the publication of *De revolutionibus orbium coelestium* written by Nicholas Copernicus (1473–1543) in 1543. His work denied the geocentric theory held at the time, shifting the Earth from the center of the universe. This vision was expanded by one of the greatest visionaries of exoplanetology, Giordano Bruno (1548–1600), with the publication of his dialogue *De l'infinito universo e mondi* in 1584. In this book, Bruno proposed revolutionary ideas such as that the universe was infinite or that the stars were distant suns with "innumerable worlds" orbiting around them that could contain life.

The heliocentric view of the Universe was slowly gaining acceptance throughout the next century with the arrival of the first refractor telescope (based on lenses) and the works based on observations of Tycho Brahe (1546–1601), Galileo Galilei (1564–1642), and Johannes Kepler (1571–1630), which theorized about the habitability of the Moon and the satellites of Jupiter that Galileo had discovered. However, these ideas continued facing rejection from the majority of society. In 1644, the French physicist and mathematician René Descartes equates the Sun with other stars in his work *Principia Philosophiae*; an idea that was spread by the French philosopher and writer Bovier de Fontenelle (1657–1757) in his book *Entretiens sur la pluralité des mondes*, taking these similarities one step further by proposing the existence other planetary systems.

The arrival of the first reflecting telescope (based on mirrors) and the publication of *Philosophiae Naturalis Principia Mathematica* by Isaac Newton (1642–1727) in 1687, supposed the demonstration of the Copernican theory through the Laws of Universal Gravitation. This opened the door for theories about the formation of the Solar system and its planets such as that published by Immanuel Kant (1724–1804) in his work *Allgemeine Naturgeschichte und Theorie des Himmels*, which pointed to the collapse of a rotating gas and dust nebula as the cause of the formation of the planets that were known at that time. This model was ratified by Pierre-Simon de Laplace (1749–1807) in his book *Exposition du Système du Monde* published in 1796, where the generally accepted basis of planetary formation modeling is exposed.

In the 19th century, the scientific community reinforced the concept of positioning the Earth in a galaxy full of stars that, like the Sun, must have planets in orbit. At that time the first large telescopes began to appear, such as the Leviathan, a 1.83-meter aperture reflector telescope built by the Irish Lord Rosse, or the large refractor telescope of the Yerkes Observatory, built in 1879 as an initiative of the American astronomer George Ellery Hale. These and other telescopes were used for planetary searches through the study of orbit

anomalies, which produced the discovery of Neptune at the beginning of the century. Around that time, the first statements of exoplanet detections were made. These claims would be proven wrong shortly after, showing that the cutting-edge astronomical instrumentation of the time was not enough to carry out the ambitious scientific discovery of finding another planet outside the Solar system.

At the beginning of the 20th century, the idea that there are other worlds orbiting the rest of the stars in the universe was generally accepted, but the astrophysics community would still need to detect one of these planets outside the Solar system to prove this hypothesis correct and study if these objects could sustain life similar to the one present on Earth.

1.2 State of the art: Techniques and instrumentation

In order to overcome the barrier related to the relatively weak stellar changes produced by a planet and its proximity to its progenitor star, several construction projects of different telescopes (with a diameter within the range of 8–10 meters) were launched in the last half of the last century. The persistent search of exoplanets using this technology led to the discovery of the first planet outside the Solar system detected in the visible range of the electromagnetic spectrum in 1995: 51 Pegasi b (Mayor & Queloz 1995). Three years priors to this detection, two planets were also reported orbiting the pulsar PSR 1257+12 based on observations performed with the Arecibo radio telescope (Wolszczan & Frail 1992), and a third companion was reported in 1994 (Wolszczan 1994). These detections were preceded by the publication of a possible planet orbiting the star HD 114762 in 1989 (Latham et al. 1989), which was first considered as a low-mass star, and years later revealed as an extrasolar planet.

The discovery of 51 Pegasi b made a great impact on the social perception of the universe since this extrasolar planet was orbiting a G2-type star very similar to our Sun. This publication established the initial landmark for the modern exoplanetary race to search and characterize these objects with the final goal of detecting a habitable Earth-like planet. To achieve this goal, several detection techniques have been developed and improved to seize the instrumental advances carried out through the years.

1.2.1 Astrometry

The first detection method developed for exoplanetary searches is based on measuring the position of the stars in the celestial vault and its variation over time. The astrometry studies offer an indirect way to detect exoplanets since their presence is reflected on the proper motion of the star (i.e., oscillations of its position around a fixed point). This method poses a two-body problem with the center of mass around which both the planet and its star rotate as a reference. In the case of the Sun, its mass constitutes 99.8 % of the total mass of the Solar system, placing it in a very close position to the reference point previously mentioned. The more massive stars are linked to smaller planetary orbits, which makes it easier to detect planets around low-mass stars because they are more easily displaced by the planets that revolve around them.

One of the main problems of this method is the high precision and the large amount of observing time necessary to obtain a significant detection. This adds to the requirement to have an orbital inclination different from 0° since in this case the angular displacement of the star caused by an exoplanet cannot be captured from the Earth. The higher the orbital inclination, the easier it is to find possible exoplanet candidates through this technique.

Two of the most important sources of data available to study the existence of exoplanets through this method are the satellite *Hipparcos* (HIgh Precision PARallax COllecting Satellite, Perryman et al. 1997) of the European Space Agency (ESA), which operated between 1989 and 1993, measuring the position of 100 000 stars with a precision of 0.002", and the *Gaia* spacecraft (Global Astrometric Interferometer for Astrophysics, Gaia Collaboration et al. 2016), also launched by ESA in 2013, which increases the precision achieved by *Hipparcos* by a factor of 100. Only with space telescopes of these characteristics, it is possible to achieve sufficient spatial resolution to achieve the detection of extrasolar planets using this method (Fig. 1.1).

FIGURE 1.1— **Left:** *Hipparcos* satellite. **Right:** *Gaia* satellite.

So far, only two planets have been discovered by the use of the technique (Muterspaugh et al. 2010; Curiel et al. 2020). The main application of this method is to confirm the presence of other planets already detected through other techniques, due to the difficulties it presents and the excessive time required.

1.2.2 Direct imaging

The next technique used in exoplanetary searches is based on detecting the stellar light reflected by the planet in the different ranges of the electromagnetic spectrum. This is the technique that provides the most information between all the methods but presents the great drawback of only being applicable to stars located at small distances from the Earth. This is due to the limitation imposed by the maximum resolution of the telescopes since the angular separation between the planet and the star decreases inversely with the distance from which both are observed.

Another problem is the large difference in brightness between the planets and the stars around which they orbit. In the case of Jupiter, the planet reflects 70 % of the light that comes from the Sun, which is equivalent in luminosity to 10^{-9} $L_\odot$, meaning that Jupiter is a billion times fainter than the Sun within the visible range (in the infrared the difference is reduced to 10^{-6} $L_\odot$). For this reason, the best candidates to be detected with this method are giant planets with a size similar to Jupiter that orbit at a great distance from their host star. Moreover, the detection of exoplanets with high orbital inclination is favored since their entire orbit can be tracked from the Earth without any planetary transit.

The brightness difference problem is solved by the use of coronagraphs, elements which role in the instrumental design is to block the light from the star that is not reflected by the planet. Initially created to block light from the solar photosphere, their incorporation into the search for exoplanets has allowed the detection of planets a million times fainter than their host star. Another key element in the case of ground-based direct imaging detections is the use of adaptative optics to correct the distortion produced by the Earth's atmosphere. This instrumental feature was key for the study of HR 8799, a young F0-type main-sequence star with four directly imaged giant planets detected in 2008 (Marois et al. 2008) and 2010 (Marois et al. 2010) (Fig. 1.2).

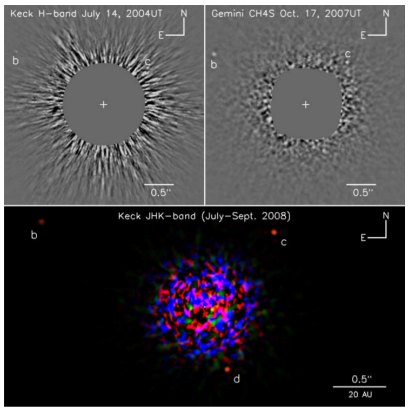

FIGURE 1.2— Direct imaging observations of HR 8799 taken with the Keck and Gemini telescopes. The final processing of the data reveals the presence of planets b, c, and d. Figure taken from Marois et al. (2008).

Apart from the stellar radiation reflected by the planet, internal sources of energy must be taken into account such as the one related to the radiative decay of unstable elements (negligible in giant planets composed mainly of H and He). Another energy contribution comes from gravitational contraction, which produces losses of potential energy in the form of heat.

As for the instruments built specifically for this method, the Gemini Planet Imager (GPI) for the Gemini Sur telescope located in Chile can be highlighted (Graham et al. 2007). This instrument makes it possible to achieve high contrast at small angular separations to obtain direct integral field images of extrasolar planets around nearby stars. Another notable instrument is the Spectro-Polarimetric High-contrast Exoplanet REsearch (SPHERE) of the Very Large Telescope (VLT), also located in Chile (Beuzit et al. 2008). This facility provides the highest contrast for direct images of planets obtained so far, allowing the distinction between exoplanets and their host star, thanks to the use of a coronagraph, adaptive optics, and differential imaging (many short-time exposure images reveal weak sources of light in terms of their color and polarization).

The first exoplanet detected using this technique was 2M1207 b, through a study in the infrared range performed with the VLT and published in 2004 (Chauvin et al. 2004). To date, the number of planets detected by this method

amounts to 53 [1], which is a low number compared to the discoveries carried out through other methods. The construction of the Extremely Large Telescope (ELT) by the European Southern Observatory (ESO) in the Atacama Desert, Chile, is expected to produce a significant increase in this quantity with its 39m diameter. This diameter will allow the detection of Earth-like planets in orbits similar to the one that characterizes the Earth. Regarding space missions, it is important to mention the next great space mission launched by NASA: the James Webb Space Telescope (JWST). Successor to the Hubble and Spitzer telescopes (which cover the visible/ultra-violet and infrared part of the spectra, respectively), the JWST is scheduled to be launched in 2021, allowing to perform a broad variety of studies across different fields of astrophysics in the mid-infrared range of the spectra. Its coronographs will enable the direct imaging of exoplanets in this range, making it possible to observe regions that are obscured by gas and dust in the visible spectrum.

1.2.3 Gravitational microlensing

The gravitational microlensing effect consists of the deflection experimented by the light from a distant star, when it encounters the gravitational field of another massive object that acts as a lens, magnifying the light from the star (the prefix micro refers to the fact that this object mass does not exceed 100 $M_\oplus$). This occurs due to the curvature of space-time produced by a compact object, as predicted by the general theory of relativity (Einstein 1916). The effect is noticeable for a short period of time, of several days or weeks, due to the Earth's translation. If the object that acts as a lens is the host star of some exoplanet, an additional increase is appreciated due to the presence of that planet (Fig. 1.3).

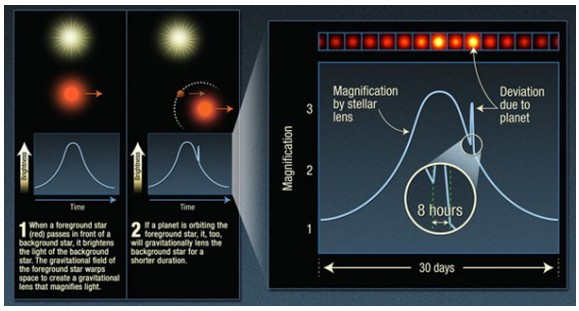

FIGURE 1.3— Scheme of the gravitational microlensing effect produced by an exoplanet. Credits: NASA, ESA, and K. Sahu (Space Telescope Science Institute in Baltimore).

[1] source: `https:/exoplanets.nasa.gov/`

This technique requires monitoring a large number of stars to determine precisely the exact contribution of an exoplanet. For this reason, this is the best method for the detection of exoplanets that are located near the center of the galaxy, which offers a large number of background stars. Finally, it must be taken into account that this effect is more appreciable in low-mass stars with giant planets orbiting around them.

This method presents the main advantage of being able to detect planets with very wide orbits located at a great distance (up to several kiloparsecs) from the Solar system, which carries the disadvantage that other techniques cannot be used to verify these discoveries. Another disadvantage is the requirement of alignment between the star and the object that acts as a lens so that the desired magnification can be detected. The probability of this happening is quite low because the size of a star is very small compared to interstellar distances. An additional drawback is that this effect is a short-term event that does not repeat itself in a long period of time due to the relative motion of the stars. Furthermore, it is only possible to detect planets located within the zone of action of the microlens, which corresponds to a distance of 1–4 AU.

The disadvantages of this technique explain the low number of exoplanets discovered up to date (108 in total) in comparison with other techniques such as radial velocity or transits, which have a much higher success rate.

The data used in this method usually come from observations made with a network of robotic telescopes. Of these networks, the PLANET (Probing Lensing Anomalies NETwork) stands out as one of the most ambitious (Albrow et al. 1996), composed of five telescopes distributed throughout the Southern hemisphere, allowing the first exoplanet detection based on the gravitational microlensing effect in 2006 (Beaulieu et al. 2006). Observations of this phenomenon not only focus on the search for exoplanets but also serve to discover other objects such as brown dwarfs or to study the effects of dark matter, among many other applications.

1.2.4 Planetary transits

The planetary transits search is one of the most popular methods used for exoplanetary detections. This technique requires a photometric study of the star in order to detect periodic variations in its brightness, which correspond to the eclipses produced by a planet when it is passing in front of the star (the planet blocks a part of the light emitted by the star depending on its size). In the case of having a planetary companion, the light curve of the host star will show a decrease in flux with a periodicity according to the period of translation of the planet, a duration that will depend on its speed, and a depth related to

its size (Fig. 1.4 and Eq. 1.1).

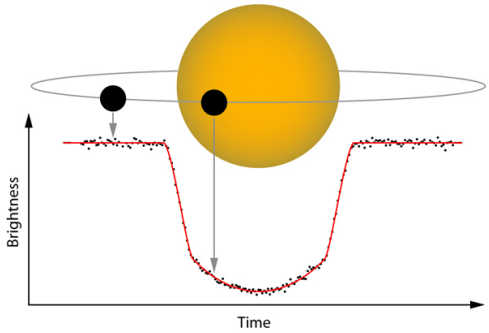

FIGURE 1.4— Flux variation produced by the transit of a planet.

$$R_{\mathrm{p}} = R_{\star}\sqrt{\frac{\Delta F}{F}} \tag{1.1}$$

These studies allow the determination of the size of the planet by measuring the depth of the transit and knowing the size of its parent star (Eq. 1.1). In addition to the planetary radius, this method makes it possible to obtain other characteristic parameters of the planet, such as its orbital inclination (related to the impact parameter), its orbital speed, or the semi-major axis of the orbit.

The first discovery of an extrasolar planet using this method was HD 209458 b (Charbonneau et al. 2000), a planet in the constellation of Pegasus discovered in 2000 that had already been detected by the Doppler effect produced by the gravitational disturbances of the planet on its star (Henry et al. 2000).

In 2006, the CoRoT (COnvection ROtation et Transits planétaires) satellite was launched (Baglin et al. 2006). This was the first space telescope dedicated mainly to the search for exoplanets. It aimed to study 120 000 stars through its 27 cm diameter mirror and 4 built-in CCD detectors, and it was capable of exploring stellar interiors to study the acoustic waves that propagate across the surface (astroseismology). This space mission was approved and led by the French Space Agency (CNES), with an operational phase between 2007 and 2012, that led to 27 confirmed exoplanets and hundreds of potential candidates. Among the great milestones of this mission is the discovery of the first Earth-sized planet in 2009, CoRoT-7b, something unattainable until then (Léger et al. 2009).

The next main instrumental reference for this method and one of the biggest advances in exoplanetary science was the *Kepler* space telescope (Borucki et al. 2010). Launched by NASA in 2009 within the Discovery plan, the *Kepler* telescope was the CoRoT successor and was especially revolutionary for its capacity to detect Earth-size planets in the habitable zone. This satellite analyzed the brightness of stars located between the constellations of the Swan and Lyra (at a distance between 600 and 3 000 light-years), searching for planetary transits. It allows detecting variations in the luminosity of the star of up to 0.0020 % thanks to its 95-megapixel detector (21 modules with 2 CCDs of 2200x1024 pixels each), the most powerful launched into space up to that date. This space mission nominally stopped operating in 2013 due to errors in the gyroscopes in charge of stabilizing the satellite. With the data taken during that period of time, the *Kepler* telescope allowed researchers to confirm the existence of 2 793 new confirmed exoplanets, along with 3 255 possible candidates. This represents 65 % of the total number of extrasolar planets confirmed to date, which makes this telescope the most successful instrument within the research field of exoplanetary searches.

The last major step in the instrumental development related to transit searches came in 2018 with the arrival of the space telescope TESS (Transiting Exoplanet Survey Satellite, Ricker et al. 2015). This satellite aims to monitor more than 200 000 stars searching for temporary drops in the stellar flux caused by planetary transits. The two-year observation plan of the nominal mission divided the sky into 26 segments and scheduled them in two annual campaigns of 13 segments each, observing the segments of the Northern hemisphere in the first year and the segments of the Southern hemisphere in the second one. This is translated into a 27.4-day observing period per segment, which makes this satellite mostly sensitive to exoplanets with an orbital period shorter than 13 days (allowing to detect at least two transits per planet). The four cameras installed in the telescope record the photometry of the target stars every 2 minutes with a 50 ppm photometric precision on stars with a TESS magnitude between 9 and 15. Full-frame images from the entire field of view of the telescope are delivered with a 30-minute cadence, providing simultaneous information from millions of stars. The TESS Input Catalog (TIC, Stassun et al. 2018) contains over 1 billion objects, from which the scientific team expects to detect 50 exoplanets with $R < 4\ R_{\oplus}$. Although the prime mission ended in 2020, NASA has extended the mission for another two years, in which the full-frame images will be delivered with a shorter cadence of 10 minutes, as well as a new 20-second cadence mode. So far, 91 planets have been confirmed through the use of TESS data, with nearly 2 100 candidates yet to be confirmed.

Finally, it is important to highlight the role of CHEOPS (CHaracterising

ExOPlanet Satellite) as a source of high precision transit measurement of bright and nearby stars that are known to host planets. Launched by ESA in 2019, the main targets of the mission are super-Earth and Neptune-size planets, and its first results are being published during this year 2020 (Lendl et al. 2020).

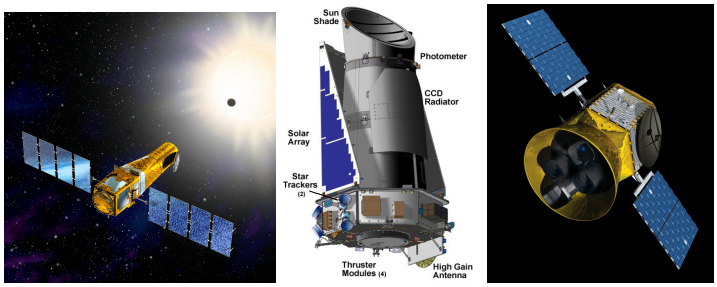

FIGURE 1.5— **Left:** CoRoT satellite. **Center:** *Kepler* satellite. **Right:** TESS.

All of these space missions are complemented by ground-based surveys specialized in search of planetary transits. Between these surveys, the ASAS, MEarth, and SuperWASP projects are noteworthy. ASAS (All Sky Automated Survey, Pojmanski 1997) consists of two automated observing stations at Las Campanas Observatory, Chile (ASAS-S or ASAS-3), and Haleakalā Observatory, USA (ASAS-N or ASAS-3N). These two stations observe simultaneously in the V and I photometric bands with an average accuracy of ~ 0.05 mag per exposure. They are complemented with the ASAS-SN (All-Sky Automated Survey for Supernovae) project (Shappee et al. 2014), which consists of 20 telescopes distributed around the globe that are automatically surveying the entire available sky every night down to $V \sim 17$ mag.

The MEarth project (Berta et al. 2012) is an American robotic observatory that searches for planets in transit around red dwarfs (small, cool main sequence stars) using two arrays of eight 40-centimeter Ritchet Chrétien telescopes located at the Fred Lawrence Whipple Observatory (USA) and Cerro Tololo Inter-American Observatory (Chile). The SuperWASP (Wide Angle Seach for Planets) program is another important survey performing a massive automated search for extrasolar planets through the transit method (Pollacco et al. 2006). This project counts with two robotic observatories at the Roque de los Muchachos Observatory (Northern hemisphere) and the South African Astronomical Observatory (Southern hemisphere), which reported their first discoveries in 2007 (Collier Cameron et al. 2007).

The biggest advantage presented by this method is that it does not depend on the distance between the planet and the star. In addition, it allows characterizing the atmosphere of a planet (combining it with spectroscopic observations), and it is very useful for detecting large-size exoplanets. However, it has the disadvantage that in order to observe planetary transits it is necessary that the orbital inclination seen from Earth is approximately 90° (something that only occurs in 10 % of planets with small orbits, and the percentage decreases as the orbit increases). Another disadvantage is the high number of false detections produced by the method (in the CoRoT telescope, the false positive rate is 83 %, Almenara et al. 2009), so a second confirmation is necessary through another detection technique.

The success rate of the transit method is the highest among all the techniques, mainly due to the large number of discoveries made by the *Kepler* mission. The current number of exoplanets discovered by transits ascend to 3 336 (the 76 % of the total number of confirmed detections). This number is expected to increase with the launch of PLATO (PLAnetary Transits and Oscillations of stars) in 2026 by the ESA. The main goal of this telescope is the detection of Earth-like planets located in the habitable zone of solar-type stars, allowing unprecedented precision in the planetary radii determination, along with new studies of stellar oscillations. One of the main incentives of this satellite will be the possibility to perform planetary searches on bright stars (with magnitudes between 4 and 11), and its sensitivity to longer period planets than the ones that TESS is able to detect.

1.2.5 Timing variations

The variation in the timing of planetary transits is an indicator of the presence of additional planets orbiting the target star. This is due to the gravitational effect between these planets which is translated into acceleration and deceleration in their orbit. These changes produce fluctuations in the transit length and orbital period which can be measured using the same facilities built for transit searches. This method allows the detection of non-transiting planets, and it is mainly used for confirming already known planets in multi-planetary systems. Up to date, 21 extrasolar planets have been discovered using this method.

It is worth mentioning two other methods based on studying the variations in some periodic phenomena which could indicate the presence of exoplanets.

The first method is based on studying pulsars. These objects are very compact neutron stars (about 20 km in diameter), which originate from the explosion of a star in the form of a supernova. Its magnetic field is so strong that it emits jets of radiation from the poles within the range of radio waves

in the electromagnetic spectrum. The rotation of the pulsar allows these jets to be measurable from Earth with a certain periodicity (which is very small, on the order of seconds). The presence of exoplanets around a pulsar produces slight variations in its rotation period due to their gravitational action.

The advantage of this technique is that it allows the detection of exoplanets with a mass ten times less than the Earth (it is the most accurate within all the methods in this regard). However, the low abundance of pulsars in our range of vision and their small size make this technique one of the least used for the search for exoplanets. Another major drawback is the low probability of having a planet rotating around a pulsar since the origin of these objects is the explosion of a star as a supernova, one of the most violent phenomena in the universe. Theoretically, planets located at close-in orbits should have disintegrated or displaced enormously from their orbit after the explosion. Nevertheless, a total number of 9 exoplanets have been found orbiting pulsars, which has generated a debate about their origin, putting the formation scenario where they formed after the supernova explosion as the most probable one. Among these planets, it is important to mention the first planetary system discovered outside the Solar system: a system of three planets orbiting the pulsar PSR-1257+12 (Wolszczan & Frail 1992; Wolszczan 1994). Finally, it must be taken into account that the planets detected by this method would not be habitable due to the high levels of radiation emitted by the pulsar.

The second method is based on the study of eclipsing binaries. In this type of systems, two eclipses can be detected between the two stars, a primary one (which happens when the star with the brightest surface is covered by the disk of the other star) and a secondary one (when the less bright star is the one that covers the brightest). The studies carried out using this technique are very similar to the ones performed in the transit method, but the variations in the flux of the star analyzed are much higher due to being caused by a companion star. In this case, the periodic phenomenon to observe are the times in which eclipses occur, looking for changes in them due to the presence of an exoplanet that produces shifts based on its orbit and mass. It is therefore important that the exoplanets that orbit the target binary are high-mass planets with close-in orbits, also being favorable that the mass of the stars that make up the binary system are low.

A great advantage of this technique over the transit method is that it detects planets that are further away from their host star. To date, 16 planets around binary stars have been discovered using the eclipse timing variation method. The first detection was achieved in 2009, with the discovery of the planet HW Vir (AB) b orbiting an eclipsing binary of the Algol type (in which there is only gravitational interaction without any matter exchange) (Lee et al. 2009).

1.3 The radial velocity method

Along with the transit searches, the radial velocity (RV) method has become the most popular technique for detecting extrasolar planets, allowing the discovery of a total number of 850 new exoplanets so far. Like the astrometric techniques, the radial velocity detection method relies on detecting motions in the exoplanet's host star. In this case, the changes experienced by the star are related to its velocity, instead of its position. The radial velocity of the stars can be measured through the Doppler effect experienced by the light they emit (the waves emitted by a target in relative motion with respect to a fixed observer vary in frequency, and therefore in wavelength). The radial displacement of a star along the line of sight produces changes in its spectral lines, as it approaches (blueshift) or moves away (redshift) from the observer (Fig. 1.6). This displacement can be affected by the gravitational pull made by exoplanets that orbit the target star, shifting the orbit of the star around the center of mass. The RV method allows the discovery of planetary companions by studying the periodic RV changes experienced by a star reflected on the shifts experienced by its spectral lines. Therefore, to apply this technique it is needed to measure the spectrum of the star with high precision.

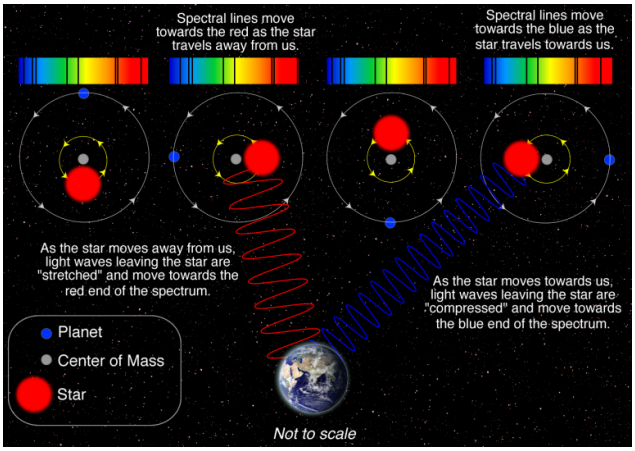

FIGURE 1.6— Schematic representation of the radial velocity variation that a star experiences when an exoplanet orbiting around it. The star is displaced from the center of mass of the system, and its spectrum is shifted with a certain periodicity. Credits: Las Cumbres Observatory.

Due to the high spectral resolution required to apply this method correctly, a very high signal-to-noise ratio is necessary, which puts a limit on the distance between Earth and the stars that can be studied. The limit also depends on the telescope. It is also important to consider that the Doppler spectrography can reveal signals due to stellar activity that are easily confused with planetary signals, as well as other types of signals characteristic of multi-planetary or multi-stellar systems. Giant planets in close-in orbits generate a greater Doppler shift in the spectral lines of the host star, while the signals related to low-mass planets located at a greater distance from their parent star are weaker and can be easily hidden by the noise or the signals related to stellar activity. This technique works better with late-type stars due to their lower masses, generally slower rotation (which results in narrower spectral lines), and lower stellar activity.

It must be taken into account that the use of this method requires a planetary orbital inclination different from 0°, since in that case no changes in the radial velocity of the host star can be observed (the closer to 90° the orbit of the planet is, the more noticeable the Doppler effect in the spectral lines of the star will be). Due to the high reliability of the detections made with this technique, the radial velocity method has become the main technique for verifying already known exoplanets. Through this method, the following planetary parameters can be obtained: the orbital period, mean distance to the star, eccentricity of its orbit, and lower limit of mass (the combination with the transit method provides the exact value of the planetary mass).

1.3.1 Current instrumentation

The instrumentation used by this method began to be developed between the end of the 80s and the beginning of the 90s. In 1993, the echelle ELODIE spectrometer, mounted on the 1.93-meter reflector telescope of the Haute-Provence Observatory in France, saw the first light (Baranne et al. 1996). This instrument was a key element in the detection of 51 Pegasi b in 1995 and the discovery of 12 other exoplanets for which only data exclusively from this spectrograph were used. ELODIE has contributed to the detection of another 20 exoplanets combining the information provided by this spectrometer with data from other instruments. In 1996, the HiRES (High Resolution Echelle Spectrometer) instrument started operating on the twin 10-meter Keck telescopes (the third-largest telescope after the Southern African Large Telescope and the Gran Telescopio de Canarias) at the Manua Kea Observatory in Hawaii (Vogt et al. 1994). Currently, this spectrograph has provided the second-largest contribution to exoplanetary discoveries among the spectrographs dedicated to

exoplanetary searches through the RV technique, with a total number of 261 detections. Two years later (in 1998), the CORALIE cross-scattering echelle spectrograph was installed at the Swiss 1.2-meter telescope of the La Silla Observatory, in Chile (Queloz et al. 2000), as an improved version of the ELODIE spectrometer. This instrument is powered by 2 fibers and includes an encoder that improves the stability related to the light captured by the spectrograph. CORALIE's contribution to the detection of exoplanets is the third highest within the RV method (117 extrasolar planets discovered with data from this spectrograph), along with several characterizations of exoplanets that were already detected by other techniques.

These 3 spectrographs are part of the so-called first generation of echelle spectrographs, characterized for achieving a radial velocity precision between 3 and 15 $\mathrm{m\,s^{-1}}$ (Pepe et al. 2014a). To illustrate the type of planets that can be detected with this precision, 51 Pegasi b and some planets of the Solar system are listed in Table 1.1 with their masses and RV changes they produced in their parent star over an orbital period along with other features of interest:

Table 1.1— Features of planets to be considered for their detection through RV measurements with high precision spectrographs.

Planet	**Mass** [$\mathbf{M_\oplus}$]	**a** [**AU**]	P_{orb}	**RV** [$\mathbf{m\,s^{-1}}$]
51 Peg b	150.02	0.05	4.23 d	55.9
Jupiter	317.83	5.20	11.86 yr	12.4
Gliese 581 c	5.40	0.07	12.92 d	3.18
Saturn	95.16	9.58	29.46 yr	2.75
Neptune	17.15	30.10	164.79 yr	0.281
Earth	1	1	365.26 d	0.089

Table 1.1 shows how only the first 3 planets could be detected with first-generation echelle spectrographs. This limitation prompted the instrumental development that led to the release of the high-precision echelle spectrograph HARPS (High Accuracy Radial velocity Planet Searcher, Mayor et al. 2003), the first second-generation echelle spectrograph. This spectrograph installed in the 3.6-meter telescope of the La Silla Observatory in Chile is currently the most used instrument for RV searches of exoplanets. Throughout the 17 years it has been operating, it has allowed the detection of an enormous amount of 262 exoplanets. In 2006, the SOPHIE (Spectrographe pour l'Observation des Phénomènes des Intérieurs stellaires et des Exoplanètes) spectrograph (Bouchy & Sophie Team 2006) was built as a substitute for ELODIE with the idea to

compete with HARPS from the Northern Hemisphere. Finally, in 2012 another second-generation echelle spectrograph appeared in the Northern Hemisphere of great relevance to this research field: HARPS-N (Cosentino et al. 2012). This spectrograph is installed in the Telescopio Nazionale Galileo of the Roque de los Muchachos Observatory and aims to complement the HARPS observations using practically the same characteristics. With these second-generation spectrographs an RV precision of $\sim 1\ \mathrm{m\,s^{-1}}$ can be achieved.

The culmination of the instrumental development related to the RV method comes in 2016 with the first light of the third-generation echelle spectrograph ESPRESSO (Echelle Spectrograph for Rocky Exoplanet and Stable Spectroscopic Observations). This instrument is an ultra-stable fiber-fed high-resolution spectrograph installed at the Very Large Telescope (VLT) in the Paranal Observatory, Chile (Pepe et al. 2014b; González Hernández et al. 2018; Pepe et al. 2021), which main goal is to detect and characterize Earth-like planets in the habitable zone of solar-like stars. Built as HARPS successor, ESPRESSO achieves a much better RV precision of a few $\mathrm{cm\,s^{-1}}$. Installed at the incoherent combined Coudé focus of the VLT, the instrument allows to carry out the observation in three different configurations. The first one is the High Resolution 1-UT mode, where one of the telescope units of the VLT is used. This mode allows a spectral resolution of $\mathrm{R} = 140\,000$ using an on-sky fiber of 1", which provides an RV precision of about 10 $\mathrm{cm\,s^{-1}}$ for very bright stars ($V \sim 3$–5). The second configuration is the Ultra High Resolution 1-UT mode, where the spectral resolution increased to $\mathrm{R} = 190\,000$ limiting the sky fiber to 0.5", but the target star needs to be brighter than in the High Resolution mode (the magnitude limit in the V filter decreases from 17 to 16) and the RV precision achieved can be worse (around 1 $\mathrm{m\,s^{-1}}$). The last configuration is the Medium Resolution 4-UT mode, where the four telescope units are used jointly to reach weaker stars (with a magnitude up to 20) with lower spectral resolution ($\mathrm{R} = 70\,000$). Fig. 1.7 shows the schematical view of this instrument along with previous spectrographs and Table 1.2 shows all the spectrographs that have allowed the RV detection of new exoplanets.

TABLE 1.2— Spectrographs used for the first detection of an exoplanet through the RV method.

Instrument	Telescope	Observatory	Country	Year	R	Exop.
AFOE	1.5m	Fred Lawrence Whipple	USA	1994	70000	6
BOES	1.8m	BOAO	Korea	2004	90000	20
CARMENES	3.5m	Calar Alto	Spain	2015	90000	14
CES	2.16m	Xinlong	China	2005	106000	3
CES	1.4m	La Silla	Chile	2005	100000	2
CES	1.5m	TÜBITAK	Turkey	2007	55000	1
CHIRON	SMARTS	Cerro Tololo	Chile	2011	140000	12
CORALIE	Euler	Ginebra	Swizerland	1993	100000	117
Coudé	Alfred Jensch	Karl Schwarzschild	Germany	1997	67000	8
Coudé	CFHT	Mauna Kea	USA	1980	100000	1
Coudé	SONG	Teide	Spain	2014	100000	1
CSHELL	IRTF	Mauna Kea	USA	1997	30000	1
DS	1.5m	Fred Lawrence Whipple	France	1992	35000	2
ELODIE	1.93m	Haute-Provence	France	1993	42000	33
ESPaDOnS	CFHT	Mauna Kea	USA	2006	81000	2
ET	2.1m	Kitt Peak	USA	2006	10000	2
FEROS	2.2m	La Silla	Chile	2003	48000	22
FIES	NOT	Roque de los Muchachos	Spain	2006	67000	3
Hamilton	Donald Shane	Lick	USA	1992	40000	58
HARPS	3.6m	La Silla	Chile	2003	115000	262
HARPS-N	TNG	Roque de los Muchachos	Spain	2010	115000	37
HDS	Subaru	Mauna Kea	USA	2004	60000	12
HIDES	1.88m	Okayama	Japan	2001	70000	37
HiRES	Keck	Mauna Kea	USA	1996	85000	261
HRS	Hobby-Eberly	McDonald	USA	1998	60000	57
HRS	2.16m	Xinlong	China	2001	6000	16
IGRINS	Harlan J. Smith	McDonald	USA	2010	45000	1
IRD	Subaru	Mauna Kea	USA	2018	70000	1
KeckET	SDSS	Apache Point	USA	2006	51000	1
Levy	APF	Lick	USA	2013	110000	27
MARVELS	SDSS	Apache Point	USA	2008	11000	1
MIKE	Magellan II	Las Camapanas	Chile	2004	50000	22
NARVAL	Bernard Lyot	Pic du Midi	France	2007	74000	1
PFS	Magellan II	Las Campanas	Chile	2009	38000	42
Phoenix	Gemini South	Kitt Peak	USA	2001	70000	1
SARG	TNG	Roque de los Muchachos	Spain	2001	46000	2
SOPHIE	Euler	Ginebra	Switzerland	2006	75000	50
TOU	AST	Fairborn	USA	2013	100000	1
TRES	Tillinghast	Fred Lawrence Whipple	USA	2007	60000	9
TripleSpec	Hale	Palomar	USA	2004	2700	1
Tull	Harlan J. Smith	McDonald	USA	1994	60000	32
UCLES	AAT	Anglo-Australiano	Australia	1998	80000	54
UVES	VLT	Paranal	Chile	2000	47000	14

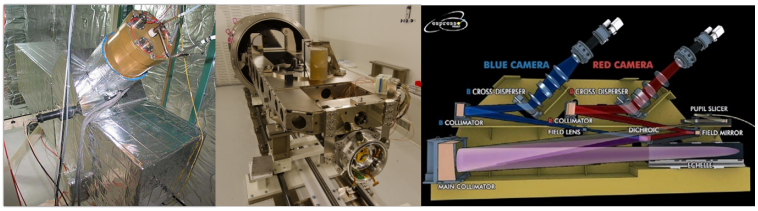

FIGURE 1.7— Evolution of the echelle spectrographs. **Left:** ELODIE spectrometer (first generation). **Center:** HARPS-N spectrograph (second generation). **Right:** Scheme of the ESPRESSO spectrograph (third generation). Credits: Sergio A. Ilovaisky (Haute-Provence Observatory), Istituto Nazionale di AstroFisica (INAF), and Denis Mégevand (University of Geneva).

From Table 1.2 it is important to note the role of CARMENES (Calar Alto high-Resolution search for M dwarfs with Exoearths with Near-infrared and optical Echelle Spectrographs) as a second-generation echelle spectrograph that allows simultaneous observations in the visible and near-infrared part of the spectra using two independent channels. Installed at the 3.5-meter telescope in the Calar Ato Observatory, CARMENES has become a key instrument for exoplanet discoveries around M-type stars due to the redder spectral distribution of these stars. Another remarkable example of an instrument that allows combined visible-infrared studies is GIANO (Oliva et al. 2004), a near-infrared high-resolution spectrograph installed in the TNG (Telescopio Nazionale Galileo) in 2012. This instrument can be used simultaneously with HARPS-N to have a wider wavelength coverage, although it provides a lower resolution than the one provided by CARMENES.

1.3.2 Future instrumentation

The large number of scientific results obtained by the current generation of astrophysical instrumentation dedicated to RV searches of exoplanets and its impact within the scientific community are paving the way for a new generation of instruments whose objective is to exploit the characteristics of the available ground-based telescopes and the future larger facilities to come. Within these future projects, it is important to highlight the HARPS3 spectrograph (Thompson et al. 2016), an upgraded version of HARPS and HARPS-N that is expected to be operating on the Isaac Newton Telescope (INT) in the Roque de los Muchachos Observatory in 2023. This instrument aims to improve the wavelength solution of its two predecessors thanks to modifications in the fibre

adapter, flow cryostat, and CCD. The robotization of the INT will allow performing extended automatic follow-up of the target stars, which will result in large RV time series ideal for the detection of the Earth-like planets. For the infrared planetary searches, the next great instrument to be developed is the Near-InfraRed Planet Searcher (NIRPS, Bouchy et al. 2017). Complementing HARPS in the 3.6-meter telescope of the La Silla Observatory, NIRPS will perform exoplanetary searches on M dwarfs with the goal of detecting rocky Earth-like planets. Simultaneous operations with HARPS are expected to be available in a similar way to how GIANO and HARPS-N currently perform in the TNG, which translates into better modeling of the stellar activity. Under current installation, is expected that NIRPS will see its first light during 2021.

Both HARPS3 and NIRPS are being developed for already existing telescope facilities. Currently, the European Southern Observatory (ESO) is carrying the construction of the largest visible/near-infrared ground-based telescope built to date: the European Extremely Large Telescope (ELT). With an expected first light in 2025, this reflecting telescope installed in the Atacama desert will include a 39.3-meter primary mirror that will operate using the newest adaptative optics techniques along with a laser guide system to obtain the best astronomical images to date. The amount of light collected by this telescope will be 13 times more than the one provided by the Gran Telescopio de Canarias (GTC), the current largest ground-based telescope. One of the instruments built for the ELT is the high-resolution spectrograph HIRES (HIgh-REsolution Spectrograph, Marconi et al. 2020. The ELT-HIRES allows simultaneous observations in the optical and near-infrared parts of the spectral with a resolution of $R = 100\,000$. One of its main science goals will be characterizing atmospheres of rocky-type planets in the habitable zone, but it will be also used for star formation, cosmological, and fundamental physics studies.

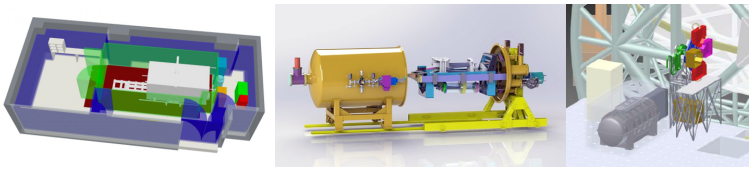

FIGURE 1.8— Conceptual design of the new generation echelle spectrographs. **Left:** HARPS3. **Center:** NIRPS. **Right:** HIRES. Credits: IAC, ESO/NIRPS, and ESO/HIRES.

1.4 Scope of the thesis

Considering the previously presented advantages that the RV method provides and the high number and quality of the current and future instrumentation dedicated to exploiting this technique, this thesis aims to seize these qualities to perform exoplanetary searches of super-Earth ($M_p \sim 2$–$10\ M_\oplus$) and Earth-like ($M_p \sim 1$–$2\ M_\oplus$) planets orbiting late-type stars (i.e., G, K, and M-type). To achieve this goal, we carried out two long-term RV surveys using HARPS-N at the TNG. The first one is the HADES (HArps-n red Dwarf Exoplanet Survey) program, a collaboration between the Instituto de Astrofísica de Canarias (IAC), the Institut de Ciències de l'Espai (IEEC-CSIC), and the Italian GAPS (Global Architecture of Planetary Systems) program (Covino et al. 2013), mainly focus on the detection and characterization of exoplanets orbiting M dwarfs. This program aims also to address statistically the properties of the planets around this type of star, which is poorly constrained. The second survey is the RoPES (Rocky Planets in Equatorial Stars) program, an effort led by the IAC that combines HARPS and HARPS-N observations to analyze a sample of nearby equatorial (i.e., observable from both hemispheres) G and K-type stars searching for planetary signals. The stars selected for this program present low magnetic activity and slow rotation. This feature and the use of the calibration instrument Laser Frequency Comb (LFC) in HARPS make it possible to detect small amplitude signals related to exoplanets.

In Chapter 2 we start by describing the calibration process performed with the LFC and other calibration instruments to achieve the best wavelength solution for the stellar spectra. Next, we show how this can be translated into more precise RV measurements and the scientific results that were drawn from this precision increase.

Chapter 3 contains a complete description of the stellar activity treatment necessary to unravel the planetary signals that lie below the Doppler shifts related to the star. The main case exposed in this Chapter is the multi-instrumental stellar activity analysis of Barnard's Star (Toledo-Padrón et al. 2019) that was key in the detection of the first candidate planet discovered around this star (Ribas et al. 2018).

Chapter 4 explains how to perform the planetary characterization once the stellar activity is removed, showing how to model this type of signals and how new generation instruments like ESPRESSO can improve significantly our results. The study of the star K2-38 and its two-planet system through the ESPRESSO spectrograph (Toledo-Padrón et al. 2020) is used as the main example for this methodology.

Chapter 5 focuses on blind RV searches of new exoplanets and the results obtained in the HADES and RoPES program. To illustrate this procedure the discovery of a super-Earth orbiting the M-type star GJ 740 is shown (Toledo-Padrón et al. 2021).

Finally, Chapter 6 serves to sum up all the results previously exposed and to establish future guidelines to continue with the work performed in the thesis.

2

Spectral calibration

I always try that my ships are equipped with the best saar invoice engines
Captain Mendosa of the Saar Fifth Fleet, Twilight Imperium

The desired goal of obtaining RV time series with the highest precision possible depends not only on the resolution provided by the spectrograph used but also on how this instrument is calibrated. Echelle spectrographs like HARPS operate using two identical fibers: the first one receives the light from the target star and the second one is usually used to conduct the light from the calibration instrument. Fig. 2.1 shows the usual display of this type of spectrographs.

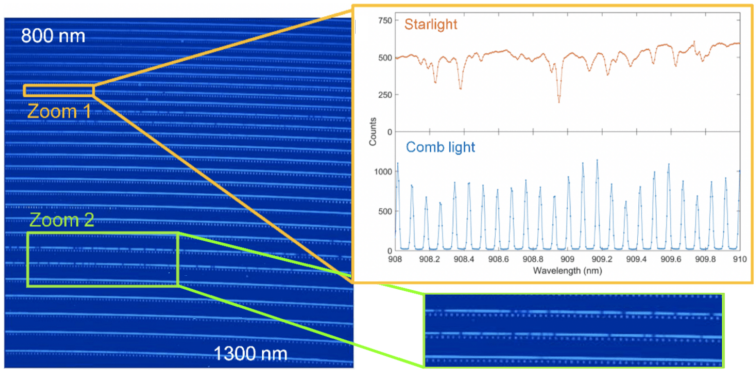

FIGURE 2.1— Typical layout of an echelle spectrograph.

In the left panel of Fig. 2.1 it can be seen how the two channels are distributed along the whole wavelength range provided by the spectrograph. The green lower panel shows a zoom of this distribution to distinguish the fiber corresponding to each channel. The orange upper panel illustrates how the spectrum located in each channel looks like. The spectrum of the star is contained in the fiber represented with a solid line in the green panel, while the calibration spectrum is contained in the fiber represented with a discontinuous line in the green panel. To ensure the best external conditions for the acquisition of the stellar spectra, the spectrographs are normally located inside a vacuum vessel surrounded by several isolation chambers, which protects them from temperature and pressure variations that can destabilize the RV measurements. In the case of the calibration instrument, it is normally located in a calibration unit separated from the vacuum tank that contains the spectrograph. Fig. 2.2 exhibits the overview of the HARPS system as an example of how these devices are distributed.

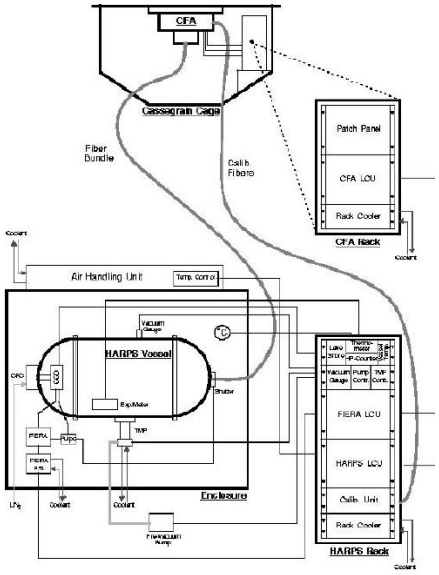

FIGURE 2.2— Schematic distribution of the HARPS spectrograph and its calibration system within the telescope facility. Credits: ESO.

Fig. 2.2 illustrates how the light from the calibration unit (located on the bottom right of Fig. 2.2) is conducted through a fiber to the Cassegrain focus of the telescope (located on the top of Fig. 2.2). Here, a small mirror guide this light into one of two fibers that leads to the vacuum vessel that contains the spectrograph (located on the bottom left of Fig. 2.2). One of the fibers contains the light from the star and the other the light from the calibration unit, and both of them are simultaneously recorded by the CCD detector in a single exposure. The calibration spectrum from the calibration unit can be generated with different sources.

2.1 Calibration sources

The first calibration source normally used for spectral calibration is the Thorium-Argon (ThAr) lamp (Baranne et al. 1996). This kind of lamp (along with others like Thorium-Neon lamps) has become one of the most used calibration instruments due to the large number of emission lines that it presents in the visible and near-infrared ranges (Lovis & Pepe 2007). However, it presents the counterparts of having spectral lines with different intensities and producing strongly saturated lines in the blue region of the spectra. This last problem can lead to contamination in the stellar spectrum for low S/N observations and exposure of late-type stars like M dwarfs which are characterized by faint blue regions. The stability of a second-generation echelle spectrograph like HARPS allows to have RV measurements with a nightly drift of about 1 $\mathrm{m\,s^{-1}}$ (Lovis et al. 2006). A ThAr lamp ensures this long-term precision and allows to characterize the short-term RV instrumental drifts experienced by the stellar spectra in a single night of observations with a precision of 20 $\mathrm{cm\,s^{-1}}$ (Lovis & Pepe 2007).

Another option for the wavelength calibration is the use of an Iodine (I_2) cell. First developed and tested in the Hamilton and HIRES spectrometers of the Lick observatory (Vogt 1987; Vogt et al. 1994; Cumming et al. 1999) and the HIDES spectrograph of the Okayama observatory (Takeda et al. 2002), the I_2 contained within an isolated cell produces absorption lines between 5 000 and 6 200 Å (Butler et al. 1996) that can be used to track the short-term RV drifts of the stellar spectra. In the case of HARPS, this cell is located in the Cassegrain focus of the telescope, instead of the calibration unit like the ThAr lamp. The accuracy in the RV determination with this method is similar to the one provided by the ThAr, but with much lower efficiency (Pepe et al. 2003).

One of the most widely used calibration instruments for RV planetary searches is the Fabry-Pérot (FP) interferometer. This type of interferometer provides a series of regularly spaced calibration lines that a high short-term

RV precision of 10 $\mathrm{cm\,s^{-1}}$ (Wildi et al. 2010). The FP interferometer has the advantage of avoiding possible contamination of the blue region of spectra which can be experienced with the use of a ThAr lamp but lacks the precise drift correction provided by this calibration instrument. In Fig. 2.3 a spectrum generated by an FP interferometer is shown along with spectra provided by the calibration instruments previously mentioned.

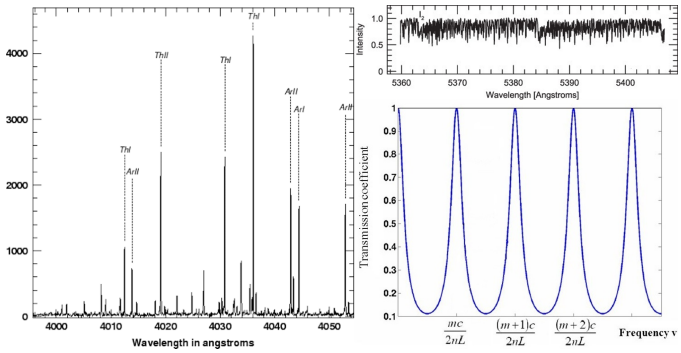

FIGURE 2.3— Examples of calibration spectra from different sources. **Left:** ThAr lamp. **Right Top:** I_2 cell. **Right Bottom:** Fabry-Pérot interferometer. Credits: Smithsonian Astrophysical Observatory/TRES, A. P. Hatzes (The Doppler Method for the Detection of Exoplanets), and Massachusetts Institute of Technology.

2.2 Laser frequency comb

The latest step in the instrumental development of calibration devices is the LFC (Laser Frequency Comb), a laser comb that generates thousands of spectral lines equally spaced in frequency and intensity with high precision (Murphy et al. 2007). This pioneering technology developed in the last 20 years was awarded with the 2005 Nobel Prize of physics (Hall et al. 2001; Udem et al. 2002) and has led to major discoveries such as the confirmation of the solar gravitational redshift (GRS) predicted by the general theory of relativity (González Hernández et al. 2020). The short-term RV stability achieved with the LFC is much higher than the one provided by the calibrations sources previously mentioned in this chapter, accomplishing results of 2.5 $\mathrm{cm\,s^{-1}}$ (Wilken et al. 2012). This calibration instrument is characterized by a lower photon noise than the ThAr lamp and presents a less complex spectral lines pattern that is easier to model. The inclusion of three FP cavities within the LFC setup

improves the RV precision in comparison with the one provided by a single FP interferometer.

The most noticeable example of an LFC currently operating is the one installed in the HARPS spectrograph, although new instruments like ESPRESSO are also incorporating this new technology. Several testing campaigns were carried out by the Max-Planck Institute for Quantum Optics and the Menlo Systems GmbH company, in collaboration with ESO, the IAC, and the Universidade Federal do Rio Grande do Norte in order to ensure the stable performance of this instrument. Considering that HARPS stores its spectra in different echelle orders (as it is expected from an echelle spectrograph), the first LFC testing phase accomplished between 2009 and 2010 was carried out operating with a single order (Wilken et al. 2010). The next campaign performed between 2010 and 2011 was used to implement and test a Photonic Crystal Fiber (PCF) whose role is to broaden the LFC spectra to 20 orders (Wilken et al. 2012). A third campaign was completed in 2012 (Probst et al. 2014) in which the LFC coverage was broadened to the majority of the HARPS spectral range (between 4500 and 6900 Å), although the short lifetime of the PCF in the blue part of the spectra produces alterations in this region. The HARPS-LFC was finally commissioned in 2015 [2]. One year later a study of the relative stability between two LFCs was performed (Probst et al. 2016), allowing the optimization of the HARPS-LFC fiber coupling. The LFC coupling to the HARPS setup is shown in Fig. 2.4 along with the LFC internal structure.

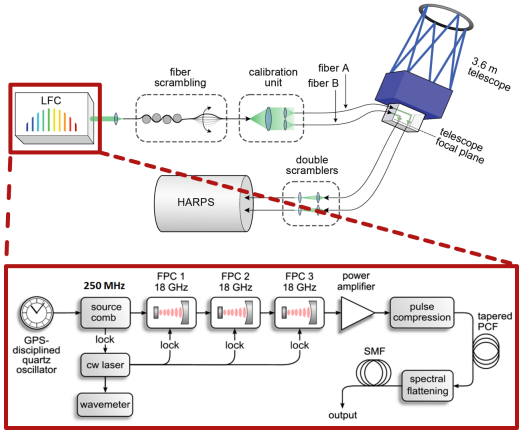

FIGURE 2.4— **Top:** Operational diagram of the 3.6m telescope with HARPS and the LFC. **Bottom:** Diagram of the LFC components.

[2] source: `https://www.eso.org/public/spain/announcements/ann15037/`

The bottom panel of Fig. 2.4 shows the different components of the LFC. The quartz oscillator controls the discrete emission of pulses coming from the laser. To stabilize the spectrum, a continuous emission is added to this spectrum. The signal is then filtered through three FP cavities which discard unwanted oscillation modes and later amplified by the power amplifier. The spectrum is finally broadened and flattened before going through the fiber scrambling. All the steps of this process are illustrated in Fig. 2.5.

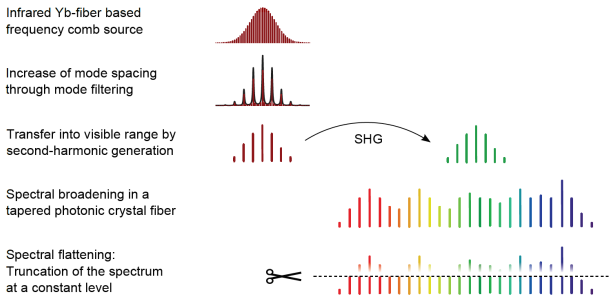

FIGURE 2.5— LFC spectra treatment. Since 2015 the Photonic Crystal Fiber (PCF) performs the wavelength shift shown in the third step which was previously carried out by a Second Harmonic Generator (SHG). Figure taken from Probst et al. (2014).

2.3 Calibration pipeline

The first main project carried out in the thesis was the creation of a calibration pipeline for the HARPS-LFC in order to be able to obtain customize wavelength calibrations that maximize the features of this instrument. To complete this task 6282 files from the 2015 LFC commissioning were used along with 2740 files from the previous testing campaigns.

2.3.1 Line modeling

The HARPS-LFC spectra present a structure of 72 orders with 4096 pixels each. Each order contains multiple laser emission lines whose theoretical frequency position is given by the following equation:

$$\nu_n = \nu_o + n\nu_r \tag{2.1}$$

where ν_o is the offset frequency and ν_r is the repetition frequency. The first step to determine the corresponding frequency ν_n to each line is to use the

ThAr wavelength contained in the header of each bi-dimensional spectrum. The header stores the coefficient of the calibration polynomial for each individual echelle order. Hence a wavelength matrix can be built with the same dimension as the flux matrix (72x4096). Then the following refractive index correction needs to be applied in order to put the wavelengths into the vacuum reference system in which the theoretical positions of the LFC lines are defined:

$$\lambda_v = \lambda \cdot n(P, T, \lambda) \tag{2.2}$$

where the refractive index n can be calculated taking into account the conditions of temperature T and pressure P to which the spectrograph is subjected:

$$n = 1 + \frac{P}{101325} \cdot \frac{10^{-6}}{1 + 3.4785 \cdot 10^{-3} \cdot (T - 15)} \cdot \left(64.328 + \frac{29498.1}{146 - \left(\frac{10^4}{\lambda}\right)^2} + \frac{255.4}{41 - \left(\frac{10^4}{\lambda}\right)^2} \right) \tag{2.3}$$

The next step after correcting the wavelength matrix is to detect the LFC lines in each order. Considering the levels of noise in the first echelle orders in HARPS, this detection is carried out in orders subsequent to the 31st. The detection is performed by searching for the peaks at relative maximum in the flux function of each order. To avoid false maxima, a minimum flux value is established based on the median per order to purge peaks below this level. Also, all the peak detections that exceed the number of theoretical lines that should be in the order considered are eliminated. The elimination criteria used is based on selecting the two lines with the smallest pixel separation and discarding the one with the lowest flux. An example of this detection is shown in Fig. 2.6 for the last HARPS order.

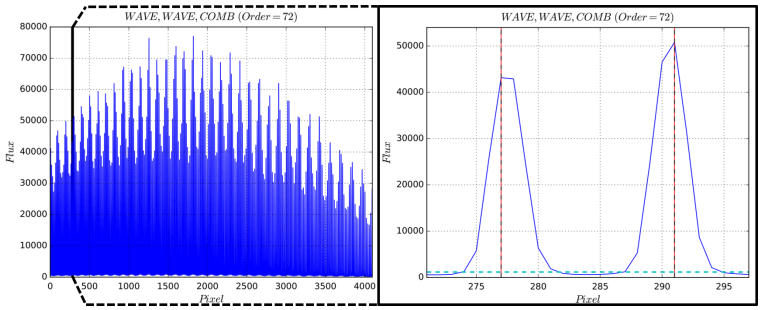

FIGURE 2.6— **Left:** Flux distribution in the 72nd order of an LFC spectrum. **Right:** Zoom over two LFC lines with their centroids marked with vertical lines and the flux threshold marked with a cyan horizontal line.

The right panel of Fig. 2.6 serves to exemplify how the line detection is performed. The cyan horizontal represents the minimum threshold to be overcome, the red vertical line represents the initial detection of the centroid of the line, and the black discontinuous line represents the verification of the two matching criteria (level of flux and number of lines). In the process, the first and last centroid of each order are removed to avoid edge effects. This provides a first approximation of the frequencies related to the centroid of each line according to the ThAr calibration.

The first approximation of the frequency of the centroids is not sufficiently precise, thus a second approximation is performed with the use of a fitting function. The pipeline allows the user to choose between four different models: Gaussian, Gaussian+constant, Gaussian+1st order polynomial, or Gaussian+2nd order polynomial. The selected model is then applied to all the LFC lines. The first approximation of the centroids frequencies previously obtained serves to establish the pixel fitting range for the selected model. The second approximation to the centroid calculation is illustrated in Fig. 2.7.

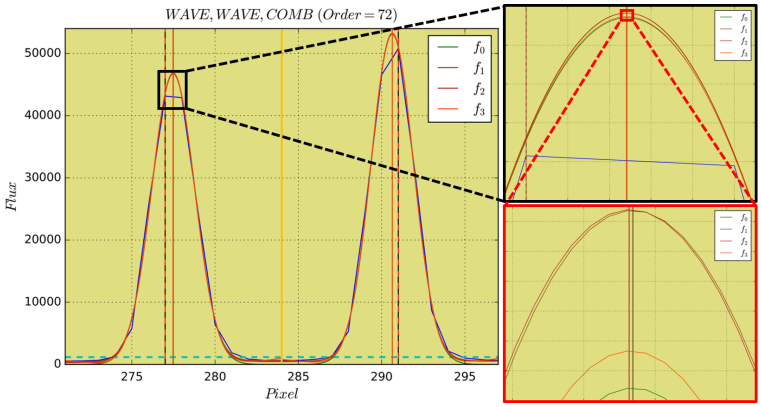

FIGURE 2.7— **Left:** Flux-pixel diagram of two LFC lines located in the last HARPS order. The four available fitting models are plotted with different colors. The yellow vertical line indicates the limits of the fitting regions. **Right:** Zoom panels over the top part of one of the LFC lines.

The right top panel of Fig. 2.7 shows how this second centroid approximation is more accurate than the first one. The right bottom panel allows us to distinguish the differences between the four available models, and how they

provide different positions of the centroid. The f_0 fit represents the Gaussian model, the f_1 the Gaussian+constant model, the f_2 the Gaussian+1st order polynomial model, and f_3 the Gaussian+2nd order polynomial model. The last three models include a measurement of the local background of the LFC line through the additional term to the Gaussian. The pipeline also allows us to perform a global background correction through an additional term in the model. This term includes a 2nd order polynomial that models all the flux values in the considered echelle order that are lower than the median threshold from the selection criteria. Then, an average sigma-clipping is applied to this term to obtain the final correction.

Therefore, the calibration pipeline offers eight models to the user (four with global background correction and four without). The χ^2 between each model (y_{model}) and the theoretical values ($y_{\mathrm{theoretical}}$) is defined as:

$$\chi^2 = \sum_i \frac{\left(y_{\mathrm{model,i}} - y_{\mathrm{theoretical,i}}\right)^2}{y_{\mathrm{theoretical,i}}} \tag{2.4}$$

The χ^2 values computed for the commissioning spectra reveal that the models with the global background correction applied provide better results. Between the four models that include this correction, the f_2 and f_3 lead to similar χ^2 values, with the Gaussian+1st order polynomial providing better modeling of the edges of the LFC lines. Nevertheless, the differences between all the options are small, both in amplitude and centroid pixel position, which makes it feasible to choose any of them to carry out the wavelength calibration.

2.3.2 Wavelength calibration

After selecting the model and obtaining the pixel position of the centroids, the pipeline assigns the theoretical LFC wavelengths from Eq. 2.1 to these pixel values. This provides a discrete pixel-wavelength relation. To extend this relation to the whole pixel range in all the echelle orders, the pipeline performs an interpolation, offering the user two different approaches. The first one uses a 3rd order polynomial to cover the complete pixel range of each order. The second one uses eight different 3rd order polynomials that cover a region of 512 pixels each. The reason for introducing this second option is the physical separation between the eight sub-chips that integrate the HARPS CCD detector. These sub-chips have a size of 512 pixels each, resulting in jumps in the wavelength calibration like the ones shown in Fig. 2.8 (Wilken et al. 2010).

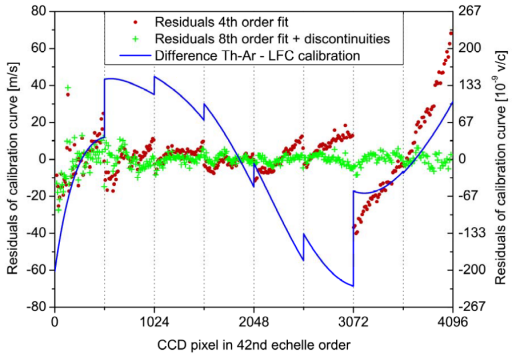

FIGURE 2.8— Residuals of the ThAr (red points) and LFC (green points) calibrations. Figure taken from Wilken et al. (2010).

In Fig. 2.8 it is clear how the LFC provides a wavelength solution with lower residuals in comparison with the ThAr calibration. The ThAr calibration provides higher residuals in comparison with the LFC sub-chip calibration due to the non-evenly spaced distribution of its emission lines. The ThAr lamp does not allow to perform a sub-chip calibration due to the insufficient number of ThAr lines within 512 pixels.

In this part of the process, the pipeline saves the coefficients of the selected calibration polynomial in the header of the target spectrum, allowing the user to retrieve the wavelength matrix later on in the same way as the ThAr matrix is built.

Due to the high computational time necessary to obtain the wavelength calibration of a single spectrum, the repetition of this process for all the spectra taken during one night of observations does not seem to be an optimal solution. To reduce this computational time and still be able to control the evolution of the instrument throughout the night, an RV drift calculation algorithm is included in the pipeline to obtain all the wavelength solutions referenced to one single spectrum. This drift is caused by small changes in the instrumental conditions, and it can be expressed as:

$$\frac{\delta V}{c} = \frac{V_1 - V_0}{c} = \frac{\delta\lambda}{\lambda_0} = \frac{\lambda_1 - \lambda_0}{\lambda_0} = \frac{\sum_i \frac{\delta V(i)}{c} W(i)}{\sum_i W(i)} \tag{2.5}$$

where λ_0 represents the wavelength of the reference spectrum from which the calibration was calculated, λ_1 represents the wavelength of the spectrum whose drift needs to be calculated, and c stands for the speed of light. The global wavelength shift $\delta\lambda$ between these two spectra can be expressed in terms of the RV drift experienced by each individual pixel $\delta V(i)$ and the weight associated with the considered pixel $W(i)$. The weight of a pixel i is related to the flux and wavelength that contains, and it can be calculated through the following equation (Bouchy et al. 2001):

$$W(i) = \frac{\lambda^2(i)\left[\frac{\partial A_o(i)}{\partial\lambda(i)}\right]}{A_o(i) + \sigma_D^2} \tag{2.6}$$

where A_o represents the flux of the reference spectrum and σ_D^2 the detector noise. Considering that the Doppler shift between two spectra taken in the same night is small compared to the width of the LFC lines, the intensity variation in the pixel i can be expressed as:

$$A_1(i) - A_0(i) = \frac{\partial A_0}{\partial\lambda}\delta\lambda(i) = \frac{\partial A_0}{\partial\lambda}\frac{\delta V(i)}{c}\lambda(i) \tag{2.7}$$

leaving the drift of an individual pixel as:

$$\frac{\delta V(i)}{c} = \frac{A_1(i) - A_0(i)}{\lambda(i)\frac{\partial A_0}{\partial\lambda}} \tag{2.8}$$

which allows writing Eq. 2.5 as:

$$\frac{\delta V}{c} = \frac{\sum\limits_i A_1(i) - A_0(i)\sqrt{\frac{W(i)}{A_0(i)+\sigma_D^2}}}{\sum\limits_i W(i)} \tag{2.9}$$

Through Eq. 2.9 is possible to calculate a drift value based on the flux variation in all the pixels of the spectrum. The results of this calculation for all the LFC spectra taken in the two HARPS fibers (A and B) during the 2015 commissioning are shown in Fig. 2.9:

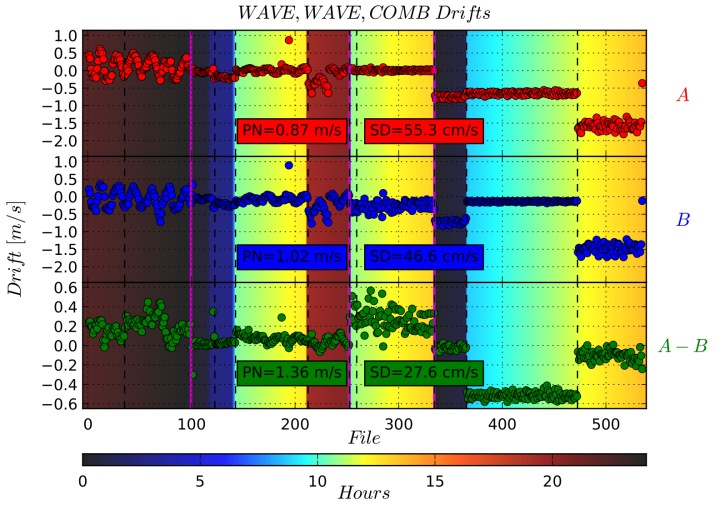

FIGURE 2.9— Evolution of the drift experienced by all the LFC spectra taken simultaneously in the two HARPS fibers (i.e., COMB-COMB) during the commissioning. The top panel represents the drift between spectra taken in the A fiber, the middle one shows the drift between spectra in the B fiber, and the bottom panel indicates the drift difference between these fibers. The photon noise and standard deviation of each series are also shown. The purple vertical lines divide the different nights of observation and the discontinuous black vertical lines indicate the different spectral series. The color map indicates the hour in which each spectrum was taken.

The photon noise shown in Fig. 2.9 is about 1 $\mathrm{m\,s^{-1}}$, which is the characteristic precision of the second-generation echelle spectrographs. The standard deviation of ~ 50 $\mathrm{cm\,s^{-1}}$ indicates the long-term stability of the spectrograph. The jumps between the different series of spectra shown in Fig. 2.9 are caused by the different configurations used during the commissioning (increase in the fiber length, flux optimization, temperature changes...). The short-term analysis of each individual night of observation shows how the LFC stability reaches the 1 $\mathrm{cm\,s^{-1}}$ level. This kind of analysis also serves to point out any instrumental problem that can affect the astrophysical data. The drift values are saved in the spectrum header along with the wavelength calibration.

The results of the analysis of all the spectra taken during the commissioning indicate a better performance of the LFC as a calibration source in comparison

with the ThAr lamp. To exemplify this, Fig. 2.10 exhibits the root-mean-square (RMS) of the residuals of three different calibrations (ThAr, LFC chip, and LFC sub-chip) with respect to the theoretical wavelength positions of the LFC lines.

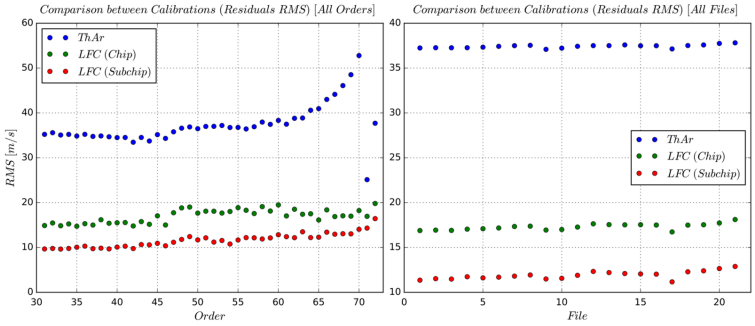

FIGURE 2.10— **Left:** RMS of the residuals of different calibrations for the echelle orders between 31 and 72 of a single LFC spectrum. The blue points represent the ThAr calibration, the green points show the LFC chip calibration, and the red points indicate the LFC sub-chip calibration. **Right:** RMS of the residuals of the same three calibrations for all the LFC files taken during one night of observation during the commissioning.

This methodology can be applied to a typical night of observation as follows: during the observing time, the astronomical spectra must be taken in the HARPS A fiber, while the LFC needs to be taken in the B fiber. Then, the wavelength calibration is performed using one of the LFC spectra (normally the first one taken). Then the drift of the rest of the LFC spectra is computed. The pipeline will provide the wavelength solution for the astronomical spectra according to these drift values. As an additional feature, the pipeline also includes an option to perform a second drift correction based on the mean A-B drift (i.e., drift between fibers) if there are COMB-COMB spectra available. Finally, the pipeline corrects from the barycentric velocity of the Earth (relative velocity of an observer located on the Earth with respect to the center of mass of the Solar system) and the radial velocity of the target star.

2.4 Radial velocity calculation

After obtaining the LFC wavelength calibration, the next natural step is to check how the wavelength precision of this calibration is translated into the

RV calculation for astronomical objects. For this analysis, we used the 171 stellar spectra+associated files taken during the commissioning along with 7 additional stellar spectra+associated files from previous HARPS observations.

2.4.1 CCF construction

The RV of a stellar spectrum can be calculated by measuring the Doppler shift in its spectral lines through the Cross-Correlation Function (CCF), defined as:

$$CCF(v) = \sum_i A(\lambda_i) \cdot M\left[\lambda_i \left(1 + \frac{v}{c}\right)\right] \tag{2.10}$$

with A being the intensity of the stellar spectrum at a wavelength λ_i and M being the mask template associated with the spectral type of the star. The v indicates the velocity used to shift the template. This provides one value of the CCF. Several shifts are needed in order to build the complete CCF, as shown in Fig. 2.11.

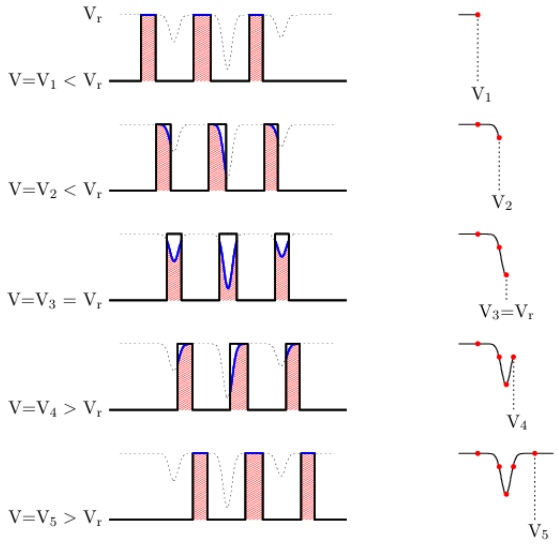

FIGURE 2.11— Example of the CCF calculation.

On the left part of Fig. 2.11 we show how the mask (represented by a solid line) matches the stellar spectrum (represented by a dashed line). Every row represents a shift of the template using a different velocity, which generates a point in the CCF as it appears on the right side of Fig. 2.11.

The HARPS-DRS (Data Reduction Software) pipeline (Lovis & Pepe 2007) provides six types of masks associated with six different sub-spectral types (G2, K0, K1, K5, M2, and M4). The three main ones are the G2, K5, and M2 masks, with a line coverage that varies between 4165 and 9196 wavelength positions. These masks contain wavelength intervals with different depths located at the positions of isolated stellar lines. The DRS also includes six files with the flux weights associated with each echelle order. The pipeline designed in this thesis includes a module to perform the RV calculation using these files.

This module allows the user to choose between any of the DRS masks and weight files along with a customized mask from Molaro et al. (2013). After selecting the RV sampling in which the selected mask is going to be shifted, the pipeline builds the CCF order by order, integrating the flux from the stellar spectrum and the lines of the selected mask whose wavelength falls within the range of the considered order. The wavelength of the stellar spectrum includes the drift and barycentric velocity corrections described in the previous sub-section. Then all the individual CCFs related to each order are added to obtain the final CCF. Once built, the complete CCF is fitted by a Gaussian function that can include a constant, a 1st order polynomial, or a 2nd order polynomial, as it was offered in the wavelength calibration process. The minimum of this function corresponds to the RV value that represents the Doppler shift experienced by the spectral lines of the studied spectrum A with respect to the model M. Finally, a correction for secular acceleration is implemented based on the distance and proper motion of the star (Stumpff 1985). An example of this calculation is shown in Fig. 2.12 for the stars HD 75289 (F9-type), HD 183658 (G3-type), HD 76700 (G6-type), and HD 123265 (K1-type), where a decrease in the width of the CCF towards late-type stars can be observed. This is caused by the lower projected speed rotation of stars with lower size. The CCF depth is connected with how well the mask fits the considered spectrum.

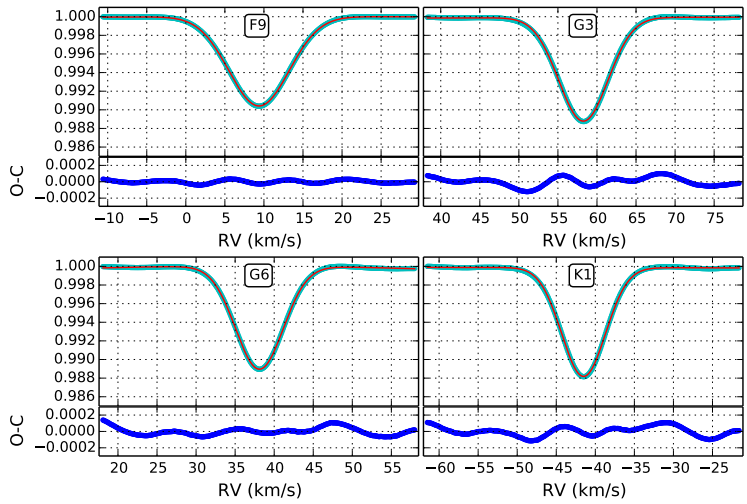

FIGURE 2.12— CCFs computed for four stars observed within the LFC commissioning along with their respective residuals O-C. **Top Left:** HD 75289. **Top Right:** HD 183658. **Bottom left:** HD 76700. **Bottom right:** HD 123265.

Following this methodology, the RV of the target stars observed during the commissioning were obtained and compared with the RV values included in the header of the files. As an additional comparison, the CCFs computed by the DRS were fitted with the same fitting function used in the self-constructed CCFs, and new RV values were computed weighting and adding the RVs of each individual order. Both the header and the DRS-CCFs values are related to the ThAr calibration. Nonetheless, the comparison between the values obtained with the ThAr and the LFC calibration only provides an RV difference in relative terms. To make an RV comparison in absolute terms, it is necessary to know with high accuracy the absolute RV of the astronomical objects we are studying.

2.4.2 JPL comparison

The ideal targets for RV accuracy studies (i.e., in terms of absolute RVs) are asteroids and planetoids in the Solar system due to their proximity to the Earth.

Between the 171 stellar spectra taken during the commissioning, there are 26 spectra of this type of objects. The objects observed were Ceres, Herculina, Massalia, and Parthenope. Herculina, Massalia, and Parthenope are three asteroids located in the asteroid belt between Mars and Jupiter. Ceres is a dwarf planet located in the same belt. Characterized by a diameter of 940 km, it is the largest object in this region. A spectrum of this planetoid is shown in Fig. 2.13.

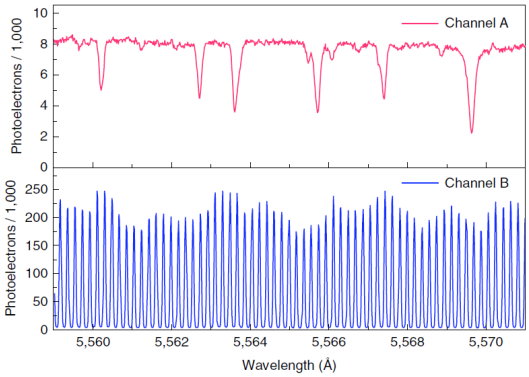

FIGURE 2.13— Zoom of a Ceres (channel A) and LFC (channel B) spectra taken with HARPS. The Ceres spectrum was obtained with a time exposure of 900 s and the LFC spectrum was generated with a frequency rate of 25 GHz. Figure taken from Probst et al. (2020).

The Jet Propulsion Laboratory (JPL) has designed a web interface named HORIZONS [3] which allows the users to compute precise absolute RV values of the Solar system objects based on dynamic models. The JPL data contains different dynamics parameters taken with a minute-precision. For the absolute RV calculation four of these parameters are necessary: the relative velocity between the Sun and the target object ($v_{\rm as}$) and its radial component ($v^r_{\rm as}$), and the relative velocity between the barycenter of the Earth and the target object ($v_{\rm oa}$) and its radial component ($v^r_{\rm oa}$). To obtain these parameters in the exact time when the HARPS spectra were taken, it is necessary to use the MJD+$t_{\rm exp}$/2 quantity as the mid-time of the observation. This quantity is calculated with the Modified Julian Date (MJD) and the exposure time ($t_{\rm exp}$) from the header.

[3] `https://ssd.jpl.nasa.gov/horizons.cgi`

The absolute RVs were calculated as $v^r_{\rm as}+v^r_{\rm oa}$, but an additional correction is still required.

Measurements of the Doppler shift with the precision considered in this case make it necessary to take into account relativistic effects. The relativistic Doppler shift $z_{\rm rel}=(\lambda_{obs}-\lambda_0)/\lambda_0$ can be expressed in terms of the following expression (Lanza et al. 2016):

$$\frac{\lambda_{obs}}{\lambda_0}=\frac{1+\frac{v_{\rm r}}{c}}{\sqrt{1-\frac{v^2}{c^2}}} \tag{2.11}$$

where λ_{obs} is the wavelength of the emitting source measured from the moving-frame system (in our case the Earth), λ_0 is the same wavelength in the rest-frame system (in our case the Sun), $v_{\rm r}$ the RV of the observed target with respect to the reference system and v the total velocity. Considering that the asteroids/planetoid we are studying are only reflecting the light from the Sun, our real emitting source is our parent star. This allows us to introduce an intermediate reference system located in the asteroid/planetoid to include the $v_{\rm as}$ and $v_{\rm oa}$ parameters provided by JPL in Eq. 2.11. From an observer located in this intermediate system, the measured wavelength will be λ_a, which means that:

$$\frac{\lambda_a}{\lambda_0}=\frac{1+\frac{v^r_{\rm as}}{c}}{\sqrt{1-\frac{v^2_{as}}{c^2}}} \tag{2.12}$$

while the wavelength change in the second part of the path traveled by the light (i.e., between the asteroid/planetoid and the Earth) is related to:

$$\frac{\lambda_{obs}}{\lambda_a}=\frac{1+\frac{v^r_{\rm oa}}{c}}{\sqrt{1-\frac{v^2_{oa}}{c^2}}} \tag{2.13}$$

which allows to express Eq. 2.11 as:

$$\frac{\lambda_{obs}}{\lambda_0}=\frac{1+\frac{v^r_{\rm oa}}{c}}{1+\frac{v^r_{\rm as}}{c}}\frac{\sqrt{1-\frac{v^2_{as}}{c^2}}}{\sqrt{1-\frac{v^2_{oa}}{c^2}}} \tag{2.14}$$

Using this expression it is possible to make the relativistic correction using the JPL parameters. Considering that the RV provided by the DRS is relative to the Solar system barycenter (RV_0), the RV relative to the Earth would be:

$$RV_{\rm obs}=RV_0-v_{\rm bary}-cz_{\rm rel} \tag{2.15}$$

where $v_{\rm bary}$ is the barycentric velocity of the Earth.

In this part of the process, we used the published Ceres RV values from Lanza et al. (2016) along with their respective spectra to ensure that the JPL computations were made correctly. We compared the individual JPL parameters ($v_{\rm as}$, $v^r_{\rm as}$, $v_{\rm oa}$, and $v^r_{\rm oa}$) along with the header values ($v_{\rm bary}$, $t_{\rm exp}$, and RV_0), and finally how this is translated into the relativistic correction and the final RV value. This comparison indicates a coincidence within the precision limits.

After checking that the JPL calculation was done correctly, we obtained the final results of this analysis, which were included as a part of a publication in the prestigious journal Nature Astronomy (Probst et al. 2020), where we proved the 1 cm s^{-1} stability provided by the LFC (see Fig. 2.14). The most relevant result was the one obtained for Ceres. The use of a G2 mask provided a difference of 3 m s^{-1} in the absolute RV with respect to the JPL value. This difference in accuracy is caused by the stellar activity of the Sun and the rotation of Ceres along with inhomogeneities in its albedo (Lanza et al. 2016). The design stellar activity models will be detailed in the next chapter, but before we describe the extension of the customize CCF-building and RV calculation procedure to other spectrographs.

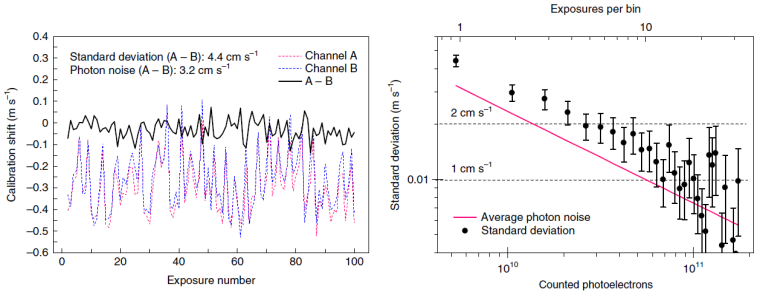

FIGURE 2.14— Relativity stability measurements between two LFCs with ν_r=18 GHz (channel A) and ν_r=25 GHz (channel B). **Left:** Relative shifts in channel A (red dashed line) and channel B (blue dashed line) with respect to a reference spectra of a series of 100 LFC calibration spectra taken every 61 s. The black solid line represents the differences between both channels. **Right:** Standard deviation and photon noise values computed for binned exposures of increasing size. Figure taken from Probst et al. (2020).

2.4.3 Extension to other instruments

As an additional stage regarding the RV computation based on self-constructed CCFs, the RV module of the pipeline developed in this thesis has been adapted to perform the complete process on different instruments. These instruments are the High Efficiency and Resolution Mercator Echelle Spectrograph (HERMES, Raskin et al. 2011 mounted on the 1.2-m semi-robotic Mercator telescope in the Roque los Muchachos Observatory, and the STELLA Echelle spectrograph (SES, Weber et al. 2012 located in the STELLA 1.2-m telescope at the Teide Observatory. The wavelength solution for the HERMES spectra was obtained using a simultaneous wavelength reference mode named HRF-WRF (that combines a High-Resolution Fiber with a Wavelength Reference Fiber) with a ThAr lamp, while the wavelength of the SES spectra was generated automatically by its pipeline using a Fabry-Pérot interferometer. The module was adapted to use the reducted spectra of both instruments, build the CCFs according to the selected mask, and perform RV measurements of the young K1-type star V 1298 Tau, which contains a planetary system of four transiting planets. An example of this calculation is shown in Fig. 2.15, where the CCF exhibits a large width due to the fast rotation of V 1298 Tau ($P_{\rm rot} = 2.91 \pm 0.05$ d).

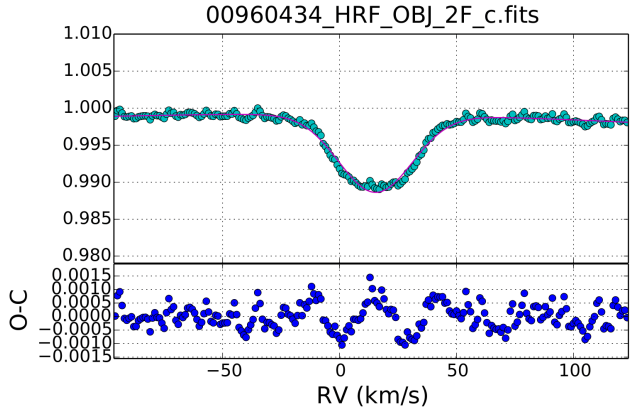

FIGURE 2.15— CCF built for one of the V 1298 Tau spectra taken with HERMES.

3

Stellar activity

Thank you, Mario! But our princess is in another castle!
Toad, Super Mario Bros.

Once the instrumental features have been exploited to obtain the most precise RV values, the next step is to study the periodic signals that are contained in these measurements.

3.1 Lomb-Scargle Periodograms

After performing an extensive observing campaign that provides an RV time series with enough datapoints, it is possible to visualize the periodicities present in the dataset through a Lomb-Scargle periodogram (Lomb 1976). This tool displays a power spectrum using the Fourier transform, where the statistical significance of a set of frequencies is represented. These significances are related to the χ^2 resulting from a least-square fitting of sinusoidal functions. In comparison with the Fast Fourier transform, the Lomb-Scargle periodogram presents the advantage of being able to deal with irregularly spaced datasets, which is the most usual case in RV samples. This least-squared spectrum represents the best measure of the contribution of the different frequencies considered to the total variation of the data but does not take into consideration the errors in the dataset.

The Generalized Lomb-Scargle (GLS) periodogram (Zechmeister & Kürster 2009) introduces an independent error for each of the values considered, allowing a more accurate frequency representation. Each frequency ω considered have

an associated significance computed as:

$$z(\omega) = \frac{N-3}{2} \cdot p(\omega) = \frac{N-3}{2} \cdot \frac{\chi_o^2 - \chi^2(\omega)}{\chi_o^2} \tag{3.1}$$

where N indicates the degrees of freedom. The χ^2 value depends on the time t_i, RV y_i, and error σ_i of each measurement. This value represents the squared difference between the data and the model selected (in the case of χ_o^2, the model is the weighted mean of all the measurements), and can be calculated as:

$$\chi^2 = \sum_{i=1}^{N} \frac{[y_i - y(t_i)]^2}{\sigma_i^2} \tag{3.2}$$

To establish the reference levels of statistical significance for the peaks in the periodogram we use the False Alarm Probability (FAP, Horne & Baliunas 1986). This threshold is an indicator of the probability for a certain frequency that its real significance being greater than the measured value. We calculated this value as (Cumming 2004):

$$FAP = 1 - [1 - P(z > z_o)]^M = 1 - [1 - e^{-z_o}]^M \tag{3.3}$$

where z and z_o are the target and measured power related to a certain frequency, respectively, $P(z > z_o)$ measures the probability of z being greater than z_o, and M is the number of independent frequencies used in the periodogram. This number is calculated as the total time coverage of the periodogram divided by the time-step used. Eq. 3.3 provides a first approximation of the usual 10 %, 1 %, and 0.1 % levels of FAP for the periodograms. For a more precise calculation of these levels, it is necessary to apply a bootstrapping method (Endl et al. 2001). This technique involves re-arranging the time order of the RVs analyzed 10 000 times, searching for the periodicity with the highest significance in every iteration to determine which values are obtained 10 %, 1 %, and 0.1 % of the times. An example of a GLS periodogram with the FAP levels is shown in Fig. 3.1 using an RV time series from the HARPS spectrograph.

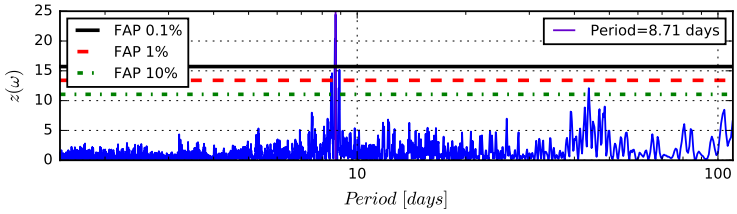

FIGURE 3.1— GLS periodogram of the HARPS RVs of the GJ 536 star showing a 8.7 d peak identified as a planetary signal of a super-Earth (Suárez Mascareño et al. 2017a).

3.2 Types of activity signals

The most prominent peaks in GLS periodograms like the one shown in Fig. 3.1 reveal the presence of signals whose origin needs to be studied. The final goal of this thesis is to detect and characterize RV signals caused by exoplanets. To do so, we first need to identify and model those signals originated by the activity of the star. There are four main sources that can be responsible for stellar activity signals.

The first possible source of activity are stellar oscillations (Leighton et al. 1962; Deubner 1975), which are characterized by a low amplitude. The research fields of helioseismology and astroseismology are focus on studying these oscillations in our Sun and other stars, respectively (Christensen-Dalsgaard 2002; García & Ballot 2019). To briefly summarize, the stellar oscillations can be described by three quantum numbers: the radial order n, the azimuthal order m, and the angular degree l. Depending on the n value, there are different oscillation modes depending on their origin: the g modes ($n < 0$) related to gravity waves, in which the restoring force is buoyancy, and the p modes related to acoustic waves ($n > 0$), in which the restoring force is pressure. These oscillations produce signals with a periodicity on the order of minutes in the case of the Sun and solar-type stars on the main sequence. This periodicity varies depending on the stellar mass, evolutionary stage, and spectral type of the star considered. A correct selection of the exposure time in the observations can allow minimizing this type of signals.

The second source is the stellar granulation (Herschel 1801; Dawes 1864; Carlsson et al. 2004), whose signals can range from the order of minutes (like in the case of the Sun, where granules have an expected lifetime between 10

and 20 minutes) to the order of days (for stars with greater radii or/and lower masses, Mathur et al. 2011). As in the case of stellar oscillations, this phenomenon changes with the stellar evolution and the spectral type. The granulation present in the stellar photosphere is related to the heat transport carried out through convections processes (Nordlund et al. 2009). It appears on the stellar surface as bright zones surrounded by dark areas, with a temperature gradient between them. It is possible to minimize the signals related to stellar granulation through the use of a wider time binning for the studied datasets (Meunier et al. 2015).

The next two sources cannot be minimized through observation techniques or changes in the sampling of the data, and need to be treated with specific models. The third type of stellar activity signals are those produced by the rotation of the star, associated with stellar spots and plages (Shajn & Struve 1929; Goldreich & Schubert 1967; Snodgrass & Ulrich 1990). The existence of stellar spots in the stellar photosphere and plages in the lower chromosphere is translated into changes in the chromospheric flux according to the rotational motion (Walter 1996). It is especially important to deal with the rotation signals in M dwarfs since their periodicity commensurate with the orbital periods of planets located in the habitable zone around these stars (Newton et al. 2016a; Vanderburg et al. 2016).

The last source of stellar activity are long-term magnetic cycles similar to the one experienced by the Sun, that can last for several years (Dravins 1985; Campbell et al. 1988). In the case of M dwarfs, several long-term magnetic cycles have been reported (Gomes da Silva et al. 2012; Savanov 2012; Robertson et al. 2013a; Suárez Mascareño et al. 2016), although the number of this type of detections is quite low in comparison with other spectral types.

To model the signals caused by these long-term cycles, single sinusoidals or second-order polynomials are normally used. In the case of signals caused by stellar rotation, a double sinusoidal function like the following one has been proven to be a good tool to model them (Boisse et al. 2011):

$$y(t) = A_1 \cdot sin(\omega_1 + \phi_1) + A_2 \cdot sin(\omega_2 + \phi_2) + A_3 \tag{3.4}$$

where $\omega_2 = 2\omega_1 = 2\pi t/P$. A more complex rotation characterization can be performed through a Gaussian Processes (GPs) regression (Haywood et al. 2014; Rajpaul et al. 2015; Ambikasaran et al. 2015). The GP sets a framework for Bayesian inference, where the set of variables considered obey a Gaussian distribution. These variables include the input observables (in our case, the acquisition time, RV, and RV error associated with each spectrum) along with the parameters of the model considered. The kernel used in a GP regression is a

covariance matrix with a dimension $n \times n$ (where n is the number of datapoints in our time series), where each element reflects the level of correlation of each pair of data. Between the available options, the following quasi-periodic kernel (Foreman-Mackey et al. 2017) has been proved to provide precise rotation characterization in both spectroscopic (Suárez Mascareño et al. 2020) and photometric (Wang et al. 2012) studies (this last one with a slightly different kernel):

$$\kappa(\tau) = \frac{K_{\rm rot}^2}{2+C} e^{-\tau/t_s} \left[\cos\left(\frac{2\pi\tau}{P_{\rm rot}}\right) + (1+C) \right] \tag{3.5}$$

where τ is the time interval between the two epochs considered. This kernel contains the squared amplitude of the rotation signal $K_{\rm rot}^2$, its periodicity $P_{\rm rot}$, and the timescale of the surface phenomena in the star t_s. The kernel also contains a term named C whose role is to measure the relative importance between the two components of the kernel: the periodic (i.e. the cosine) and non-periodic (i.e. the exponential).

The use of these fitting tools allows us to model the activity signals present in the GLS periodogram. The process followed to clean an RV time series from stellar activity consists of first selecting a signal from the periodogram (usually the most significant one) and model it with the desired fitting function. Then the model of this individual signal is subtracted from the time series, and a new GLS periodogram is computed from the RV residuals. Then we study the remaining peaks and repeat the process iteratively until there are no more significant signals in what is defined as a pre-whitening process. In every step of the process, all the model parameters are re-computed, and the fit is performed over the original RV time series (without any model subtraction).

The pre-whitening process arise the fundamental question of how to distinguish between RV signals related to stellar activity and those originated by exoplanets. To answer this question it is necessary to measure and study a different type of indicator from the RVs, which are not sensitive to the Doppler shifts caused by an exoplanet.

3.3 Activity indices

3.3.1 Chromospheric activity indicators

Through the study of the flux variations of certain spectral lines, it is possible to measure several chromospheric activity indicators, which help to model the stellar activity effects on the RV measurements. For the analysis performed during the course of this thesis, three indicators have been used.

The first indicator is the S-index related to the Ca II H& K lines (Noyes et al. 1984; Lovis et al. 2011), defined as:

$$S = \frac{H + K}{R + V} \tag{3.6}$$

where H and K are triangular passbands for the core of the lines (centered at 3968.470 and 3933.664 Å, respectively) with a full width at half maximum (FWHM) of 1.09 Å. R and V represent continuum filters that cover a wavelength range from 3981.070 to 4021.070 Å, and from 3881.070 to 3921.070 Å, respectively. Fig. 3.2 shows this spectral region in four different spectrographs.

The second indicator is the Hα index (Kürster et al. 2003; Gomes da Silva et al. 2011), which we calculate as:

$$H\alpha = \frac{A}{L + R} \tag{3.7}$$

where A is a rectangular passband centered at the core of the Hα line (6562.808 Å) with a width of 1.6 Å, and L and R are two continuum bands centered at 6550.870 and 6580.310 Å respectively, with a width of 10.75 and 8.75 Å, respectively. Fig. 3.3 shows the normalized Hα spectral region for an M-type star taken with seven different spectrographs.

The last activity indicator used is the Na I D index (Díaz et al. 2007; Houdebine et al. 2009), defined as:

$$N = \frac{D_1 + D_2}{L + R} \tag{3.8}$$

where D_1 and D_2 are rectangular passbands for the core of the sodium doublet lines (centered at 5895.92 and 5889.95 Å, respectively) with a width of 1 Å. L and R are continuum bands centered at 5805.0 and 6090.0 Å, with a width of 10 and 20 Å, respectively. Fig. 3.4 shows this spectral region in five different spectrographs.

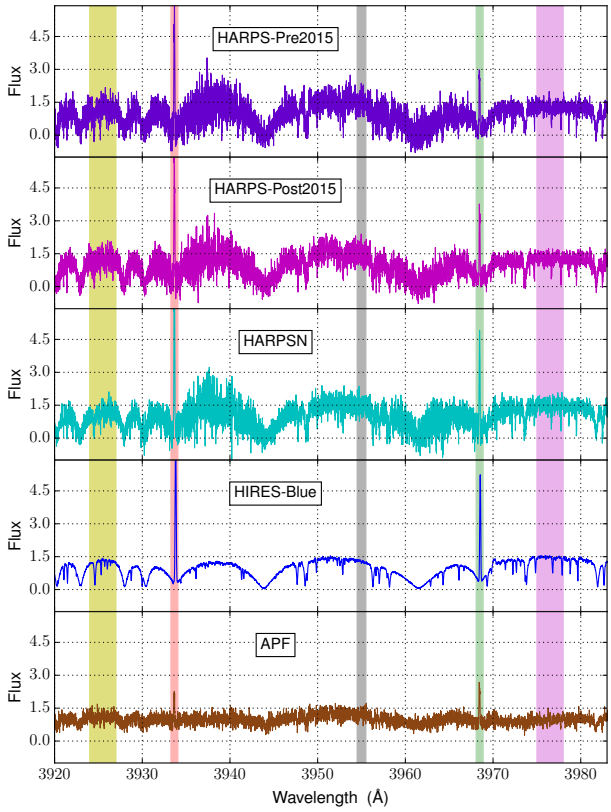

FIGURE 3.2— Normalized one-dimensional spectra of GJ 699 taken with four spectrographs. The Ca II H&K bands are marked in green and pink respectively, and the continuum passbands are marked in yellow and violet. The continuum region marked in grey indicates the spectral zone used to calculate the index error.

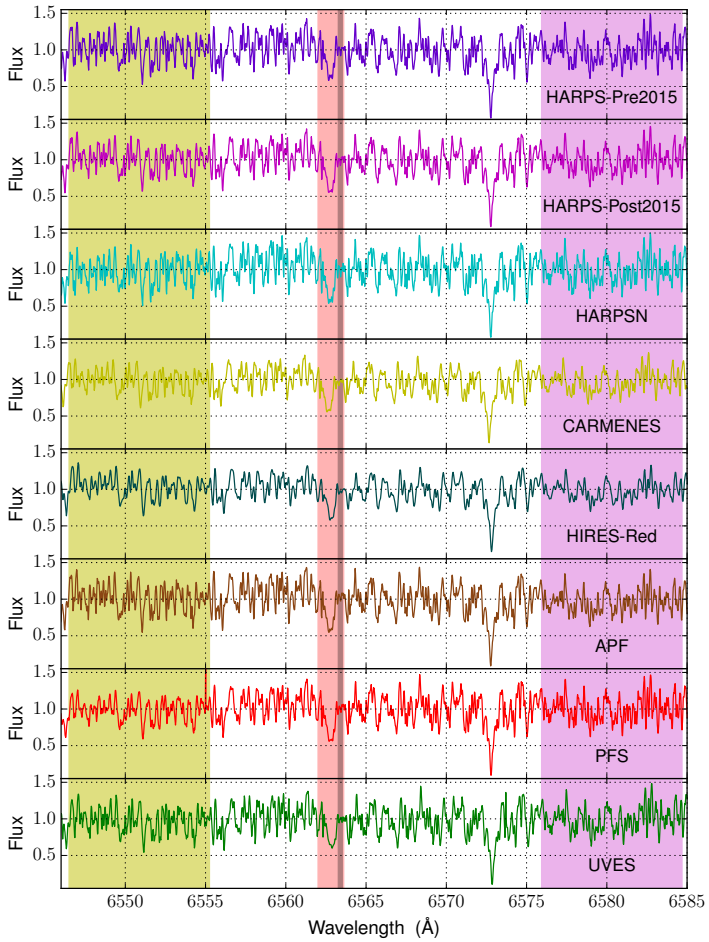

FIGURE 3.3— Normalized one-dimensional spectra of GJ 699 taken with seven spectrographs. The core band A is marked in pink. A0 modified version of the continuum passbands L and R are marked in yellow and violet, respectively. The continuum region marked in grey indicates the spectral zone used to calculate the index error.

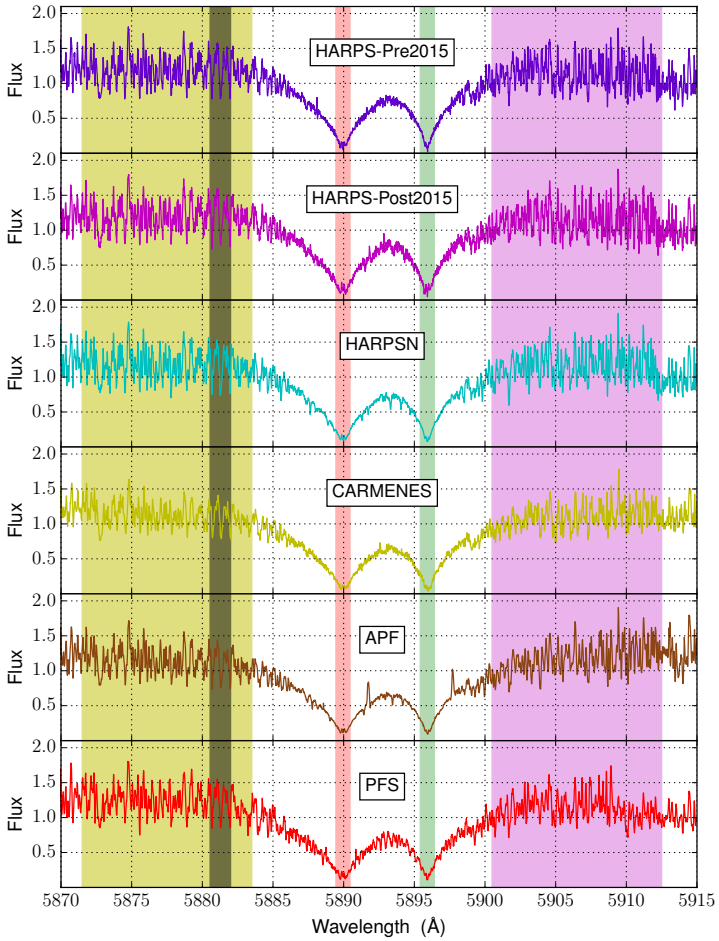

FIGURE 3.4— Normalized one-dimensional spectra of GJ 699 taken with five spectrographs. The Na I D_1 and D_2 bands are marked in pink and green respectively, and the continuum passbands are marked in yellow and violet. The continuum region marked in grey indicates the spectral zone used to calculate the index error.

In order to measure these activity indices, it is necessary to apply some corrections to the spectra used. The first one is the blaze correction, for which we used a blaze function that models the instrumental response independent from the astronomical object observed. Next, we correct for the pixel size variability in wavelength, which requires re-binning the spectra to obtain a constant step in wavelength between pixels and also to correct accordingly the flux evaluated in the selected wavelength step. Then, we performed a secular acceleration correction based on the proper motion of the observed star. Finally, the wavelengths are corrected for the barycentric velocity of the Earth and the radial velocity of the star.

After applying all of these corrections, we build an average spectrum (co-adding all the available spectra) and use the individual spectra to calculate the weights of each echelle order involved in the index considered. The weight of one order in a certain spectrum is calculated as the quotient between the normalized median of the flux of this order in the average spectrum and the selected spectrum. The result of applying these weights are the normalized spectra previously shown in Fig. 3.2, Fig. 3.3, and Fig. 3.4.

The uncertainties of the three indices can be determined through error propagation (Taylor 1982). For this calculation, we computed the individual error of each of the bands considered (A, L, R, H, K, V, D_1 and D_2) using the RMS of the region marked in grey in Fig. 3.2, Fig. 3.3, and Fig. 3.4.

3.3.2 CCF asymmetry indicators

Besides the chromospheric indices related to spectral lines, there are other indicators related to the CCF properties that can be used to track stellar activity.

The first of these indicators is the FWHM, which by definition can be calculated as $\mathrm{FWHM} = 2 \cdot \sqrt{2ln(2)} \cdot \sigma$, with σ being one of the parameters of the Gaussian fit of the CCF. For this calculation, the CCFs involved need to undergo a weighting process similar to the one applied to the spectra in the chromospheric indices calculation. For a single exposure, an average CCF is computed using individual weights for each echelle order as it was done with the spectra. In order to obtain a proper modeling, this CCF is cut to a certain width depending on the spectral type of the star (for G-type stars we used a width of 40 pixels, for K-type stars 35 pixels, and for M-type stars between 30 and 25 pixels) due to the variation in the projected speed rotation, and finally fitted by a Gaussian+second-order-polynomial model. Examples of this fit were previously displayed in Fig. 2.12 and Fig. 2.15.

The second of the CCF indicators is the Bisector Span (BIS), associated with the slope of the polynomial that fits the centroid of the CCF at different

heights (Queloz et al. 2001). This index measures directly the distortion of the CCF due to the presence of stellar spots and plages on the stellar surface. This distortion is greater in the case of fast rotators and active stars. In the case of M dwarfs, the BIS is not well defined due to the bumps present on the wings of the CCF (Rainer et al. 2020).

The third and last indicator is the chromatic index (CRX), introduced by Zechmeister et al. (2018). This index is related to the slope of the first-order polynomial that fits the RV-wavelength dependence across all the echelle orders. Due to its nature, this indicator works better in spectrographs with a wide wavelength coverage like CARMENES.

3.4 Rotation predictors

Once all the activity indicators are computed, we start to characterize the stellar rotation by computing the level of chromospheric activity $log_{10}(R^{'}_{\rm HK})$ (Noyes et al. 1984), defined as:

$$log_{10}(R'_{\rm HK}) = log_{10}\left((1.34 \cdot 10^{-4}) \cdot C_{\rm cf} \cdot < S_{\rm mw} > -R_{\rm phot}\right) \quad (3.9)$$

This quantity depends on three terms. The first one is the mean value of the S-index in the Mount Wilson calibration $< S_{\rm mw} >$ (Vaughan et al. 1981). To obtain this value, we apply the conversion described in Lovis et al. (2011):

$$S_{\rm mw} = \alpha \cdot S + \beta \quad (3.10)$$

where $\alpha = 1.111$ and $\beta = 0.0153$. Then we computed the conversion factor $C_{\rm cf}$ used to correct the flux variations in the S-index continuum passbands and to normalize to the bolometric luminosity (Middelkoop 1982), defined as:

$$C_{\rm cf} = (R + V) \cdot 10^{-4} \cdot 10^{0.4(m_{\rm v}+BC)} \quad (3.11)$$

where BC is the bolometric correction. For stars with $B - V > 0.4$ and $B - V < 1.95$, this expression can be expressed as (Suárez Mascareño et al. 2015):

$$log_{10}(C_{\rm cf}) = -0.443 - 0.645 \cdot (B-V) - 1.270 \cdot (B-V)^2 + 0.668 \cdot (B-V)^3 \quad (3.12)$$

Finally, we computed the $R_{\rm phot}$ which accounts for the photospheric contribution to the calcium core lines (Hartmann et al. 1984) that we need to get rid of in order to measure only the chromospheric contribution:

$$log_{10}(R_{\rm phot}) = (1.48 \cdot 10^{-4}) \cdot e^{-4.3658 \cdot (B-V)} \quad (3.13)$$

Several studies have been conducted to explore the relationship between the level of activity and the stellar rotation (see e.g. Walter & Bowyer 1981; Simon & Fekel 1987; Montes et al. 2004). Suárez Mascareño et al. (2015) quantified the following relation between the level of chromospheric emission and the rotation period using a sample of 48 late-type quiet stars (up to $log_{10}(R^{'}_{\rm HK}) = -4.5$) that was later expanded to 125 stars with spectral types between A and M characterized by a $log_{10}(R^{'}_{\rm HK})$ up to -4 in Suárez Mascareño et al. (2016).

$$log_{10}(P_{\rm rot}) = A + B \cdot log_{10}(R^{'}_{\rm HK}) \tag{3.14}$$

This relation can be used to obtain a first prediction of the rotation period of the studied star. Another useful relation from the literature is the connection between the chromospheric activity and the semi-amplitude K of the induced RV rotation signal (Suárez Mascareño et al. 2017b):

$$log_{10}(K) = A + B \cdot log_{10}(R^{'}_{HK}) \tag{3.15}$$

The rotation period is also connected with the level of X-ray emission (Pallavicini et al. 1981; Pizzolato et al. 2003; Wright & Drake 2016). This relation depends on whether the star is on the saturated or non-saturated regime, but can generally be expressed as (Reiners et al. 2014):

$$log_{10}(F_{\rm x}) = a_0 + a_1 \cdot log_{10}(P_{\rm rot}) \tag{3.16}$$

with $F_{\rm x}$ representing the $L_{\rm x}$ or $L_{\rm x}/L_{\rm bol}$ value. Within our HADES program, González-Álvarez et al. (2019) tested how this equation fits for M dwarfs using the complete sample of stars from the program. The X-ray emission measurements were carried out using ROSAT and XMM-Newton data, while the rotation periods came from earlier publications of the program. The study revealed the rotation period and age at which the saturation is reached with the best precision achieved to date. With our sample, we fill the slow rotation area, where the habitable zone of M-type stars is located, and therefore, habitable Earth-analogues could be found.

3.5 Barnard's Star activity analysis

With the activity models, the activity indicators time series, and the initial prediction of the stellar rotation, a complete stellar activity analysis can be carried out. From all the activity analysis performed during the course of this thesis, we highlight the one carried out on Barnard's Star (Toledo-Padrón et al. 2019).

3.5.1 Stellar properties

Barnard's Star (Gl 699) is the closest single star and second closest stellar system to the Solar system. Located at a distance of 1.8 parsecs (Gaia Collaboration et al. 2018), and with an age between 7 and 10 Gyr (Ribas et al. 2018), Gl 699 is the star with the highest proper motion known to date (Barnard 1916), which causes Doppler shifts due to secular acceleration (Kürster et al. 2003) that need to be taken into account. The most important properties of this star are shown in Table 3.1.

Table 3.1— Stellar properties of Barnard's Star.

Parameter	Gl 699	Reference
RA (J2000)	17:57:48.50	[1]
Dec (J2000)	+04:41:36.11	[1]
$\mu_\alpha \cos\delta$ [mas yr^{-1}]	-802.8 ± 0.6	[1]
μ_δ [mas yr^{-1}]	$+10362.5 \pm 0.4$	[1]
Distance [pc]	1.8266 ± 0.0001	[1]
$m_{\rm B}$	11.24	[2]
$m_{\rm V}$	9.51	[2]
Spectral type	M3.5V	[3]
$T_{\rm eff}$ [K]	3278 ± 51	[4]
[Fe/H] [dex]	-0.12 ± 0.16	[4]
$M_\star$ [M$_\odot$]	0.163 ± 0.022	[5]
$R_\star$ [R$_\odot$]	0.178 ± 0.011	[5]
$L_\star$ [L$_\odot$]	0.00329 ± 0.00019	[5]
log g (cgs)	5.10 ± 0.07	[4]
log ($L_{\rm x}/L_{\rm bol}$)	-5.4	[6]
$v \sin i$ [km s^{-1}]	<3	[4]
$a_{\rm sec}$ [m s^{-1} yr^{-1}]	5.15 ± 0.89	[7]
$\log_{10}(R^{'}_{\rm HK})$	-5.82 ± 0.08	[8]

References: [1] Gaia Collaboration et al. (2018); [2] Koen et al. (2010); [3] Alonso-Floriano et al. (2015); [4] Passegger et al. (2018); [5] Ribas et al. (2018); [6] Kiraga & Stepien (2007); [7] Kürster et al. (2003); [8] Toledo-Padrón et al. (2019)

As it is shown in Table 3.1, Barnard's Star presents a low X-ray luminosity and chromospheric emission, which indicates a low level of current magnetic activity. This reduces the effects of spots and plages in the spectral line profiles (Lovis et al. 2011). Using Eq. 3.14 and Eq. 3.16 with the coefficients provided by Suárez Mascareño et al. (2018a) and Wright et al. (2011), we estimated a rotation period of 142 and 132 days, respectively, which will be explored later.

3.5.2 Planetary companion

Ribas et al. (2018) reported the discovery of a candidate planetary companion orbiting Barnard's Star. This planet is characterized by an orbital period of $233\,^{+0.38}_{-0.41}$ d and a minimum mass of 3.23 ± 0.44 $M_\oplus$. Its semi-major axis positions Barnard b near the snow-line of the system (Kennedy & Kenyon 2008). The detection of this super-Earth was based on 771 RV epochs from seven different spectrographs. Fig. 3.5 shows the complete RV time series used along with the final planetary model.

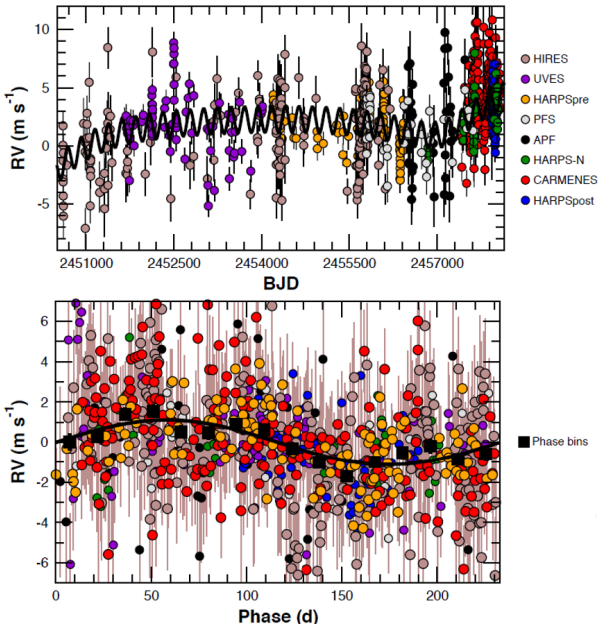

FIGURE 3.5— Original and phase-folded RV time series of Gl 699 with the best-fit to a 233-day circular orbit represented in black. Figure taken from Ribas et al. (2018).

This discovery produced a great impact on the scientific community due to the characteristics of the Barnard's Star and the planet itself. The work carried out in Toledo-Padrón et al. (2019) was motivated to confirm that this planetary signal could not arise from stellar activity.

3.5.3 Spectroscopic and photometric datasets

For the activity study, we used spectra from seven different spectrographs (the same ones that were used for the planetary detection). The main properties of each one of these datasets are shown in Table 3.2.

Table 3.2— Properties of all the spectrographs used for Barnard's Star activity analysis.

Spectrograph	$\Delta\lambda$ [Å]	N_{spec}	Time-span [yr]
HARPS	3780–6910	317	10.5
HARPS-N	3830–6930	74	3.3
CARMENES	5200–17100	192	1.7
HIRES	3700–10000	179	10.1
UVES	3000–11000	57	2.5
PFS	3880–6680	43	5.0
APF	3740–9700	95	2.7

Columns: Spectrograph name, spectral range, number of spectra, and time-span.

In the case of HARPS and HARPS-N, the calibration instrument used for the majority of the spectra was a ThAr lamp. For the most recent HARPS data, an ultra-stable Fabry-Pérot interferometer was used. The CARMENES calibration is similar, along with simultaneous Fabry-Pérot exposures and a daily calibration using ThNe, UAr and UNe lamps (Quirrenbach et al. 2018). The HIRES data were calibrated using a ThAr lamp. In this case, an additional calibration from an I_2 cell was used to extract accurate RVs, making some parts of the spectra unuseful to measure certain chromospheric indices like the Na I D.

UVES (Ultraviolet-Visual Echelle Spectrograph) is a high-resolution optical spectrograph installed in 2000 at the 8.2 m VLT in Paranal Observatory, Chile (Dekker et al. 2000). The UVES spectra were acquired using an image slicer, with an effective slit width of 0.3 arcsec that gives a resolution of $\sim 110\,000$ in the visible spectral range. The wavelength calibration of these spectra was obtained in a similar way as for the HIRES spectra.

PFS (Carnegie Planet Finder Spectrograph) is a high-resolution optical echelle spectrograph installed in 2009 at the 6.5 m Magellan II telescope in Las Campanas Observatory, Chile (Crane et al. 2010). The wavelength calibration method for the PFS spectra is similar to the one used in UVES.

The APF (Automated Planet Finder) consists of a 2.4 m telescope with the Levy Spectrometer commissioned in 2013 at the Lick Observatory, USA (Vogt et al. 2014). This instrument has a similar optical configuration to PFS, and also uses an I_2 cell to improve the derived RVs.

These spectroscopic datasets were complemented with photometric observations from four different sources. The main properties are shown in Table 3.3, including the mean error of the averaged nights, which indicates the scatter of the measurements within the night, giving an idea of the quality of the nights; and the RMS of the run, which gives a measure of the night-to-night stability.

TABLE 3.3— Properties of the photometric V-filter datasets.

Observatory Survey/ Telescope	Aperture [m]	Error [mmag]	RMS [mmag]	N_{epochs}	Time-span [yr]
Combined ASAS	0.07, 0.10, 0.14	10.4	16.8	836	15.1
FCAPT & RCT	0.80, 1.30	4.9	11.2	348	14.1
SNO	0.90	4.4	6.4	69	0.4
AAVSO	Range	15.1	8.9	148	0.3

Columns: Observatory, survey or telescope; telescope aperture; filters; mean error of the nights; RMS of the run; and number of epochs (measurements averaged to one per night).

The ASAS dataset combines data from ASAS-S, ASAS-N, and ASAS-SN. Data from the ASAS-S and ASAS-SN were retrieved from its public database[4], while data from ASAS-N were supplied by private communication.

The FCAPT (Four College Automated Photoelectric Telescope) is a 0.75 m automated telescope installed at the Fairborn Observatory (USA) that provides differential Strömgren uvby, Johnson BV, and Cousins RI photometry of a wide variety of stars (Adelman et al. 2001). The RCT (Robotically-Controlled Telescope) is a 1.3 m telescope installed at the Kitt Peak National Observatory (USA) that includes a $UBVRI$ broadband filter set and is focused on observing faint objects such as brown dwarfs (Gelderman 2001).

The Sierra Nevada Observatory (SNO, Spain), whose data come from the 0.9 m telescope (T90) that is equipped with a CCD camera VersArray 2Kx2K with a 13.2×13.2 arcmin^2 field of view. We collected about 30 measurements per night in each in B, V, and R Johnson filters, accounting for a total of about 2000 observations in each filter. These observations were acquired as a part of the Red Dots 2017 (RD2017) campaign[5], designed to search for planet signatures around our closest M-dwarf neighbors. As a part of this campaign, we also collected 72 epochs during 4 months with the Joan Oró robotic telescope (TJO)

[4] http://www.astrouw.edu.pl/asas/
[5] https://reddots.space/

located in the Montsec Astronomical Observatory (OAdM, Spain). The TJO is equipped with a CCD Andor DW936N-BV camera with a $12.3 \times 12.3\,\mathrm{arcmin}^2$ field of view. A minimum of 5 measurements was done per night, to finally obtain a total of about 700 images in two filters (R and I). As the previous photometric data from other instruments were acquired in the V filter, we do not include the OAdM dataset in the final analysis.

In addition to the RD2017 campaign, we requested support from the AAVSO (American Association of Variable Stars Observers) and issued an AAVSO alert with a call for photometric follow-up from observers. More than 8000 measurements in the $BVRI$ and Hα filters for Barnard's Star were uploaded to the AAVSO database. About 75 % of these observations/acquired exposures had great quality and could be included in the analysis. Measurements from different observers were not consolidated into nightly binned epochs.

We also analyzed data from the Las Cumbres Observatory network (LCO), the ASH2 0.40 m telescope at the SPACEOBS (San Pedro de Atacama Celestial Explorations Observatory) in Chile, and the MEarth survey.

In the case of LCO, data were obtained in the B and V Johnson and r' and i' Sloan filters. Unfortunately, data in the B, r', and i' filters could not be used due to instrumental issues. The data in the V filter were not included either in the final combined dataset due to their high dispersion both intra- and night-to-night, as reflected in the high mean error and root-mean-square (RMS), of 16.0 mmag and 30.5 mmag, respectively. The scattering was very high in comparison to the other observatories simultaneously acquiring data within the RD2017 campaign.

In the case of ASH2, observations were acquired in three narrow-band filters with an FWHM of 12 nm, centered on the OIII (501 nm), SII (672 nm) and Hα (656 nm) lines, with mean errors in the range of 14 to 24 mmag, larger than in most datasets. This is most likely attributed to the narrow filters and faint comparison stars. The night-to-night stability, shown by the RMS, is low, with values ranging from 7 to 13 mmag, depending on the filter. The narrow band lines were useful to monitor any possible activity bursts, such as flares, but were not included in the final combined dataset due to the short time base and larger scatter compared to the other RD2017 observatories.

Finally, we analyzed 161 epochs (across 6.7 yr) from the publicly available data of the MEarth survey. The large mean error in this dataset indicates that the measurements had a large intra-night scatter, but once consolidated into nightly averages, the scatter of the whole run decreased to 6.5 mmag, indicating that there were not large differences from night to night observations. We did not combine this dataset with the rest of the time series because it was taken with a filter that did not match the V Johnson filter used in the other datasets.

All photometric data (except for ASAS and MEarth) were reduced with standard procedures including bias and/or dark subtraction and flat-field correction. Several apertures were tried to extract the best aperture photometry that maximized the signal-to-noise ratio. Differential magnitudes were obtained with respect to nearby comparison stars that had previously been checked for stability and, in the case of observations taking place during the RD2017 campaign, agreed upon so that the different photometric datasets were as uniform and comparable as possible.

3.5.4 Time series computation and analysis

From all the available spectra, we computed the Hα, S-index, Na D, and FWHM time series. Several changes were introduced in the continuum bands of the chromospheric activity indices in order to avoid the wavelength overlap between consecutive echelle orders in all the spectrographs considered. We used narrower spectral regions near the core of the lines located in the same echelle orders as the spectra lines considered. In the case of the S-index measurements, we shifted the central wavelength of the continuum filters of R and V to 3976.5 and 3925.5 Å, modifying the width of both filters from 20 to 3 Å (we named this modified index CaHK). For the Hα measurements we used a width of 8.75 Å for the R passband. In the Na D index calculation we shifted the two continuum passbands L and R to 5881.5 and 5902.5 Å, and modified their widths to 12 Å.

We also used the BIS values from HARPS, HARPS-N, and CARMENES, although this time series did not provide any significant signal. Additionally, we analyzed the CARMENES CRX time series. We found a 10000 day-signal that disappears after a trend correction, which hints at the presence of a variability in the activity level on time scales much larger than the range of our observations.

We then computed the weighted average per night for both the spectroscopic and photometric measurements, discarding those values that are beyond 3σ from the median index in order to remove outliers. We also discarded values with errors beyond 3σ from the median error. The outliers may be associated in some cases with flares, a phenomenon already detected in Barnard's Star (Paulson et al. 2006), though occurring rarely due to its advanced age.

The relative offsets between instruments were calculated for each index separately. We divided the spectroscopic data into two separate blocks according to their time-span in order to have enough overlapping observations (the first one including HIRES, HARPS-Pre2015, PFS, APF, and UVES; and the second one including HARPS-Post2015, HARPS-N, and CARMENES). We split the HARPS dataset into two subsets due to the upgrade of the fibre link carried out in May 2015 (Lo Curto et al. 2015), which creates a discontinuity in the RV and

index values. To evaluate the offsets between instruments we used time windows of 10 days for spectrographs of the same block, and 30 days for spectrographs of different blocks. We determined the difference between the values contained in these windows and averaged all of them to obtain the offsets (within and between blocks). For the photometric data, we only used one block of instruments due to the long-time coverage of surveys like ASAS. After this process, an additional 3σ-clipping was applied to the complete dataset. The resulting time series and their corresponding periodograms are shown in Fig. 3.6 (in the case of the photometric time series, we did not use the FCAPT-RCT dataset for reasons discussed later).

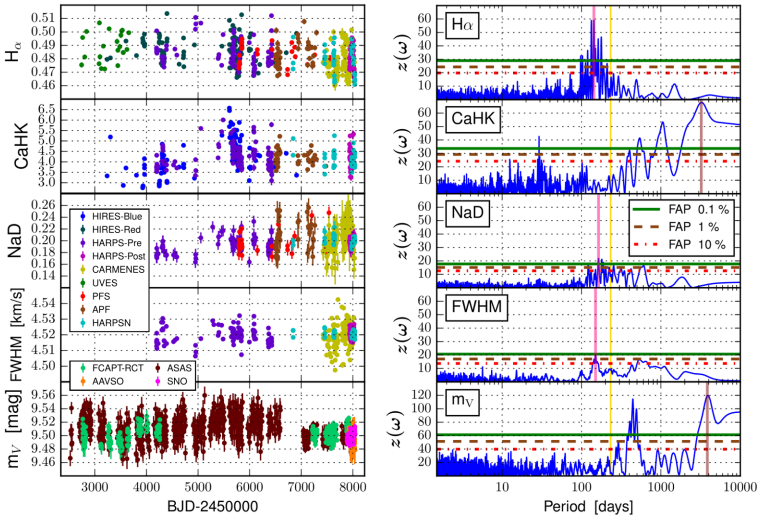

FIGURE 3.6— **Left:** Time series of the four spectroscopic indices and the V-band photometry of Gl 699 after the sigma-clipping and offset correction. **Right:** Periodograms of these time series. The most significant signals have been marked in different colors: pink for the ones associated with the rotation period and brown for the ones associated with the long-term activity cycle. The vertical yellow line shows the period of the super-Earth planet candidate Barnard b.

The FAP levels shown in Fig. 3.6 with horizontal lines are calculated with a bootstrapping technique. Signals with a FAP lower than 0.1 % (i.e. with a $z > z_{\mathrm{FAP}=0.1\%}$) are statistically significant, and those below the 10 % are non-

significant. For those with a FAP between 0.1 % and 10 % we cannot ensure that they are not false positives, and its nature can be open for discussion (especially for tentative signals below or close to a FAP of 1 %).

We first modeled the most significant peaks in the periodograms of Fig. 3.6 with a double sinusoidal (see Eq. 3.4) through the MPFIT routine (Markwardt 2009) in order to account for possible asymmetries (Berdyugina & Järvinen 2005). We left $A_1, A_2, A_3, \phi_1, \phi_2$ and P as free parameters, restricting the value of P in a 15 % from the original period in the periodogram. We add a jitter term associated with every single instrument considered in order to account for possible bad estimations in the index errors. We also included a trend correction in the cases where long-term variations were detected above our time coverage.

After subtracting the first signal, we repeated the process (maintaining the same FAP levels) until we had no more significant signals in the periodogram. After this pre-whitening process, we isolated each individual signal from the rest of the signals that we subtracted along this process. We selected one signal at a time and used the frequencies from the rest to make a model. The subtraction of this model gave us an isolated periodogram, where we can check that the original period was not caused by effects of the other signals. We obtained this isolated periodogram for every single signal that was detected along the pre-whitening process.

Before introducing the results for each time series using the complete dataset, we remark the fact that prior to this study, we previously began performing analyses on every single instrument individually. Considering that the information provided by a single instrument may not be enough in terms of timespan or sampling, we then added a second instrument with its respective offset and repeated the modeling-subtraction-isolation method. For the first block of spectrographs, we begin analyzing HIRES (the longest dataset), and then add HARPS-Pre, PFS, APF, and UVES in this particular order. For the second block, the initial spectrograph was CARMENES, and then HARPS-Post2015 and HARPS-N were added in that particular order. We analyzed each block of instruments separately and then joined them by applying their respective offsets. These preliminary analyses support the results that will be exposed below.

Hα index

For the Hα analysis, all the spectrographs were considered. The first periodogram of Fig. 3.6 was obtained after applying a trend correction. The non-corrected periodogram exhibits a 7692 days signal as the second most significant peak after the $\sim$140–150 days peak, which disappears after this correction. The

most significant peak in the first periodogram of Fig. 3.6 is located at 143 days, which is close to a previous determination of the rotation period from the literature (Suárez Mascareño et al. 2015). This signal is surrounded by multiple peaks between 130 and 177 days with low FAP. We fit this forest of peaks with a Gaussian model, whose FWHM gives us an error associated with the 143-day signal of 15 days. We note that the baseline of the observations is much longer than the expected lifetime of stellar spots and plages. These magnetic phenomena can occur at different stellar latitudes, favoring these multiple peaks around the rotation signal.

After the subtraction of the 143 days signal (modeled by a double sinusoidal), the remaining peak with the highest significance is a 149-day signal with a FAP close to the 1 % level (see the first periodogram of Fig. 3.13). When we isolate the 143 days signal from this new signal, the highest peak stays at 143 days with an amplitude of 0.00523 ± 0.00001 and a FAP above the 0.1 %, as shown in Fig. 3.7.

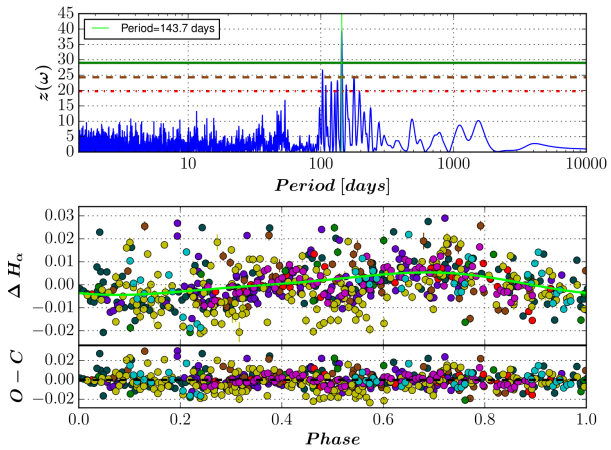

FIGURE 3.7— **Top:** Periodogram of the Hα time series after the subtraction of the 149 days period signal. **Bottom:** Phase-folded curve of the Hα time series using the 143 days period. Each spectrograph has been represented with a different color, following the legend in Fig. 3.6. The green line represents the best double-sinusoidal fit found by the MPFIT routine. Figure taken from Toledo-Padrón et al. (2019).

To complement this analysis, we introduced one jitter term per spectrograph in the double sinusoidal model and we changed the independent term (A_3) for

a linear trend term ($A_3 + A_4 \cdot t$). In this case, the error re-calculation associated with the jitter terms produces that the second signal to be detected shifts to 177 days with a FAP close to the 1 % level, and may also be related to differential rotation. The forest of peaks around the rotation period in the residuals is similar to the one shown in the first periodogram of Fig. 3.13, giving us a range of signals between 130 and 180 days.

Ca II HK index

In the time series of the CaHK index, the blue arm spectra of UVES, where the calcium lines are located, was not available. The CARMENES wavelength coverage did neither include the Ca II H&K spectral range and therefore it was not used. We also omitted PFS due to the high noise in that wavelength range. Therefore, we based this analysis on the HARPS, HARPS-N, HIRES, and APF measurements. Owing to the new continuum filters introduced in this work, we did not use the Mount Wilson calibration (Vaughan et al. 1978) for this index. In the complete dataset, we first detected a 3225.8-day signal that remains stable after the trend subtraction as shown in the second periodogram of the right panel of Fig. 3.6. This long-period signal may be related to a long-term activity cycle in the star. It has a FAP level above the 0.1 % and it is fitted by the double sinusoidal shown in Fig. 3.8 that includes jitter terms and has an amplitude of 0.5 ± 0.4.

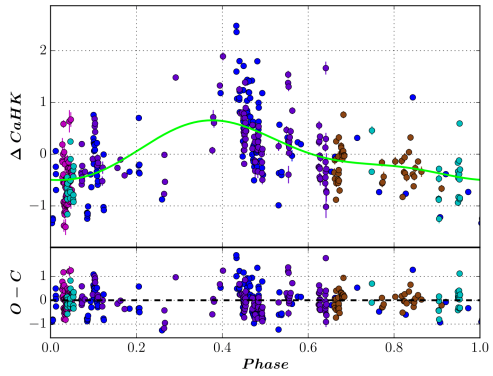

FIGURE 3.8— Phase-folded curve of the CaHK time series using the 3226 days period. Each spectrograph has been represented with a different color, following the legend in Fig. 3.6. The green line represents the best double-sinusoidal fit found by MPFIT. Figure taken from Toledo-Padrón et al. (2019).

When we subtract this model, we obtain a 120-day period signal with very low significance that seems to be dependent on the model used to subtract the long-term signal (see the second periodogram of Fig. 3.13). Depending on the use of jitter terms and trend correction, we obtain different peaks in the range of $\sim$80 to 200 days with a similar FAP, so we could not ensure that any of the signals are indeed stellar activity signals. We also could not find a clear signal associated with the expected rotation in the analysis of this index.

Na I D index

The time series of the NaD index does not include HIRES measurements because we could not get a reliable wavelength calibration for the echelle orders that contain the core lines and the continuum regions. We also avoid using UVES due to the lower signal-to-noise ratio (S/N) in those orders. The set of remaining spectrographs (HARPS, HARPS-N, CARMENES, PFS, and APF) produces the third periodogram shown in the right panel of Fig. 3.6, which reveals a 164-day signal surrounded by a forest of peaks similar to the one found in Hα that could be associated with the rotation of the star. The difference in period with respect to the signal detected in the Hα index suggests that this signal could be caused by differential rotation. In the Sun, for instance, the rotation period can vary from the equator (25 days) to the pole (35 days) in 40 %. From a sample of more than 24 000 active *Kepler* stars, Reinhold et al. (2013) found evidence of differential rotation within the 30 % of the equatorial rotation period in 77 % of the sample. In a more recent study, Aigrain et al. (2015) tested a blind hare-and-hounds exercise using 1 000 simulated photometric light curves, and found little correlation between the reported and simulated values of the differential rotation, indicating that this detection in single light curves must be treated with caution. With a spectroscopic study like ours, using time series from different activity indicators, we gain reliability with the detection of the same structure around the rotation period in two of the time series. In this case, the variation from the original period measured in Hα to the one measured in Na I D is only 15 %. This signal has an amplitude of 0.0070 ± 0.0008 and its FAP grows near the 0.1 %.

When we subtract this signal with the double sinusoidal model shown in Fig. 3.9 that includes jitter terms, the rest of the peaks remain with FAP values higher than 1 % (see the third periodogram of Fig. 3.13), and they may be caused by the offsets between spectrographs, so no more clear information was extracted from this index.

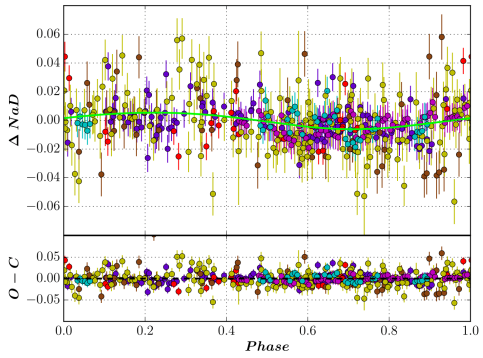

FIGURE 3.9— Phase-folded curve of the NaD time series using the 164 days period. Each spectrograph has been represented with a different color, following the legend in Fig. 3.6. The green line represents the best double-sinusoidal fit found by MPFIT. Figure taken from Toledo-Padrón et al. (2019).

FWHM

The FWHM time series was computed from the CCFs provided by the HARPS, HARPS-N, and CARMENES pipelines are shown in Fig. 3.10.

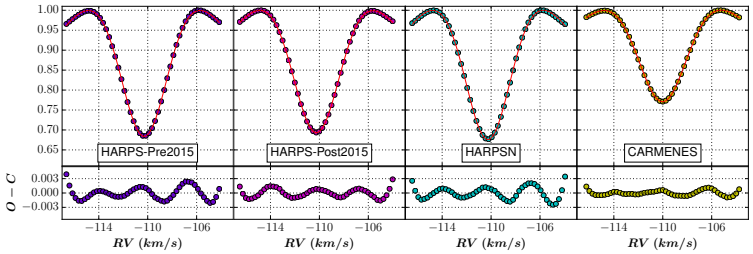

FIGURE 3.10— Individual CCFs of the spectrographs used for Barnard's Star analysis.

In the analysis of these measurements, we first apply a trend correction to the HARPS-Pre2015 values due to a focus drift problem. We also noticed a higher dispersion in the CARMENES values that may be related to the lack of weights per order in this spectrograph (the CCFs that we have used were already built as a one average function). The combination of the measurements

from the three available spectrographs leads to a tentative detection of the rotation period at 150 days with a FAP level close to 0.1 %, as it is shown in the fourth periodogram of Fig. 3.6. In this case, the signal is fitted by the double sinusoidal shown in Fig. 3.11 with an amplitude of 0.00343 ± 0.00006 km s^{-1}. After subtracting this first peak with a double sinusoid function including jitter terms and a global trend, the remaining peaks do not exceed the 10 % level of FAP (see the fourth periodogram of Fig. 3.13), making it difficult to establish a clear origin for them.

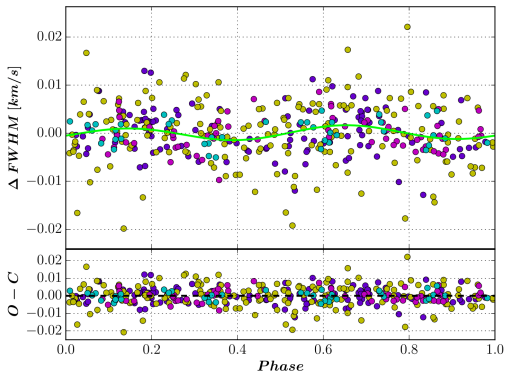

FIGURE 3.11— Phase-folded curve of the FWHM time series using the 150 days period. Each spectrograph has been represented with a different color, following the legend in Fig. 3.6. The green line represents the best double-sinusoidal fit found by MPFIT. Figure taken from Toledo-Padrón et al. (2019).

Photometry

We complement our spectroscopic analysis using the time series of V-band photometric measurements. We begin by analyzing the largest dataset (ASAS), combining the ASAS-S and ASAS-N time series. In this dataset, the most significant signal is located at 3703.7 days, which may be related to a long-term activity cycle in the star. After the subtraction of this signal with a very high amplitude (0.012 ± 0.004 mag), the rest of the peaks in the periodogram remain under the 10 % level of FAP, with the rotation period at 141 days being the second signal in amplitude. The addition of the ASAS-SN dataset produces a shift in the peak of the long-period signal to 3846 days.

When we add the AAVSO and SNO datasets and determine the offsets using ASAS as a reference, we recover the long-term activity cycle signal at 3846 days

signal present in the complete ASAS dataset (see the fifth periodogram in the right panel of Fig. 3.6).

The addition of the FCAPT-RCT dataset creates a broad signal at 204.5 days as the most significant one. After the subtraction of this first signal, we recover the long-term activity cycle signal at 3846.2 days obtained in the previous time series with an amplitude of 0.009 ± 0.008 mag. The isolated periodogram of this signal and its model are shown in Fig. 3.12, where the periodicity of the cycle is even clearer than in the time series of the CaHK index due to the higher number of points.

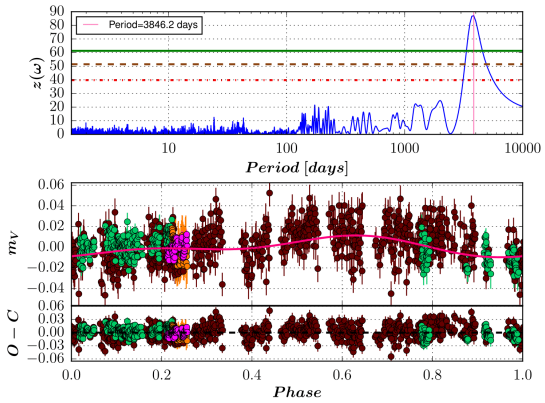

FIGURE 3.12— **Top:** Periodogram of the ASAS+AAVSO+SNO+FCAPT-RCT m_V time series after the subtraction of the 204.5 days period signal. **Bottom:** Phase-folded curve of the m_V time series using the 3846.2 days period. Each instrument has been represented with a different color, following the legend in Fig. 3.6. The pink line represents the best double-sinusoidal fit found by MPFIT. Figure taken from Toledo-Padrón et al. (2019).

The problem with the FCAPT-RCT dataset is the underestimation in the m_V errors, which produces the high amplitude signal at 204.5 days in the periodogram. When we apply a jitter term to this dataset and recompute the errors, we recover the long-term signal with its expected amplitude. It is also important to take into account the time gap of ~ 8 years between the FCAPT and RCT datasets, which can affect the results due to a bigger uncertainty in the offset between those two datasets. The same happens between the datasets of ASAS-S+ASAS-N and ASAS-SN, with a gap of more than 1 year between them, but in this case, the difference is not so remarkable. We maintain the

ASAS-SN time series in the analysis because it is needed to obtain the offset values using the time windows methodology and the FCAPT-RCT time series because it increases the m_V amplitude of the long-term activity cycle signal. The residuals of these time series after subtracting the model shown in Fig. 3.12 are displayed on the fifth periodogram of Fig. 3.13.

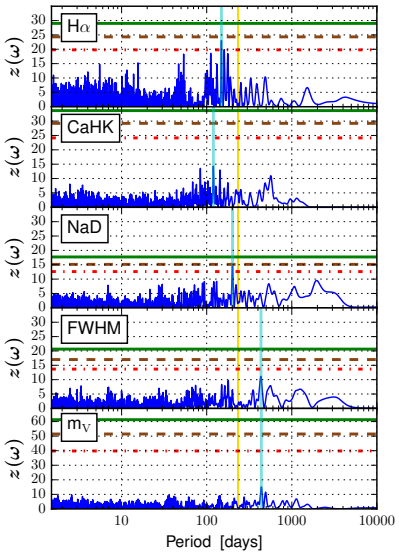

FIGURE 3.13— Periodograms of the residuals of the four spectroscopic indices and the V-band photometry of Gl699. The most significant signal in each periodogram has been marked in cyan, while the orbital period of Barnard b is marked in yellow.

In the separate analysis of Montsec and MEarth time series from different photometric filters, we do not detect any significant signal that could be attributed to rotation or a long-term activity cycle, although MEarth has proven to be capable of detecting rotation periods (Feng et al. 2019).

Finally, we computed the window function for each time series of each activity indicator including the photometric and RV data using the Systemic console (Meschiari et al. 2009). We find only a few signals related to the daily sampling and the yearly periodicity of the observations (the most significant at 365 and 1850 days).

3.5.5 Results

Activity cycle

In the CaHK and m_V time series, we detected two long-period signals with similar periodicities, both compatible with the length of a solar-like cycle. The comparison of the two series side by side shows that, not only their periods are compatible, but the dates of their maxima and minima are virtually the same, hinting at a common underlying phenomenon (see Fig. 3.14). The combination of the two series gives us coverage across two full phases of the signal, pointing at a cyclic nature. We can interpret this variability as the footprint of a magnetic cycle of 10 ± 2 yr, which is not expected for a completely convective star like Barnard's Star (Chabrier & Küker 2006). Given our short baseline, the exact period and long-term behavior are still complicated to assess. Further monitoring spectroscopic and photometric would be needed to better characterize it.

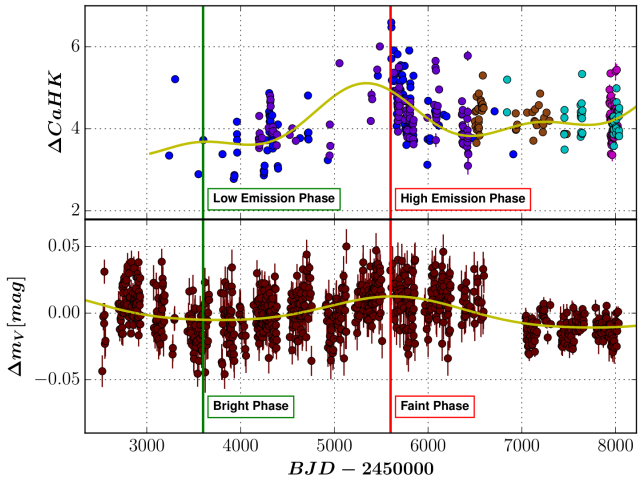

FIGURE 3.14— **Top:** Time series of CaHK for HIRES-Blue+HARPS-Pre2015+APF+HARPS-Post2015+HARPS-N spectra. The beginning of the low emission phase is marked in green and the beginning of the high emission is marked in red. **Bottom:** Time series of ASAS-S+ASAS-N m_V. The beginning of the bright phase is marked in green and the beginning of the faint is marked in red. In both panels, the yellow line represents the best double-sinusoidal fit found by MPFIT. Figure taken from Toledo-Padrón et al. (2019).

Fig. 3.14 shows how the position of the maximum emission phase coincides with the position of the faintest phase of the star, while the minimum emission phase coincides with the brightest phase of the light curve. Given the low level of chromospheric and X-ray emission of Barnard's Star (Passegger et al. 2018), this behavior is opposite to the solar case, and to most old FGK stars (Radick et al. 1998). It would be compatible with a spot-dominated stellar surface, typical of active FGK stars (in the case of the Sun and low-activity stars, the stellar surface is faculae-dominated, Lockwood et al. 2007). In active stars, spots dominate the brightness changes, while plages would dominate chromospheric and X-ray emission. The situation is similar to what Wargelin et al. (2017) found for the case of Proxima, when comparing V-band photometry to X-ray and UV emission, as well as the anti-correlation between the FWHM of the CCF and the brightness changes found by Suárez Mascareño et al. (2020) in the same star. Despite being old, Proxima remains quite active (Pavlenko et al. 2017), which made it natural to put in on the "active stars" category. The case of Barnard is quite different, as the star shows very low levels of chromospheric and X-ray emission. This could hint at late-M dwarfs keeping their "active star" behavior, and remaining spot dominated, even after their chromospheric and X-ray emission reach extremely low levels.

Rotation pattern

Combining the rotation period from Hα and FWHM time series with weights according to their FAP level we obtain a final average value of 145 ± 15 d. The 10 % error comes from the FWHM of a Gaussian model that fits the forest of peaks around the 145-day signal and takes into account the uncertainty in the latitude of the active regions that are producing this signal. We discard the photometric detection due to its low statistical significance. This insufficient significance is related to the typically low photometric amplitude of the rotation signal in slow-rotating M dwarfs (see e.g. Suárez Mascareño et al. (2016), Díez Alonso et al. (2019)), which is below the RMS of most of our photometric datasets, including ASAS. The spectroscopic rotation value matches the predictions from the X-ray luminosity (132 d) and the $log_{10}(R'_{\rm HK})$ (142 d). This means that Barnard's Star is among the main sequence stars with the slowest rotation known to date, above the M-stars typical rotation periods (Newton et al. 2016b). This also suggests that Barnard's age matches the age of the local thick disk, which is around 9 Gyr (Newton et al. 2018). Our results regarding Barnard's Star rotation have subsequently been supported by the analysis performed by Bortle et al. (2021) using HARPS and HIRES data.

Differential rotation may be responsible for the different signals found between 130 to 180 days, as a consequence of the presence of active regions at different latitudes of the stellar surface. This phenomenon has not been fully understood for stars from all spectral types, but especially for M dwarfs. In the case of fast-rotating M-type stars, it is expected that their strong magnetic field minimizes differential rotation (Browning 2008), while in the case of slow-rotating M dwarfs such as Barnard's Star, the effects of differential rotation are expected to be more significant (Brown et al. 2020). Reinhold & Gizon (2015) confirmed a relation between rotation period and differential rotation predicted by Reiners & Schmitt (2003) including M-type stars in their sample. Although this relation has only been proven for stars with $P_{\rm min} < 50$ days, we obtain a value for Barnard's Star of $\alpha = (P_{\rm max} - P_{\rm min})/P_{\rm max} = 0.278$ that matches the M-stars values present in this study. Taking into account that differential rotation is more evident in slow rotators, we conclude that our estimation is consistent with the theoretical prediction for differential rotation.

Impact on the planetary detection

The year-alias of a rotation period of 145 d happens at a period of about 240 d (Dawson & Fabrycky 2010) that is close to the planetary signal of 233 d of Barnard b. We computed the periodogram of the RV data published by Ribas et al. (2018) using the Systemic console, including a linear trend term along with offset and jitter terms for each instrument as free parameters, which removes any possible long-term signal (of several years) that could be associated with either long-term activity or long-period planetary signals. The first periodogram after minimizing the linear term, offset and jitter values provides the strongest signal at 233 d and secondary much less significant signals at 1 d and 77 d, but no significant signal around 145 d. A real signal should appear at its original frequency and also at its two alias frequencies with a given significance depending on the level of noise (see e.g. Anglada-Escudé et al. 2013). The signal at 145 d does not appear in the periodogram of the RV data. This could be due to the low semi-amplitude of the induced RV rotation signal ($K = 0.67^{+0.28}_{-0.20}$ m s^{-1}), which we compute using Eq. 3.15 with the coefficients provided by Suárez Mascareño et al. (2018a). The upper limit of this semi-amplitude (0.95 m s^{-1}) marginally falls on the detection limit of a big part of the current instrumentation dedicated to RV searches (Pepe et al. 2014a). However, we performed several tests with the published set of RV time series, trying to force a fit for the rotation signal (with both a sinusoid and a Keplerian model), allowing the period to move in the range between 130 d and 160 d. After fitting and subtracting the stellar rotation signal, the 233 d signal

remains highly significant in the periodogram of the residuals. We note that 77 d is about half of the estimated rotation period from activity indicators but we do not find any signal in the RV time series at about 145 d. After fitting and subtracting the 77 d signal, the 233 d signal still holds with high power. The combined fit of the 77 d + 233 d signals does not affect the final parameters of the planet reported in Ribas et al. (2018). We conclude that the planetary signal at 233 days is not related to any possible rotation signal present in the RV data, which we have not been able to detect since it is probably much weaker than the RV precision of the data.

3.6 Activity study of HADES and RoPES samples

With the experience gained with the activity analysis of Barnard's Star, we then proceed to analyze the complete sample of our HADES and RoPES programs. The HADES sample contains 79 M dwarfs which we had been monitoring with HARPS-N at the TNG. We focus on the sub-spectral types between M0 and M3 because otherwise the low visible flux and high activity jitter would make the planetary detections very challenging. An extensive chemical abundances analysis of this sample can be found in Maldonado et al. (2020). The RoPES sample contains 30 nearby equatorial solar-type and K-type stars with low chromospheric activity which we monitored using both HARPS-N (with ongoing observations) and HARPS (with archive data and future new data based on the LFC). The objective of both programs is the detection of planetary companions, with special interest in low-mass planets located in the habitable zone. The planetary discoveries made by both programs will be discussed in Chapter 5.

3.6.1 Observations

During the course of this thesis, we had carried out 17 campaigns of observations across 60 nights at the TNG to obtain spectra of the stars of both programs. The spectra acquired add to the previous observations that have been taken since 2012 (in the case of HADES) and 2014 (in the case of RoPES). For these acquisitions, we used an exposure time of 900 s per spectra to average out the short-time periodic oscillations of the star (Dumusque et al. 2011). In the case of the stars of the RoPES program, we split the exposure into 3 takes to avoid saturation effects. Table 3.4 and Table 3.5 show the principal information of the star sample from both programs analyzed in this thesis.

TABLE 3.4— Main characteristics of the stars from the RoPES program.

Star	Spectral Type	m_V	N_{spec} HARPS-N	N_{spec} HARPS	Time-span [d]	$log_{10}(R'_{HK})$
HD 161098	G8V	7.67	383	155	4576	-4.868 ± 0.020
HD 170493	K4V	8.00	295	51	4829	-4.868 ± 0.087
HD 203384	G5V	8.02	280	21	5105	-4.971 ± 0.043
HD 210277	G8V	8.57	273	41	5229	-4.960 ± 0.019
HD 220339	K2V	7.80	293	35	5505	-4.849 ± 0.059
HD 4915	G5V	6.97	286	60	5526	-4.797 ± 0.027
HD 7438	K1V	7.87	268	31	3966	-4.659 ± 0.081
HD 8389	K0V	7.84	277	33	5501	-5.081 ± 0.050
HD 12264	G5V	7.98	224	35	2600	-4.648 ± 0.037
HD 176986	K2.5V	8.45	329	170	5202	-4.837 ± 0.039
HD 197210	G5V	7.61	298	19	4840	-4.857 ± 0.028
HD 204941	K2V	8.48	219	96	5056	-4.932 ± 0.039
HD 220256	K1V	8.57	291	26	5524	-4.949 ± 0.045
HD 7134	G1V	7.48	250	24	5505	-4.937 ± 0.019
Eps Eri	K2V	3.73	626	548	5405	-4.454 ± 0.030
HD 20165	K1V	7.80	241	0	1553	-4.908 ± 0.056
HD 146233	G2V	5.50	18	2880	4489	-4.867 ± 0.017
HD 212657	F7V	8.24	33	0	113	-4.974 ± 0.049
HD 213575	G5V	6.95	39	24	5507	-4.970 ± 0.028
HD 218566	K3V	9.21	42	21	906	-4.554 ± 0.030
HD 3651	K0.5V	5.88	12	0	24	-4.943 ± 0.020
HD 4628	K2.5V	5.74	9	182	5418	-4.967 ± 0.023
BD+10 125	G0V	9.54	36	2	780	-4.894 ± 0.047
HD 16160	K3V	5.83	9	232	5418	-4.987 ± 0.038

Columns: Star name, spectral type, V-band magnitude, number of HARPS-N measurements, number of HARPS measurements, time-span of the combined dataset, and level of chromospheric activity.

TABLE 3.5— Main characteristics of the stars from the HADES program.

Star	Spectral Type	m_V	N_{spec} HARPS-N	N_{spec} HARPS	Time-span [d]	$log_{10}(R'_{HK})$
Gl 49	M1.5V	9.56	118	0	2151	-4.934 ± 0.061
GJ 2	M2V	9.97	92	0	1742	-4.908 ± 0.055
GJ 21	M1V	10.56	117	0	1761	-4.805 ± 0.054
GJ 119 A	M1V	10.46	132	0	1930	-4.792 ± 0.052
GJ 47	M2V	10.87	87	0	1930	-4.946 ± 0.084
GJ 1030	M0V	11.40	19	5	3012	-4.900 ± 0.050
GJ 4306	M1V	10.56	145	3	1599	-4.373 ± 0.051
GJ 16	M1V	10.68	125	8	4010	-5.571 ± 0.071

Star	Spectral Type	m_V	N_{spec} HARPS-N	N_{spec} HARPS	Time-span [d]	$log_{10}(R'_{HK})$
GJ 26	M2.5V	11.24	55	0	2245	-4.934 ± 0.068
Gl 15 A	M2V	8.13	115	0	1581	-5.492 ± 0.062
GJ 908	M1V	8.99	42	86	5243	-5.368 ± 0.075
GJ 9793	M0V	10.51	30	0	1567	-4.600 ± 0.059
GJ 9122 B	M0V	10.76	122	0	2151	-4.950 ± 0.061
GJ 1074	M1V	10.93	54	0	2071	-4.964 ± 0.060
GJ 184	M0.5V	10.06	87	0	2071	-5.937 ± 0.070
GJ 9689	M0.5	11.23	157	3	2008	-4.905 ± 0.062
StKM 1-1877	M1.5V	11.69	72	0	1593	-4.427 ± 0.067
GJ 625	M1.5V	10.17	154	0	1921	-5.936 ± 0.185
GJ 3942	M0.5V	10.25	141	0	1374	-4.529 ± 0.052
GJ 685	M1V	9.97	106	0	1605	-4.738 ± 0.051
GJ 720 A	M0.5V	9.83	113	0	1968	-5.066 ± 0.055
GJ 694	M2V	10.49	148	0	1599	-5.344 ± 0.065
GJ 3998	M1V	10.83	187	6	3439	-5.106 ± 0.049
Gl 686	M1.5V	9.58	64	20	4888	-5.468 ± 0.069
GJ 4092	M0.5V	10.86	53	13	4006	-4.900 ± 0.080
GJ 3997	M0.5V	10.37	122	0	2212	-5.197 ± 0.060
GJ 740	M1V	9.37	129	57	4003	-4.880 ± 0.050
GJ 3822	M1V	10.64	53	68	3899	-4.802 ± 0.059
GJ 4057	M0V	10.77	145	0	1968	-5.073 ± 0.062
GJ 119 B	M2.5V	11.70	10	0	1481	-4.891 ± 0.048
GJ 3117 A	M2.5V	11.51	12	0	1210	-4.832 ± 0.052
GJ 70	M2V	10.92	27	9	1906	-5.346 ± 0.074
G 214-14	M2.5V	11.55	31	0	1565	-5.380 ± 0.078
GJ 162	M2.5	11.19	79	0	1810	-3.746 ± 0.073
GJ 9138	M1.5V	10.64	106	0	1784	-4.966 ± 0.060
GJ 272	M1V	10.53	12	0	1483	-5.242 ± 0.088
GJ 3352	M1V	11.07	12	0	1483	-4.525 ± 0.041
G 234-57	M1V	11.30	43	0	1721	-4.692 ± 0.083
StKM 1-587	M0.5V	11.43	11	0	1393	-4.849 ± 0.122
BPM 96441	M0V	11.90	17	0	1295	-4.722 ± 0.045
StKM 1-650	M0.5V	12.03	19	0	1521	-4.629 ± 0.056
GJ 521	M1V	10.26	145	0	1594	-4.790 ± 0.057
GJ 793	M3V	10.68	27	0	1168	-5.142 ± 0.114
GJ 552	M2.5V	10.68	105	8	1590	-5.204 ± 0.058
GJ 507.1	M2V	10.55	122	0	1594	-5.364 ± 0.068
GJ 414 B	M2V	9.98	36	0	1367	-5.453 ± 0.043
GJ 412 A	M1V	8.78	101	0	1559	-5.511 ± 0.096
GJ 408	M2.5V	10.02	49	0	1332	-5.492 ± 0.088
GJ 450	M1.5V	9.80	40	0	1530	-4.920 ± 0.093
GJ 9404	M0.5V	10.64	54	0	1432	-4.771 ± 0.057
GJ 606	M1V	10.49	29	24	3775	-4.973 ± 0.067
GJ 548 A	M3V	9.72	35	0	909	-4.841 ± 0.051

Star	Spectral Type	m_V	N_{spec} HARPS-N	N_{spec} HARPS	Time-span [d]	$log_{10}(R'_{HK})$
GJ 731	M0V	10.10	35	0	1425	-5.063 ± 0.056
GJ 2128	M2.5V	11.53	25	6	3055	-5.555 ± 0.078
GJ 399	M2.5V	11.28	37	8	3283	-5.243 ± 0.094
GJ 476	M1V	11.41	16	38	4686	-5.307 ± 0.059

The $log_{10}(R'_{HK})$ shown in Table 3.4 and Table 3.5 was computed from the combined HARPS and HARPS-N dataset with their respective offset applied. The spatial distribution of the stars listed in these tables is shown in Fig. 3.15.

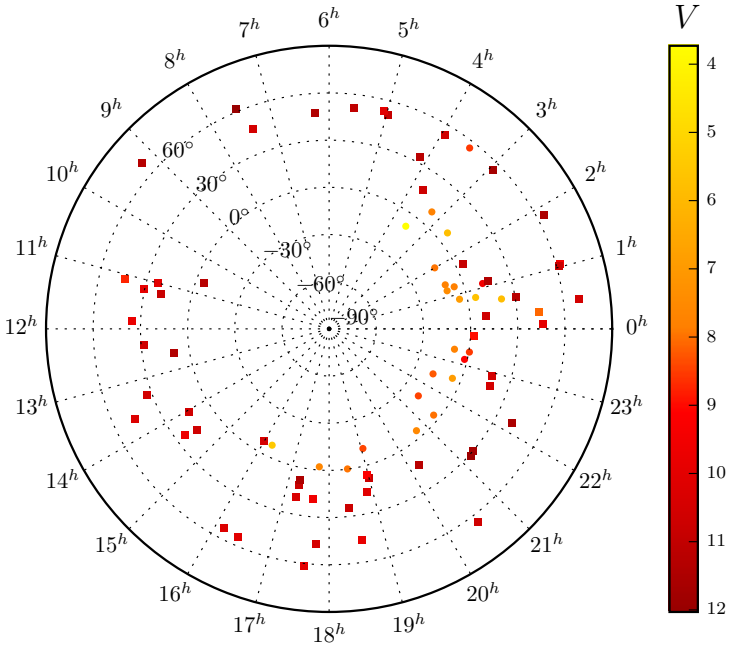

FIGURE 3.15— Coordinate distribution of the star sample from the HADES and RoPES programs represented with squares and circle points, respectively. The color of the points indicates the V-magnitude of the star according to the color bar on the right side.

3.6.2 Methodology

An analysis on the individual datasets (HARPS-Pre2015, HARPS-Post2015, and HARPS-N) was first carried out using three chromospheric indices (Hα, S_{mw}, and NaD) computed for the bi-dimensional and one-dimensional spectra, and three CCF-related indices (RV, FWHM, and BIS). We used the Systemic console for a first visualization of the GLS periodogram of each time series. Then we fitted the most significant peak in these periodograms with a second-order polynomial or a single sinusoidal in the case of the long-term signals and a double sinusoidal in the case of the short-term signals. We carried out the pre-whitening process and then isolated each signal individually. In each subtraction, the FAP levels were recomputed through bootstrapping to ensure the statistical significance of the signals. We then added the additional datasets available with their respective offsets and repeated the whole process. To be able to perform this analysis on such a large sample, the algorithms implemented have been parallelized using the IAC supercomputing facility HTCondor[6]. This tool allows the exploitation of the computational resources of the IAC to minimize the computational time of the codes launched from an individual machine.

We compared the RV signals detected with the ones found in the rest of the indices. We then studied the RV residuals to search for signals that could arise from an orbiting exoplanet. The planetary discoveries will be later described in Chapter 5. The activity analysis was done in conjunction with the one that we published on Suárez Mascareño et al. (2018a), where the main results for the HADES sample are shown.

3.6.3 Magnetic cycles and rotation signals

Within the HADES collaboration, Suárez Mascareño et al. (2018a) reported the $log_{10}(R'_{HK})$ measurements for the complete M-dwarf sample of the program (the values shown in Table 3.5 are updated with the new spectra taken since the publication of that paper). We presented the detection of 33 new rotation signals and 18 new magnetic cycle signals. These results were complemented with 16 new RV induced rotation signals and 36 estimations of the rotation period and amplitude of this type of signals using Eq. 3.15. To achieve this, we complemented the spectroscopic analysis with a photometric study using light curves from the ASAS survey.

This study helped us to refine the activity-rotation relation of Eq. 3.14 and the activity-RV semi-amplitude relation of Eq. 3.15 with a large sample

[6] http://research.cs.wisc.edu/htcondor/

of M dwarfs. For Eq. 3.14, we found a saturation limit at $log_{10}(R'_{\rm HK}) \sim -4.0$ previously reported by Astudillo-Defru et al. (2017a). This can be shown in Fig. 3.16, where we have represented how this relationship fits a combined sample of stars from Suárez Mascareño et al. (2015), Suárez Mascareño et al. (2016), Suárez Mascareño et al. (2018a), Suárez Mascareño et al. (2018b) and Astudillo-Defru et al. (2017a).

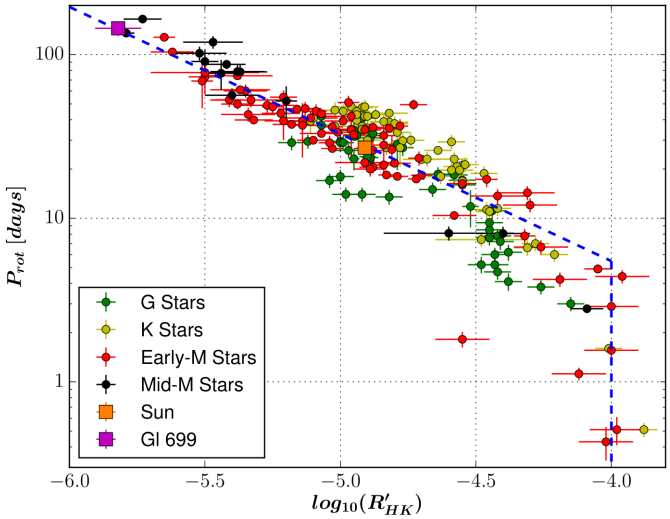

FIGURE 3.16— Rotation period and chromospheric activity level of a G, K, Early-M (M0 to M3), and Mid-M (M4 to M6) star sample from the literature, including Barnard's Star. Figure taken from Toledo-Padrón et al. (2019).

The blue line of Fig. 3.16 represents the relation obtained by Suárez Mascareño et al. (2018a) for M-type stars. In the paper, we observed a different behavior between Early-M (M0 to M3) and Mid-M (M4 to M6) stars. For Eq. 3.15 we did not find this difference, but the relatively low number of induced RV rotation signals detected points out that a larger sample of M dwarfs is needed to constrain better the relationship between the semi-amplitude of these signals and the level of chromospheric activity.

4

Planetary characterization

We've always defined ourselves by the ability to overcome the impossible. And we count these moments. These moments when we dare to aim higher, to break barriers, to reach for the stars, to make the unknown known. We count these moments as our proudest achievements. But we lost all that. Or perhaps we've just forgotten that we are still pioneers. And we've barely begun. And that our greatest accomplishments cannot be behind us, because our destiny lies above us.
Joseph Cooper, Interstellar

We have already reviewed the characteristics of the stellar activity signals, the different indicators and models used to trace them, and the derived relations from their properties. Therefore we can now start studying the signals induced by planetary companions.

4.1 Exoplanet database

Across more than 25 years of research, the total number of known exoplanets has been increasing exponentially up to over 4400 detections. The majority of these objects (96 %) have been discovered through the Transit (76 %) and RV (19 %) techniques. Regarding the spectral type of their parent star, the G-, K- and M-type stars gather 85 % of the total detections (their respective percentages are 35 %, 29 %, and 21 %). Of these planets, 407 have an Earth-like radius (i.e., $R_{\rm p} < 1.25\,R_{\oplus}$) and only 48 have an Earth-like mass (i.e., $M_{\rm p} < 2\,M_{\oplus}$). The most common types of planets in our galaxy are super-Earths

(i.e., $1.25\,R_\oplus < R_\mathrm{p} < 2\,R_\oplus$ and $2\,M_\oplus < M_\mathrm{p} < 10\,M_\oplus$) and sub-Neptunes (i.e., $2\,R_\oplus < R_\mathrm{p} < 3\,R_\oplus$ and $10\,M_\oplus < M_\mathrm{p} < 17\,M_\oplus$). These statistitics are displayed in Fig. 4.1.

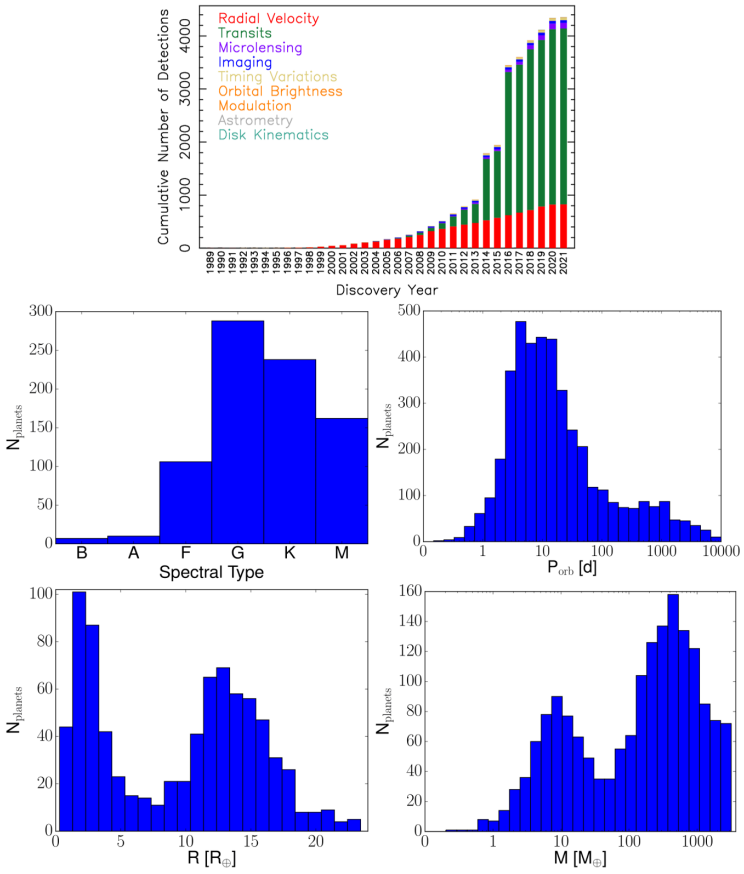

FIGURE 4.1— Planetary statistics (source: NASA database). **Top:** Cumulative detections per year of the different detection methods. **Center Left:** Distribution of parent stars' spectral types. **Center Right:** Distribution of orbital periods. **Bottom Left:** Distribution of planetary radius. **Bottom Right:** Distribution of planetary masses.

In Fig. 4.1 we have also included the distribution of the orbital period of the detected exoplanets, which presents its maximum in the short-period region. This result is affected by the lower semi-amplitude of the RV induced signals produced by long-period planets and the decrease of the transit probability with the orbital distance, along with time limitations in the surveys used. In photometric transit photometry searches, the *Kepler* telescope (the main reference in this field prior to the launch of TESS) presents a detection limit at $P \simeq 200\,\mathrm{d}$ and $R_\mathrm{p} \simeq 1.25\,R_\oplus$ (Bryson et al. 2020), since planets with longer orbital periods only transit twice as maximum within the observational baseline. The stellar jitter and RV precision of the current echelle spectrographs are the two main obstacles that affect the sample of exoplanets detected by RV.

Since 2005, several studies have been conducted to analyze the occurrence rate of exoplanets (see e.g. Marcy et al. 2005; Cumming et al. 2008; Borucki et al. 2011; Howard et al. 2012; Fressin et al. 2013; Gaidos et al. 2016; Hsu et al. 2019). These studies have revealed very promising results, such as an average of ~ 2.5 planets per M-type star in the $P < 200\,\mathrm{d}$ and $R_\mathrm{p} = 1$–4 $\mathrm{R}_\oplus$ regime (Dressing & Charbonneau 2015), or that 50 % of the Solar-type stars could host an Earth-like planets located in their habitable zone (Bryson et al. 2021). The M dwarfs are the most common stars in the Milky Way (Chabrier & Baraffe 2000; Winters et al. 2015). They are ideal targets for the search of temperate Earth-like planets due to their lower luminosities which produce closer habitable zones, along with their lower masses, which are connected to greater semi-amplitudes of the RV signals caused by their planetary companions. However, the complexity of the characteristic stellar activity pattern of these stars requires a careful analysis of the chromospheric activity indicators in order to identify false planetary signals induced by the rotation of the star (Bonfils et al. 2007; Robertson et al. 2014) as described in the previous Chapter (Suárez Mascareño et al. 2018a; Toledo-Padrón et al. 2019). Regardless of the spectral type of the host star, those RV signals not classified as false positives by this process need to be properly modeled.

4.2 Planetary modeling

A Keplerian fit like the following one is normally used to model the planetary signals found in the RV time series (Delisle et al. 2016):

$$y(t) = K\,(\cos(\nu + \omega) + e\ \cos(\omega)) \tag{4.1}$$

where ν is the true anomaly related to the solution of the Kepler equation that depends on the orbital period of the planet P and the orbital phase ϕ.

This phase corresponds to the periastron time, which depends on the mid-point transit time T_0, the argument of periastron ω, and the eccentricity of the orbit e. The parameters of the Keplerian function can be fitted using tools like `RVLIN` (Wright & Howard 2012), although the more adequate approach requires Monte Carlo Markov Chain (MCMC) simulations. These simulations are performed within a Bayesian framework to infer the probability distribution over all the parameters considered. This method requires priors for all of these parameters, along with a convergence criterion based on the auto-correlation function that ensures that the parameter distributions are correct. This approach is particularly useful when the planetary modeling is performed along with activity models based on GP. To exemplify the process of characterization of planetary signals we will use our study of the planetary system around the solar-type K2-38 (Toledo-Padrón et al. 2020).

4.3 Characterization of the K2-38 planetary system

Crossfield et al. (2016) reported the discovery of two planetary companions around K2-38, which were first characterized by Sinukoff et al. (2016) using 14 HIRES spectra. The first planet (K2-38 b) is a high-density super-Earth ($R_\mathrm{p} = 1.55 \pm 0.16$ R$_\oplus$ and $M_\mathrm{p} = 12.0 \pm 2.9$ M$_\oplus$) with an orbital period of 4 d, and the second planet (K2-38 c) is a low-density sub-Neptune ($R_\mathrm{p} = 2.42 \pm 0.29$ R$_\oplus$ and $M_\mathrm{p} = 9.9 \pm 4.6$ M$_\oplus$) with a period of 10.6 d. The masses provided by the preliminary RV analysis of Sinukoff et al. (2016) indicated that K2-38 b could be the densest planet known to date due to its bulk density of $\rho_\mathrm{p} = 17.5\,^{+8.5}_{-6.2}$ g cm^{-3}. The system is composed by the two most common types of exoplanets. One of the most relevant differences that separates these two objects in close-in orbits is the existence of radius valley between them (Owen & Wu 2013; Lopez & Fortney 2013; Chen & Rogers 2016; Fulton et al. 2017). We took advantage of the high RV precision provided by ESPRESSO to study how this system fits into the radius valley scenario, improve the mass measurement of the two planets (along with other properties), and explore the mass-radius relation in terms of the incident stellar flux.

4.3.1 Dataset

We acquired 43 ESPRESSO spectra of K2-38 at the VLT as part of the Guaranteed Time Observation of this instrument, including a physical visit of 4 nights in September of 2019. This dataset was obtained using the 1-UT mode and is characterized by a time-span of 240 d and a mean S/N per extracted pixel at 550 nm of 56.1. The RVs and activity indicators were computed using the

public version of the ESPRESSO pipeline Data-Reduction-Software (DRS)[7]. The CCFs were computed using a G2 mask and an RV step of 0.5 $\mathrm{km\,s^{-1}}$ within a range between -55 and -15 $\mathrm{km\,s^{-1}}$ centered on the systemic velocity of the star. We achieved an RV precision of 1.0 $\mathrm{m\,s^{-1}}$ with 3.6 $\mathrm{m\,s^{-1}}$ of RMS, which shows the better performance of ESPRESSO in comparison with other spectrographs.

We complemented this dataset with the 14 HIRES RV measurements published by Sinukoff et al. (2016) which are characterized by a time-span of ~ 100 d, a RV precision of 1.5 $\mathrm{m\,s^{-1}}$ and a RMS of 5.2 $\mathrm{m\,s^{-1}}$.

For the photometric study, we downloaded the available K2 photometric light curve obtained by the *Kepler* mission (Howell et al. 2014) taken in the long cadence mode, which is characterized by 30-min integration time. This photometric dataset covers a time-span of 78 d (one *Kepler* quarter) within Campaign 2 of the K2 mission.

Additionally, we also included the available ASAS-SN photometric observations of K2-38 (Kochanek et al. 2017) in our photometric analysis. The ASAS-SN light curve covers nearly 8 consecutive years preceding the ESPRESSO spectra. K2-38 lies at a relatively high Galactic latitude ($b = +22$ deg) and does not have any other bright stars in its surroundings, which guarantees that the ASAS-SN photometry is not contaminated by nearby stars. The dispersion of the g- and V-band used to obtain the light curves is 33 and 62 mmag, respectively (after removing the few most deviant data points).

4.3.2 Stellar characterization

K2-38 is a $V = 11.34$ high-proper motion G2-type star (Henden et al. 2016) located at 194 pc from the Sun (Gaia Collaboration et al. 2018). Prior to the characterization of its planetary system, we performed a stellar parameter analysis and a chemical abundances study.

Stellar parameters

To obtain the stellar parameters of K2-38, we first coadded the blaze-corrected bi-dimensional ESPRESSO spectra at the barycentric reference frame. Then we normalized, merged, and corrected them for RV using the StarII workflow of the Data Analysis Software (DAS) of ESPRESSO (Di Marcantonio et al. 2018). The final RV-corrected normalized 1D ESPRESSO spectrum of K2-38 is shown in Fig. 4.2.

[7] `https://www.eso.org/sci/software/pipelines/espresso/espresso-pipe-recipes.html`

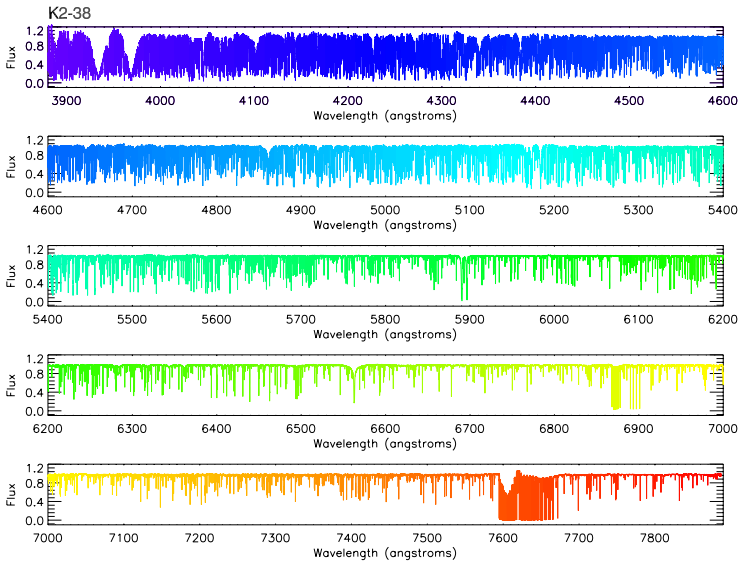

FIGURE 4.2— Normalized 1D ESPRESSO spectrum of K2-38 corrected from RV. Five different spectral regions are shown in different colors changing from blue to red as the wavelength increases from bluer to redder wavelengths. Figure taken from Toledo-Padrón et al. (2020).

We derived the effective temperature $T_{\rm eff}$, surface gravity $\log g$, microturbulence ξ, and metallicity [Fe/H] of K2-38 using the ARES+MOOG method (Sousa 2014). The spectral analysis to obtain these stellar atmospheric parameters is based on the excitation and ionization balance of iron. The EWs of these lines were consistently measured with the ARES (v2) code (Sousa et al. 2007; Sousa et al. 2015), deriving the abundances in local thermodynamic equilibrium (LTE) with the spectral synthesis code MOOG (v2014) (Sneden 1973). Using a grid of plane-parallel Kurucz ATLAS9 model atmospheres (Kurucz 1993) with the line list from Sousa et al. (2008), we obtained the parameters shown in Table 4.1. We cross-checked these results using the StePar code (Tabernero et al. 2019) based on the MARCS models (Gustafsson et al. 2008), the MOOG code (2017 version) and the TAME code (Kang & Lee 2012).

TABLE 4.1— Stellar properties of K2-38.

Parameter	K2-38	Reference
RA (J2000)	16:00:08.06	[1]
Dec (J2000)	−23:11:21.33	[1]
$\mu_\alpha \cos\delta$ [mas yr^{-1}]	-57.00 ± 0.10	[1]
μ_δ [mas yr^{-1}]	-37.63 ± 0.06	[1]
Parallax (mas)	5.16 ± 0.07	[1]
Distance [pc]	$193.6\ ^{+2.7}_{-2.5}$	[2]
$m_{\rm B}$	12.27 ± 0.13	[3]
$m_{\rm V}$	11.39 ± 0.03	[3]
Spectral type	G2V	[4]
Age [Gyr]	$6.7\ ^{+2.4}_{-3.0}$	[2]
$T_{\rm eff}$ [K]	5731 ± 66	[2]
[Fe/H] [dex]	0.26 ± 0.05	[2]
$M_\star$ [M$_\odot$]	$1.03\ ^{+0.04}_{-0.02}$	[2]
$R_\star$ [R$_\odot$]	$1.06\ ^{+0.09}_{-0.06}$	[2]
$L_\star$ [L$_\odot$]	1.09 ± 0.15	[1]
$\log g$ (cgs)	4.38 ± 0.11	[2]
ξ [km s^{-1}]	0.98 ± 0.04	[2]
A_V	$0.15\ ^{+0.16}_{-0.14}$	[2]
$v \sin i$ [km s^{-1}]	<2	[4]
$\log_{10}(R'_{\rm HK})$	-5.06 ± 0.13	[2]

References: [1] Gaia Collaboration et al. (2018); [2] Toledo-Padrón et al. (2020); [3] Henden et al. (2016); [4] Sinukoff et al. (2016)

The mass and radius shown in Table 4.1 were computed using the PARAM code (da Silva et al. 2006; Rodrigues et al. 2017). We matched three of the stellar parameters previously obtained ($T_{\rm eff}$, $\log g$, and [Fe/H]), along with the *Gaia* DR2 parallax and the V magnitude published in the literature (Henden et al. 2016), to a grid of stellar evolutionary tracks and isochrones from PARSEC (Bressan et al. 2012). The optimization method is based on the PARAM2 implementation (Rodrigues et al. 2014), which provides posterior probability distribution functions for the stellar properties using a set of input parameters that are considered at once. The method uses the absolute magnitude computed through the model along with the apparent magnitude to derive the distance of the star and the extinction coefficient. For consistency, we also derived the mass and radius of K2-38 using the Torres et al. (2010) calibration. We obtained compatibles values, within the error bars, with the ones estimated from the isochrone analysis.

Chemical abundances

Using the stellar parameters of Table 4.1 we also measured the element abundances of C, O, Mg, and Si using the MOOG and ARES tools by following the methodology described in Adibekyan et al. (2015) and Adibekyan et al. (2016). As previously described, we calculated the chemical abundances of these elements from the EWs of each spectral line, using the LTE code MOOG (Sneden 1973) with an appropriate ATLAS model atmosphere (Kurucz 1993) of K2-38. The final abundances were computed as the average value of individual element abundances. The errors were estimated from the sensitivities of the element abundances to the uncertainties on the stellar parameters added quadratically to the dispersion from the individual element abundances. We derived the following abundances: $[C/H] = 0.21 \pm 0.06$, $[O/H] = 0.18 \pm 0.07$, $[Mg/H] = 0.24 \pm 0.05$, $[Si/H] = 0.27 \pm 0.06$. The atomic line parameters including oscillator strengths of spectral lines of MgI and SiI were taken from Adibekyan et al. (2012). The oxygen abundances were determined using two weak lines at 6158.2 Å and 6300.3 Å following the work of Bertran de Lis et al. (2015). Carbon abundances were based on the two well-known C I optical lines at 5052 Å and 5380 Å. The atomic data of these lines were extracted from VALD3 database[8].

Dorn et al. (2015) proposed that Mg/Si and Fe/Si ratios can be used as probes to constrain the internal structure of terrestrial planets. Santos et al. (2015) successfully tested this on three terrestrial planets with a model later used to explore the possible compositions of planet-building blocks and planets orbiting stars belonging to different Galactic populations (Santos et al. 2017). We transformed the chemical abundances of C, O, Mg, Si, and Fe relative to the Sun to absolute abundances accepting the solar reference abundances as given in Asplund et al. (2009) for Fe ($\log \epsilon = 7.5$ dex), Mg ($\log \epsilon = 7.60$ dex), and Si ($\log \epsilon = 7.51$ dex), and as given by Bertran de Lis et al. (2015) and Suárez-Andrés et al. (2017) for O ($\log \epsilon = 8.71$ dex) and C ($\log \epsilon = 8.50$ dex). By using these absolute abundances we applied the aforementioned stoichiometric model of Santos et al. (2015) to determine the iron-mass fraction and water-mass fraction of the planet building blocks in the planetary disks of the star. Our model suggests an iron-mass fraction of 33.4 ± 3.3 % and water-mass fraction of 51.9 ± 5.9 %. This model predicts an iron-mass fraction of 33 % and water-mass fraction of 60 % for the solar system planet building blocks (Santos et al. 2017). These results may have implications on the possible bulk composition of the planets formed in the planetary system of K2-38, although they are not directly applicable to the final composition or internal structure of a

[8] http://vald.astro.univie.ac.at/~vald3/php/vald.php?newsitem=0

final differentiated planet, which depend on several factors such as the position in the proto-planetary disk where the planet is formed and its migration path. Additionally, some physical processes, such as evaporation and collisional stripping, may change the overall composition of planets.

4.3.3 Photometric analysis

For the analysis of the K2-38 planetary system, we first studied the ASAS-SN light curves. The GLS periodograms of these light curves show a long-term trend (>1000-2000 d). When this trend is removed with a linear fit, the remaining periodograms show no significant peaks above the 10 % FAP level. To improve the S/N detection of any periodic signal we also computed the GLS periodogram of the merged g- and V-band light curves, obtaining a similar result: no strong peak between 2 and 1000 days. We concluded that ASAS-SN data confirm that K2-38 is photometrically inactive above 30–60 mmag ($1\,\sigma$) for nearly 8 years of observations before the ESPRESSO measurements.

We then analyzed the K2 light curve to search for the photometric signals of the planets. To detrend this light curve we used the `everest` code (Luger et al. 2016; Luger et al. 2018), which has been proved to provide better results in terms of flux scatter in comparison with other pipelines (Hirano et al. 2018). This code performs a flux correction based on a single co-trending basis vector (CBV). We performed a sigma-clipping procedure to these flux values using a 2.5σ in order to remove outliers. We also discarded the photometry taken in the Barycentric Julian Date (BJD) range between BJD = 2456926.85 and BJD = 2456930.62 due to a flare event. Finally, we used a moving average to clean the light curve from the small-scale outliers.

Then we carried out a transit analysis using the `exotrending` code (Barragán & Gandolfi 2017). We used the period and epoch of transit provided by Sinukoff et al. (2016) for both known planets as input parameters and applied the model from Mandel & Agol (2002). Assuming a quadratic law for the limb-darkening (Claret 2000) based on two coefficients γ_1 and γ_2, we obtained the results shown in Fig. 4.3. The light curve shown in the top panel of Fig. 4.3 exhibits a low-frequency modulation which is related to the CBV correction made by `everest` and not connected to the stellar activity of the star since it is not present in the light curve obtained with other detrending tools. The brightness dips shown in the bottom panel of Fig. 4.3 are related to a $R_{\rm p} = 1.54 \pm 0.14$ R$_\oplus$ for planet b and $R_{\rm p} = 2.29 \pm 0.26$ R$_\oplus$ for planet c according to Eq. 1.1. These values are in good agreement with those reported in Sinukoff et al. (2016), with the difference between both studies coming from the improved star radius used in our work.

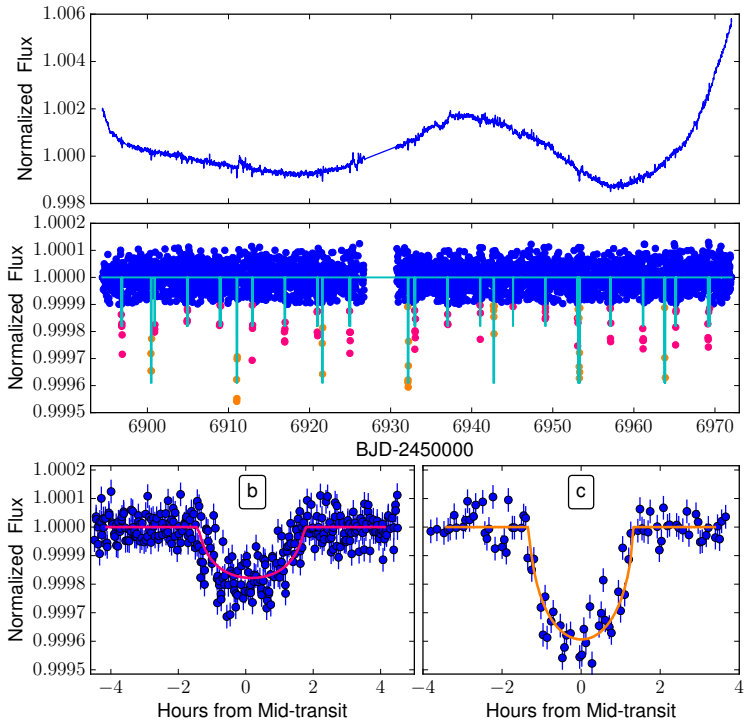

FIGURE 4.3— **Top:** Normalized flux of the light curve extracted using the `everest` pipeline. **Middle:** Detrended light curve with the transits of K2-38 b and K2-38 c marked in pink and orange, respectively. **Bottom:** Folded light curve using the period of K2-38 b (P = 4.02 d) and K2-38 c (P = 10.56 d). Figure taken from Toledo-Padrón et al. (2020).

4.3.4 Spectroscopic analysis

For the spectroscopic analysis, we used the DACE interface[9] of the ESPRESSO pipeline to compute the RVs, the FWHM of the CCFs, and chromospheric activity indicators (H_α, S_{mw}, and NaD). These time series are shown in Fig. 4.4.

[9] `https://dace.unige.ch`

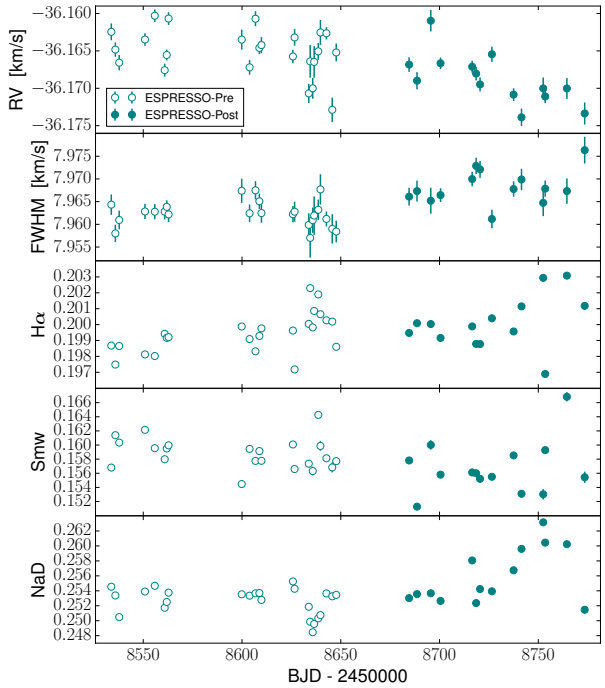

FIGURE 4.4— Time series of the RVs and stellar indices obtained with the ESPRESSO pipeline: RV, FWHM, H_α, S-index, and NaD index. Figure taken from Toledo-Padrón et al. (2020).

We split the ESPRESSO dataset into two subsets due to the maintenance operations carried out in the instrument on the last weeks of June 2019 to update its fiber link that produce an offset in the RV measurements (Pepe et al. 2021).

Stellar activity

Using the S_{mw} time series shown in Fig. 4.4 we calculated a chromospheric activity level of $\log_{10}(R'_{HK}) = -5.06 \pm 0.13$, which according to Eq. 3.14 is related to an expected rotation period of $P_{rot} = 29 \pm 2$ d.

The stellar activity analysis of the spectroscopic indices H_α, S_{MW}, NaD, and FWHM shown in Fig. 4.4 reveals that all the signals in the GLS periodograms had a significance below the 10 % level (i.e., no significant periodicity was detected in any of the datasets). This points out the fact that the rotation signal may have an amplitude lower than the RMS of the data. The time-span of observations does not cover the typical timescale of signals associated with long-term magnetic cycles, and therefore, we cannot assess their presence on this star with the current dataset. We performed a GP analysis based on the `celerite` code (Foreman-Mackey et al. 2017) in the four time series separately using the quasi-periodic kernel from Eq. 3.5. We introduced an additional jitter term for each dataset, which leads to the use of two kernels (one for each dataset) with the same rotation parameters. We set up our GP model as a combination of these two kernels with boundaries for all the parameters. We used the expected rotation value derived from the $log_{10}(R'_{HK})$ index as the first guess for P_{rot}, and the double of this value as the first guess for t_s (Giles et al. 2017). We then defined our likelihood function including two offset terms to account for the zero-point of each dataset. We minimized this function using the `minimize` python module included in the `scipy.optimize` package. The parameters obtained from this analysis performed on the four time series did not provide any clear rotation value for the star. We also carried out an MCMC analysis on these time series using the `emcee` python code (Goodman & Weare 2010; Foreman-Mackey et al. 2013). We established priors based on the results from the previous `minimize` analysis, but the rotation parameters did not converge to a clear value. We repeated this GP analysis on the RV time series and we did not find any conclusive result regarding the activity of the star.

Planetary characterization

Due to the lack of a good characterization of the rotation of K2-38, we opted for simplifying our activity model, maintaining only the jitter terms. We performed two separate analyses on the RV time series using the `minimize` and `emcee` packages in each one of them. We repeated the two-step structure carried out in the stellar indices time series, using first the `minimize` package to obtain preliminary results that are considered to establish the priors for the `emcee` package. For the MCMC analysis, we defined a sample of 512 walkers, running first a burn-in chain with 10 000 steps, followed by a construction chain with 50 000 steps.

We first modeled the RV time series with a quadratic polynomial to account for a visible trend in the time series, along with two offset terms to account for the zero-point of each dataset. The subtraction of this model leaves an RMS

in the residuals of 2.61 $\mathrm{m\,s^{-1}}$. The periodogram of the residuals is shown in Fig. 4.5, where the signal of K2-38 c appears with a FAP close to 1 %.

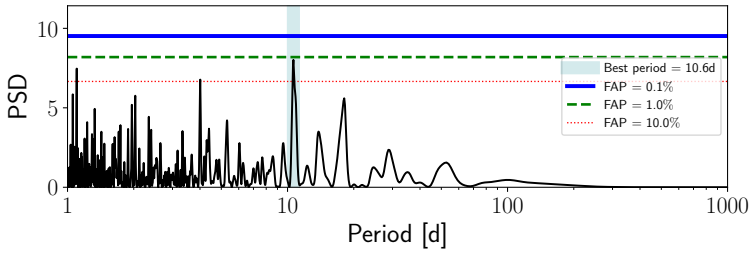

FIGURE 4.5— Periodogram of the residuals of ESPRESSO RV time series after subtracting the trend model.

We modeled this first planetary signal in the original RV time series using the Keplerian from Eq. 4.1 with a fixed period to the photometric transit value ($P_\mathrm{b} = 4.01593 \pm 0.00050$ d). We used the T_0 value from the photometric analysis ($T_0 = 2456896.8786 \pm 0.0054$) and started assuming a circular orbit (i.e., $\omega = 0$ and $e = 0$) for the first guess of the periastron time. We then carried out the minimization of all the parameters (including the new parameters K, ω, and e, and recomputing the previous ones related to the trend, offsets, and jitter) using the original RV time series. The subtraction of this second model lowers the RMS of the residuals to 1.89 $\mathrm{m\,s^{-1}}$. The periodogram of the residuals is shown in Fig. 4.6, where the signal from K2-38 b appears with a FAP below the 1 %.

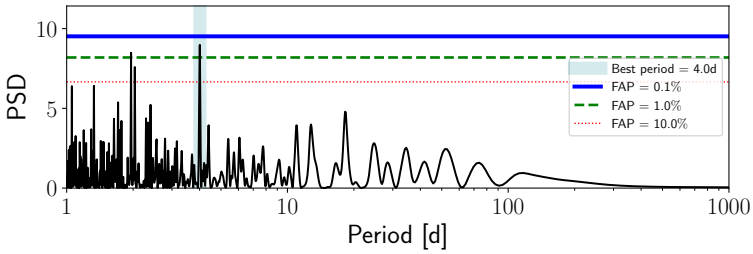

FIGURE 4.6— Periodogram of the residuals of ESPRESSO RV time series after subtracting the model that includes a trend and the planetary signal from K2-38 c.

We included this second planetary signal in our model as a new Keplerian using the period ($P_c = 10.56103 \pm 0.00090$ d) and T_0 ($T_0 = 2456900.4752 \pm 0.0033$ d) from photometry, which adds four new parameters to fit. From the minimization of the 12 parameters based on the original RV time series, we obtained the results shown in Fig. 4.7.

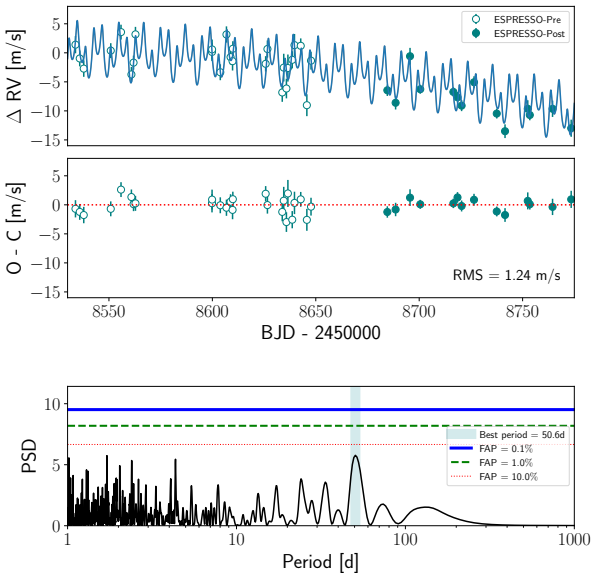

FIGURE 4.7— **Top:** ESPRESSO RV time series with a model that includes a trend and the planetary signals from K2-38 b and K2-38 c. **Center:** Residuals after subtracting the aforementioned model. **Bottom:** Periodogram of the residuals. Figure taken from Toledo-Padrón et al. (2020).

The RMS of residuals after subtracting this model is 1.24 $\mathrm{m\,s^{-1}}$, which is very close to the time series mean photon noise (i.e., mean of internal errors) of 1.14 $\mathrm{m\,s^{-1}}$. The periodogram of the residuals from Fig. 4.7 does not show more significant peaks. We then incorporated the HIRES dataset into the time series with its own offset and jitter terms. In the combined dataset we treated the long-period signal with a sinusoidal since this approach provided a lower RMS in the residuals and better Bayesian evidence $\log Z$ (Perrakis et al. 2013),

which indicates a statistical preference for this model. The minimization of the 15 final parameters led to the results shown in Fig. 4.8.

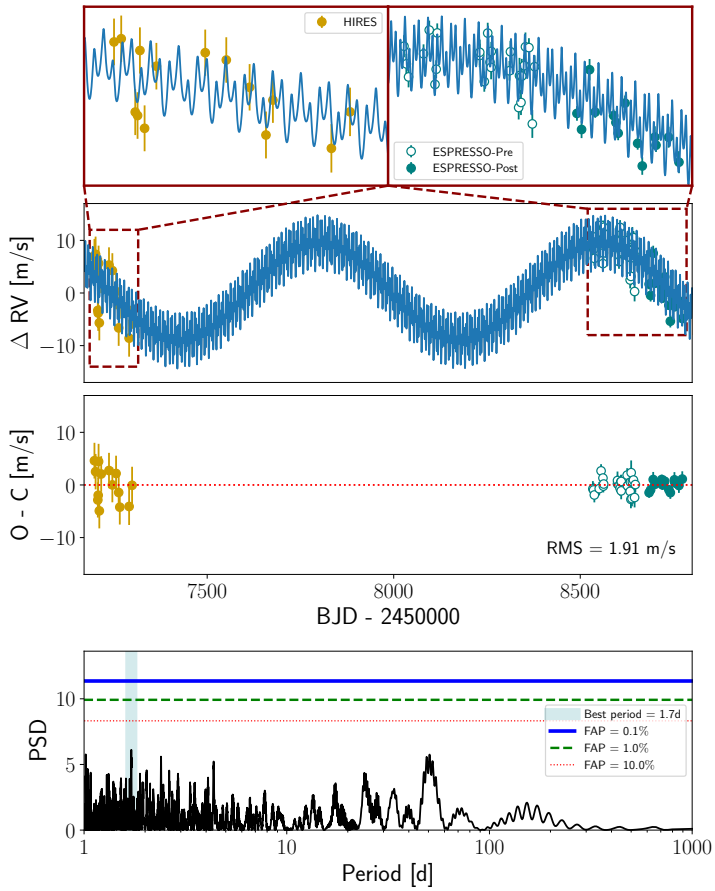

FIGURE 4.8— **Top:** HIRES and ESPRESSO RV time series with a model that includes the long-period signal fitted by a sinusoidal along with the two planetary signals fitted by Keplerians. **Center:** Residuals after subtracting the model. **Bottom:** Periodogram of the residuals. Figure taken from Toledo-Padrón et al. (2020).

This combined treatment provides a higher RMS in the residuals due to the lower quality of the HIRES measurements but puts better constraints on the long-period signal. The individual phase-folded RV models of the two planets and their parameter distribution from the MCMC analysis are shown in Fig. 4.9 and Fig. 4.10.

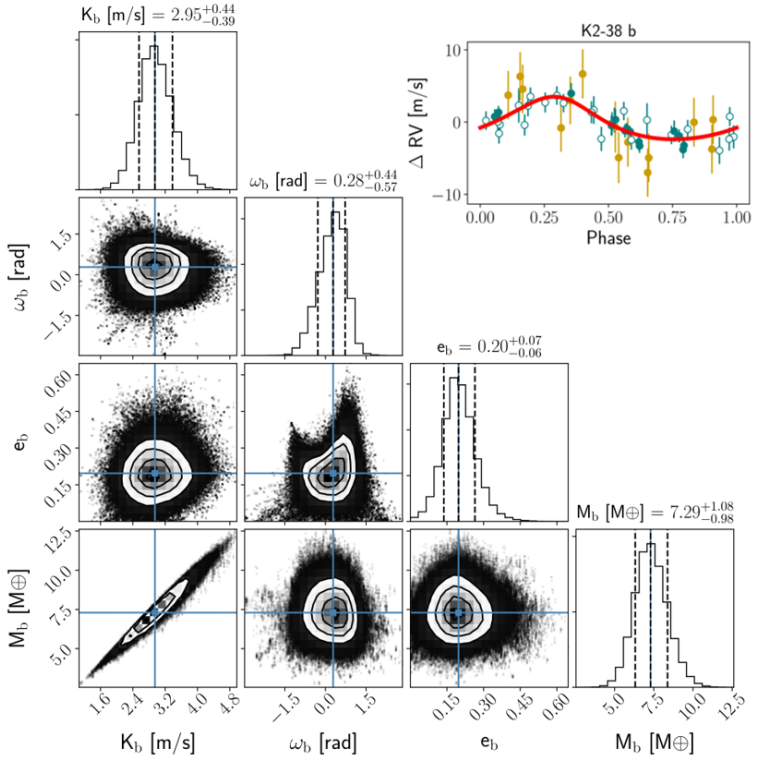

FIGURE 4.9— Corner plot of the fitted parameters associated with K2-38 b in the 2 planets model for the K2-38 RV time series. The vertical lines indicate the mean and the 16th-84th percentiles. The top right panel contains the phase-folded RV curve using the periastron time of the planet as a time reference.

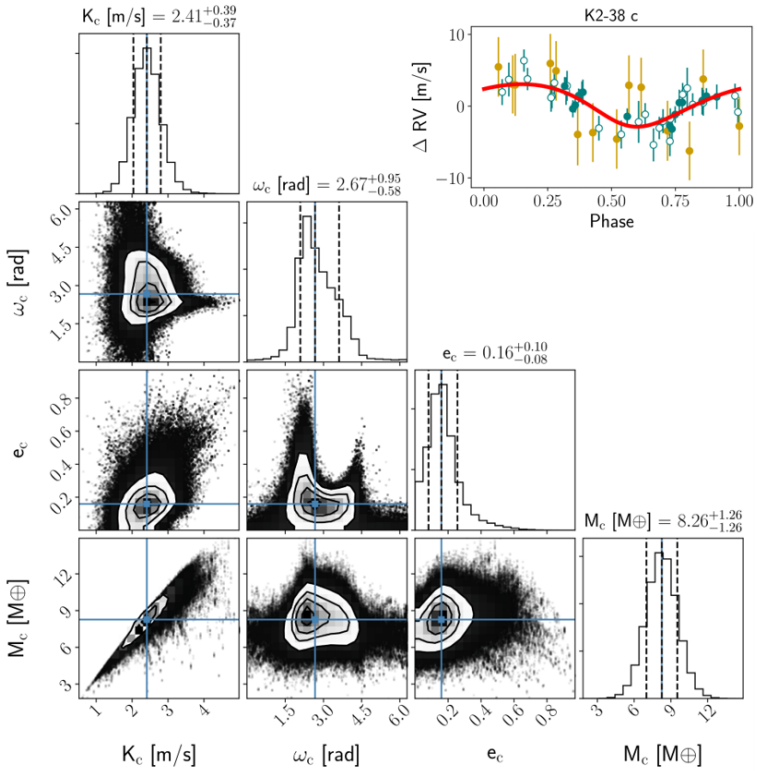

FIGURE 4.10— Corner plot of the fitted parameters associated with K2-38 c in the 2 planets model for the K2-38 RV time series. The vertical lines indicate the mean and the 16th-84th percentiles. The top right panel contains the phase-folded RV curve using the periastron time of the planet as a time reference.

The mass distributions shown in Fig. 4.9 and Fig. 4.10 were computed as:

$$M_{\rm p} = K M_\star^{2/3} P^{1/3} \frac{\sqrt{1-e^2}}{\sin i} \frac{317.8}{28.4329} M_\oplus \tag{4.2}$$

where K is the amplitude of the planetary signal, $M_\star$ is the stellar mass from Table 4.1, P is the orbital period of the planet, e is the eccentricity, and i is

the orbital inclination. This last parameter is computed from the photometric results as:

$$i = \cos^{-1}\left(\sqrt{\left(\frac{R_\star}{a}\right)^2 - \left(\frac{T_{\rm dur}\pi}{P}\right)^2}\right) \tag{4.3}$$

where $R_\star$ is the stellar radius, $T_{\rm dur}$ is the duration of the transit, and a is the semi-major axis of the planet considered. This last parameter is provided by the `exotrending` code, but it can be also calculated as:

$$a = \left(\frac{G\cdot(M_\star + M_{\rm p})\cdot P^2}{4\pi^2}\right)^{1/3} \tag{4.4}$$

We also computed the level of insolation flux received by each planet as a function of its semi-major axis and the luminosity of the star $L_\star$:

$$S = \frac{L_\star}{a^2} = \frac{4\pi R_\star^2\,\sigma T_{\rm eff}^4}{a^2} \tag{4.5}$$

along with the planetary equilibrium temperature $T_{\rm eq}$ that depends on the albedo A (energy fraction re-emitted by the planet):

$$T_{\rm eq} = \left(\frac{L_\star\cdot(1-A)}{16\pi\sigma a^2}\right)^{1/4} = T_{\rm eff}\cdot\sqrt{\frac{R_\star}{2a}}\cdot(f\cdot(1-A))^{1/4} \tag{4.6}$$

where f is a filling factor introduced to describe the atmospheric circulation of the planet (Charbonneau et al. 2005). This factor varies between f=1 (if the planet isotropically distributes the incident flux) and f=2 (if only the dayside of the planet reradiates the incident flux).

All the derived parameters from the MCMC analysis along with the ones from the K2 light curve analysis are shown in Table 4.2.

TABLE 4.2— Derived planetary parameters of K2-38 b and K2-38 c.

Parameter	K2-38 b	K2-38 c
$R_{\rm p}$ [$R_\oplus$]	1.54 ± 0.14	2.29 ± 0.26
i [deg]	$88.36\ ^{+0.17}_{-0.15}$	$87.68\ ^{+0.31}_{-0.28}$
a [AU]	$0.04994\ ^{+0.00048}_{-0.00049}$	$0.09514\ ^{+0.00091}_{-0.00094}$
Insolation Flux [$S_\oplus$]	$426\ ^{+67}_{-60}$	$117\ ^{+18}_{-16}$
$T_{\rm eq}$ [K] (*)	$1266\ ^{+44}_{-50}$	$916\ ^{+32}_{-37}$
$M_{\rm p}$ [$M_\oplus$]	$7.3\ ^{+1.1}_{-1.0}$	$8.3\ ^{+1.3}_{-1.3}$
ρ [g cm^{-3}]	$11.0\ ^{+4.1}_{-2.8}$	$3.8\ ^{+1.8}_{-1.1}$

(*) Calculated assuming null bond albedo.

As Table 4.2 shows, the MCMC analysis provides a value of $M_{\rm p} = 7.3^{+1.1}_{-1.0}$ $M_\oplus$ for K2-38 b and $M_{\rm p} = 8.3^{+1.3}_{-1.3}$ $M_\oplus$ for K2-38 c. We repeated this analysis establishing the orbital period of both planets as free parameters and recovered values of $P_{\rm b} = 4.01 \pm 0.01$ d and $P_{\rm c} = 10.56 \pm 0.04$ d that match the results from photometry. We also replaced the Keplerian terms by sinusoidal functions to fit the planetary signals with null eccentricities, which provides similar results. The RMS in the periodogram of the residuals after subtracting the two planets along with the long-term signal using the sinusoidal models (1.92 $\rm m\,s^{-1}$) is almost identical to the one obtained with the Keplerian approach (1.91 $\rm m\,s^{-1}$). Comparing the $\log Z$ values calculated from the posterior distribution of both models, we obtained $\log Z = -103.79$ for the sinusoidal fits, and $\log Z = -103.38$ for the Keplerian approach. The difference between these values indicates that both models are equally favored according to Jeffreys's interpretation of the Bayesian factor (Jeffreys 1961), with slightly better results coming from the Keplerian model, which is supported by the marginally better RMS in the residuals.

4.3.5 Discussion

Planet density and bulk composition

The mass measurements from the MCMC analysis point out to a different mass distribution with respect to those reported by Sinukoff et al. (2016), with K2-38 b being less massive than K2-38 c. This difference comes from the time-span of the ESPRESSO dataset (three times larger), its smaller error bars (almost a factor two), and the larger number of measurements in comparison with the HIRES dataset. Combining these mass measurements with the radius from the photometric transit analysis we obtained the density of both planets shown in Table 4.2. To compare these properties with the rest of the values published in the literature, we used the complete sample of confirmed planets from the NASA exoplanets archive. We selected planets with a published measure of the RV semi-amplitude (which ensures us to have mass measurements comparable with our results) and with relative uncertainties below 25 % in the following properties: orbital period, distance, inclination, radius, and mass. The $M_{\rm p} < 12\,M_\oplus$ and $R_{\rm p} < 4\,R_\oplus$ region of the resulting sample of 300 stars is shown in the mass-radius diagram of Fig. 4.11 along with four composition models from Zeng & Sasselov (2013) and two additional models that include H2 envelopes from Zeng et al. (2019).

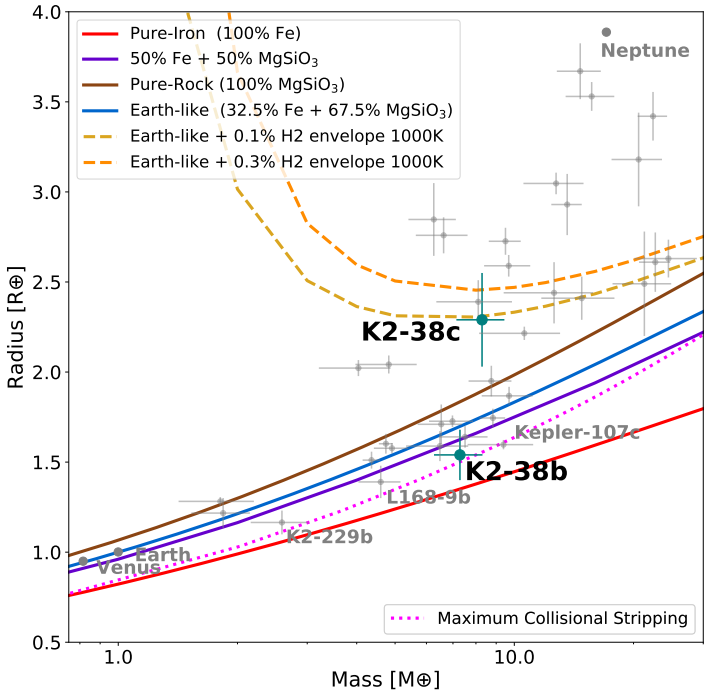

FIGURE 4.11— Radius-mass diagram including the planets from the NASA exoplanets archive with $>=4\sigma$ parameter measurements and a public RV semi-amplitude measurement. Different models are plotted: the red one denotes a 100 % Fe composition, the purple one denotes a 50 % Fe - 50 % rock composition, the blue one denotes a 32.5 % Fe - 67.5 % rock composition, the yellow and orange ones denote the same composition with a 0.1 % and 0.3 % mass percentage of H2 envelope, respectively, and the brown one denotes a rocky-type interior (composed by $MgSiO_3$). The dotted pink line indicates the minimum radius that a collision can produce for a certain planetary mass. Figure taken from Toledo-Padrón et al. (2020).

The models represented in Fig. 4.11 indicate the more probable compositions of the planets in the K2-38 system. K2-38 b is better described by a composition of 50 % Fe - 50 % rock but it is also consistent with models with higher percentages of Fe (we calculated a 67.6 % of Fe from the interior structure models computed through the wolfram tools developed by Zeng & Sasselov (2013) and Zeng et al. (2016)). These models characterize iron-rich planets like Mercury in which the presence of a mantle and a planetary magnetic field is not common. This lack of mantle could be caused by collisions during the planetary formation (Marcus et al. 2010). To explore if this phenomenon is occurring in the K2-38 system, we represented in Fig. 4.11 a collision-stripping boundary. This curve represents the minimum radius that a planet can have for a given mass if it experienced typical collisional events throughout its history. The error bars of K2-38 b fall within the boundary, making the planet compatible with this scenario. We have highlighted in Fig. 4.11 three objects with similar characteristics to K2-38 b: Kepler-107 c (Bonomo et al. 2019), L 168-9 b (Astudillo-Defru et al. 2020), and K2-229 b (Santerne et al. 2018). The hydrodynamical simulations carried for Kepler-107 c (Bonomo et al. 2019) shown how the high density of a planet can be explained through the mantle stripping caused by giant collisions. The case of K2-229 b is a good example of a Mercury analog Earth-sized planet with a very short orbital period (14 hr). The high metallicity of K2-38 could explain the formation of an iron-rich massive planet like K2-38 b in this system. The theoretical models predict the formation of iron-dominated planets in close-in orbits (Wurm et al. 2013). In the case of K2-38 c, the planet fits better within a model of 32.5 % Fe - 67.5 % rock with an H2 atmosphere of 0.1 % by mass, although the error bars make it compatible with the same envelope with a higher mass percentage (0.3 %).

To study the dependence of the density of these planets with the respective flux received from their host star, we calculated this quantity using Eq. 4.5 for two samples of exoplanets and we represented it with contours in Fig. 4.12 against the planet density and the planet size. The contours were created by binning the data and interpolating using the `scipy.ndimage` package.

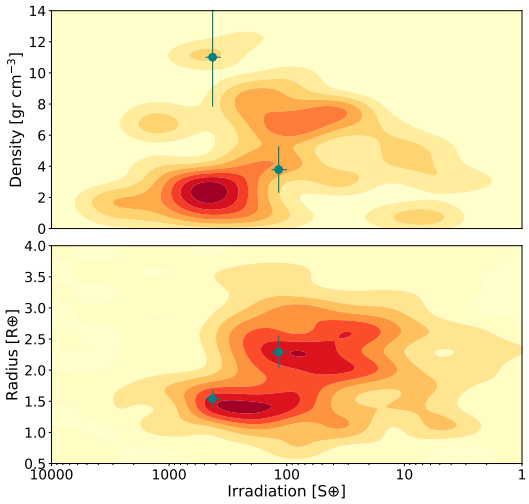

FIGURE 4.12— **Top:** Density-irradiance diagram with contours built using the exoplanets sample from Fig. 4.11. The two circle points represent the density and insolation flux of K2-38 b (left) and K2-38 c (right), respectively, with their associated error bars. **Bottom:** Radius-irradiation diagram with contours built using an exoplanet sample from NASA archive that includes all exoplanets with known radius measurements. The two circle points represent the estimated radius and insolation flux of K2-38 b (left) and K2-38 c (right), respectively, with their associated error bars. Figure taken from Toledo-Padrón et al. (2020).

The top panel of Fig. 4.12 shows that K2-38 b is among the densest planets detected to date (with a density approximately twice that of Earth), along with Kepler-107 c ($\rho_{\rm p} = 12.7 \pm 2.5$ g cm^{-3}), L 168-9 b ($\rho_{\rm p} = 9.6^{+2.4}_{-1.8}$ g cm^{-3}) and K2-229 b ($\rho_{\rm p} = 8.9 \pm 2.1$ g cm^{-3}). Our results reveal that K2-38 b is less massive than previously reported (Sinukoff et al. 2016). In the case of K2-38 c, its density is compatible with that of a sub-Neptune-like planet. The difference in density of the two planets in spite of their similar masses may suggest that, despite sharing a similar original composition at the time when the planetary system was formed, the two planets have experienced an unrelated evolution due to differing stellar irradiation and possibly to their migration histories. The maximum collision stripping from Fig. 4.11 indicates that the impacts suffered by K2-38 b could be one of the main causes of this difference.

The semi-major axis of both planets presented in Table 4.2 locates them in very close-in orbits (closer than Mercury in the Solar system), which indicates that they may be subject to evaporation effects (due to a higher insolation flux). The bottom panel of Fig. 4.12 clearly shows each of these planets located on a different side of the radius valley. The largest one (K2-38 c) is positioned above the gap, where the received flux is lower; while the smallest one (K2-38 b) is located below, where the irradiance is higher. We estimated the mass-loss rate for both planets following the procedure described in Lecavelier Des Etangs (2007). Using the semi-major axis, mass, and radius of the planets as input parameters, and assuming the UV luminosity of a G2 star, we obtained a mass loss along the life-time of the star of 0.058 ± 0.024 $M_\oplus$ for K2-38 b and 0.046 ± 0.018 $M_\oplus$ for K2-38 c. The study of planetary systems composed of a gaseous mini-Neptune and a rocky super-Earth (such as K2-38) through both spectroscopic and photometric follow-up helps to define better the limits of the radius gap of the valley. Owen & Campos Estrada (2020) provides a formalism to calculate the minimum mass of the sub-Neptune planet in this type of planetary configuration in order for the system to be consistent within a photoevaporation scenario. In our case, we obtained a minimum mass of $2.49^{+0.62}_{-0.64}$ $M_\oplus$ for K2-38 c, a threshold lower than the measured mass of this planet, which makes the K2-38 system consistent with the photoevaporation model. For the core-powered mass loss case, we relied on the formulation made by Cloutier et al. (2020). We computed a minimum mass of 7.73 $M_\oplus$ for K2-38 c, which is lower than our mass measurement, making this scenario also compatible with the masses obtained in our work.

The similarity in the mass of both planets suggests an evaporation threshold for small H/He envelopes between ~ 150 and ~ 400 times the irradiation of the Earth for a planetary mass of ~ 8 $M_\oplus$. This boundary will depend fundamentally on the spectral type of the star and also on its age. Different stellar environments will produce different evaporation rates (Fulton & Petigura 2018). In the irradiance-radius diagram of Fig. 4.12 the lack of super-Earth at high irradiances found by Lundkvist et al. (2016) is also visible. They used a large sample of detected exoplanets from the *Kepler* mission, positioning the super-Earth gap between 2.2 and 3.8 $R_\oplus$ for irradiances higher than 650 times of the insolation flux of the Earth. In our case, only the region positioned below the radius valley related to smaller planets extends to irradiances higher than 650 times the irradiance of the Earth.

Co-orbital scenario

The high density of K2-38 b makes it necessary to discard other possible scenarios that could equally explain the RV signal associated with this planet. The co-orbital case is one of the main scenarios in which a two-planet system co-orbiting at the same stellar distance would wrongly increase the planetary mass if the signal is interpreted as coming from a single Keplerian. Co-orbital configurations have not yet been confirmed outside of the Solar system although several candidates have been published (Janson 2013; Hippke & Angerhausen 2015; Lillo-Box et al. 2018; Leleu et al. 2019). As proved by Laughlin & Chambers (2002), co-orbital planet pairs are stable under relaxed conditions. Such configuration would remain long-term stable if the total mass of the planet and its co-orbital companion is smaller than 3.8 % of the mass of the star. This condition would be fulfilled by any co-orbital planetary mass for K2-38.

We explored this possibility by taking advantage of the transiting nature of the planet to apply the technique developed in Leleu et al. (2017). We modeled the radial velocity data as:

$$v(t) = \gamma + K[(\alpha - 2c)\cos(nt) - \sin(nt) + c\cos(2nt) + d\sin(2nt)] \qquad (4.7)$$

where α is proportional to the mass ratio between the co-orbital and the main planet. This allows discarding co-orbitals to a certain planetary-mass if this parameter is compatible with zero. We performed an MCMC analysis with 50 walkers and 10 000 steps per walker to explore the parameter space and study the posterior distribution of the α parameter. The model includes Eq. 4.7 for K2-38 b and Eq. 4.1 for K2-38 c. This analysis provides an α posterior characterized by $\alpha = 0.42^{+0.37}_{-0.44}$. The shift of this distribution with respect to zero is not statistically significant given its uncertainty. However, the separation from the null value ($\sim 1\sigma$) makes it impossible to reach a firm conclusion on the possible presence of co-orbitals. Additional data is thus required to narrow down the α posterior distribution in order to provide further constraints on the co-orbital scenario. From the RMS of the out-of-transit light curve, we estimated an upper limit on the co-orbital radius of $R_{\rm co} = 1.01 \pm 0.07$ R$_\oplus$ assuming a coplanar orbit. The confirmation of the $\alpha = 0.42$ would mean a reduction in the mass of the main planet due to the mass repartition between the two co-orbitals of around 30 %, placing K2-38 b in the Earth-like density regime.

Additional RV signals

Despite not finding more significant signals in the MCMC RV analysis, we added a third Keplerian to our model to search for a possible third planet. We included the new parameters without bounds using 30 000 steps for the burn-in stage and 150 000 for the construction stage, but the MCMC simulations did not converge to a clear result. We then considered possible planetary solutions that can be causing the long-term signal in the RV time series. We used the offset-corrected RV measurements after the subtraction of the two-planet model, and model the long-period signal using a sinusoidal with only the phase as a free parameter along with a constant. We calculated the amplitude of this sinusoidal using Eq. 4.2 for a certain range of masses and periods. We then computed the RMS of the residuals for all the models and represent it in the colormap of Fig. 4.13.

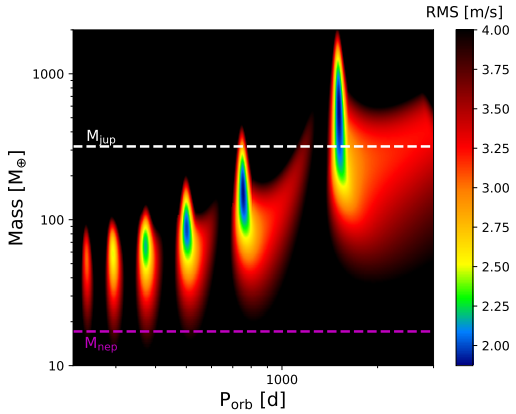

FIGURE 4.13— Distribution of the RMS of the residuals in the RV time series after subtracting the long-term signal with a sinusoidal whose amplitude is calculated from the considered values of mass and period. The horizontal white and purple dashed lines represent the Jupiter and Neptune mass, respectively. Figure taken from Toledo-Padrón et al. (2020).

The possibility of a third planet causing the long-term signal was already explored by Sinukoff et al. (2016) through an analysis of the RV acceleration using the Bayesian Information Criterion (BIC). This analysis showed that the existence of a third companion is feasible but without providing a clear mass limit. A potential companion around K2-38 was reported by Evans et al. (2018)

and Bohn et al. (2020). In the first case, the companion was identified by the *Gaia* DR2 as a background object. In the second case, the probability of this companion to be a background object was only 1.59 %, but more astrometric measurements are required to check the common proper motion. From Fig. 4.13 one can conclude that the period of the long-term signal must be within the regions of 375, 750, or 1500 d (where the residuals are minimized under a 2 m/s threshold). If this signal is caused by a planet, this would have a mass between 0.25 and 3 M_J. With more ESPRESSO RV measurements, we would be able to better constrain this signal, along with a more accurate model for the two already detected planets, which will produce changes in the distribution shown in Fig. 4.13. The Pearson coefficient (Pearson 1895) calculated between the RV of the long-period signal and the stellar activity time series of FWHM and NaD shows a possible correlation between them. This indicates that the chromospheric activity of the star could be causing this signal, although further observations are necessary to confirm it and discard a possible planetary origin.

Stellar rotation

The fact that we could not find any hint of rotation neither in photometry and spectroscopy could indicate that the star may be in a Magnetic Grand Minimum (MGM) of stellar activity (Saar & Testa 2012). If this was the case, we expect a low amplitude for the amplitude of the cycle signal, which favors the interpretation of the long-period signal as a planet. Using Eq. 3.15 we estimated an induced RV semi-amplitude lower than 0.60 $m\,s^{-1}$, which is below the RMS of the residuals after subtracting the two planets and the long-term signal. This means that it is not possible to detect the rotation signal in the RV time series until more measurements are taken. This lack of detectability is related to the low chromospheric activity of the star along with its age (older than the Sun) and intrinsic RV errors (around 1 $m\,s^{-1}$).

5

Detection of new planet candidates

If I cease searching, then, woe is me, I am lost.
That is how I look at it - keep going,
keep going come what may.
Vincent van Gogh (1853-1890)

With all the knowledge about planetary modeling and after testing it over already known exoplanets, we began the blind RV searches of previously non-reported planetary companions.

5.1 HADES and RoPES detections

The two samples of stars used to achieve this goal are the HADES and RoPES samples previously described in Sect. 3.6, which are focused on nearby stars due to their higher S/N ratio. The analysis of these samples has allowed us to detect 9 new planetary companions to 8 different stars of the programs.

The first detection reported within these programs during the course of this thesis was the discovery of the super-Earth GJ 625 b (Suárez Mascareño et al. 2017c). The spectroscopic analysis performed of this star supported by a photometric light curve from APT2 (Affer et al. 2016) lead to the detection of this planet located in the inner edge of the habitable zone. The analysis revealed the rotation signal from the star, along with the first estimation of its magnetic cycle. This star served as a testing field for all the algorithms developed for the time series computation and analysis through the GLS periodograms to test the presence of the planet.

The second publication from the HADES collaboration included a combined spectroscopic analysis of HARPS-N, HARPS, and CARMENES spectra that lead to the detection of a super-Earth orbiting the early M-dwarf GJ 3942 (Perger et al. 2017a). In this case, the rotation signal was the dominant one in the RV periodogram, with its first harmonic very close to the planetary signal, which made the detection more complicated to confirm. In this publication, we also reported a possible second planet companion in mean-motion resonance with the first and inner one.

The next paper presented the discovery of Gl 15 A c (Pinamonti et al. 2018), which is one of the exoplanets with the longest orbital period detected to date using the RV method. In this case, the progenitor star is a binary orbited by another confirmed planet (Howard et al. 2014), which makes it the second closest multi-planetary system to the Solar system. Apart from the spectroscopic analysis of the HARPS-N, HIRES, and CARMENES datasets, this paper includes an astrometric study to measure the influence of the second star in the system, providing a new orbital solution from the Lidov-Kozai interactions (Lidov 1962; Kozai 1962).

In Affer et al. (2019) we published the discovery of a super-Earth around the star of spectral sub-type M1 Gl 686. For this detection, we used 20 years of data from HARPS-N, HARPS, and HIRES, along with simultaneous photometry from ASAS, APACHE (Sozzetti et al. 2013), and APT2. In this article, we also characterized the star's magnetic cycle, as well as its rotation period.

We collaborated again with the CARMENES consortium in Perger et al. (2019) to detect and characterize a new super-Earth around the M-type star Gl 49 that presents a complex pattern of stellar activity. The consortium provided us with 3 yr of CARMENES data for this star along with new photometric data from SNO thanks to which we were able to correctly discern between the planetary signal and the chromospheric activity signals.

Our last planetary report was the case of GJ 685 b (Pinamonti et al. 2019), a massive super-Earth orbiting one of the stars with the largest RV dispersion in our sample ($6.16\,\mathrm{m\,s^{-1}}$). We based this detection on 106 HARPS-N RV measurements along with the simultaneous photometric follow-up carried out with APACHE and APT2. We also identified the rotation and the first harmonic signals in the RV time series.

From the RoPES program, we have published the discovery of two super-Earths orbiting the moderately active K-type star HD 176986 (Suárez Mascareño et al. 2018b) combining data from HARPS-N and HARPS. This star is characterized by a complex activity pattern, with the RV induced rotation signal located at 36 d. We also found a long-term signal compatible with a magnetic cycle of $\sim$6 yr. The main properties of these and the other planet

candidates are shown in Table 5.1 and their presence in the GLS periodograms is shown in Fig. 5.1.

TABLE 5.1— Planetary parameters of the HADES and RoPES reported detections.

Planet	$P_{\rm orb}$ [d]	a [AU]	$M_{\rm p} \sin i$ [$M_\oplus$]	$T_{\rm eq}$ [K] (*)
GJ 625 b	$14.628^{+0.012}_{-0.013}$	$0.078361^{+0.000044}_{-0.000046}$	2.82 ± 0.51	336 ± 21
GJ 3942 b	6.905 ± 0.040	0.0608 ± 0.0068	7.14 ± 0.59	591^{+29}_{-33}
Gl 15 A c	7600^{+2200}_{-1700}	$5.4^{+1.0}_{-0.9}$	36^{+25}_{-18}	46^{+3}_{-4}
Gl 686 b	$15.53209^{+0.00166}_{-0.00167}$	0.091 ± 0.004	7.1 ± 0.9	380^{+21}_{-26}
Gl 49 b	$13.8508^{+0.0053}_{-0.0051}$	0.0905 ± 0.0011	$5.63^{+0.67}_{-0.68}$	436^{+9}_{-10}
GJ 685 b	$24.160^{+0.061}_{-0.047}$	$0.1344^{+0.052}_{-0.051}$	$9.0^{+1.7}_{-1.8}$	369^{+17}_{-20}
HD 176986 b	6.48980 ± 0.00086	0.06296 ± 0.00013	5.74 ± 0.66	837^{+22}_{-23}
HD 176986 c	16.8191 ± 0.0044	0.11878 ± 0.00025	9.18 ± 0.97	610^{+16}_{-17}

(*) Calculated assuming null bond albedo.

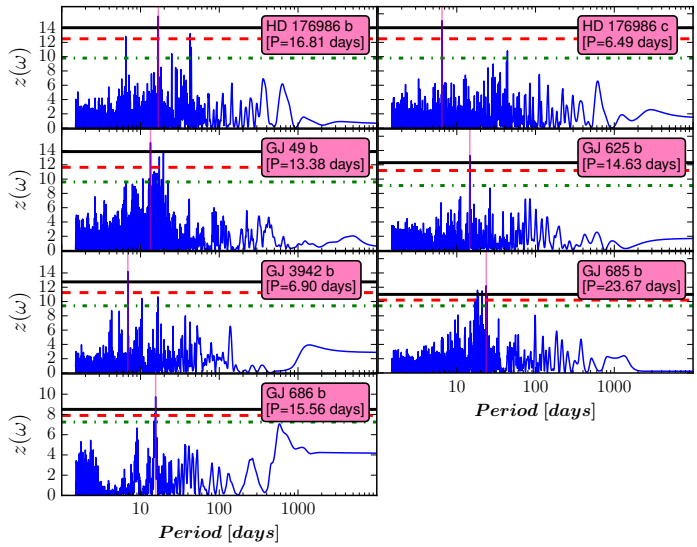

FIGURE 5.1— GLS periodograms of the RV time series from the stars within the HADES programs with short-period planetary companions reported during the course of this thesis. The green, brown, and red horizontal lines indicate the 0.1 %, 1 %, and 10 % FAP levels, respectively.

The analysis of the aforementioned stars carried out in this thesis confirmed the presence of the planets listed in Table 5.1. This is shown in Fig. 5.1, where the GLS periodograms after subtracting the activity models for the stars considered unveiled the planetary peaks. The majority of these planets present a minimum mass below the 10 $M_{\oplus}$ limit, and they are located in close-in orbits (except for Gl 15 A c). The habitability studies of GJ 625 b, Gl 686 b, and Gl 49 b revealed that depending on the considered albedo, these planets could be located close to the inner limit of the habitable zone, with equilibrium temperatures that ranged between 350 K and 380 K. The other three detections from the HADES program have been revealed as warmer (GJ 685 b and Gl 3942 b) and colder (Gl 15 A c) planets. The two planets detected in the RoPES program have been proven to be inhabitable due to the higher temperature of their host star. The orbital period distribution of all these planets is represented in Fig. 5.2 along with the habitability zone of their host star.

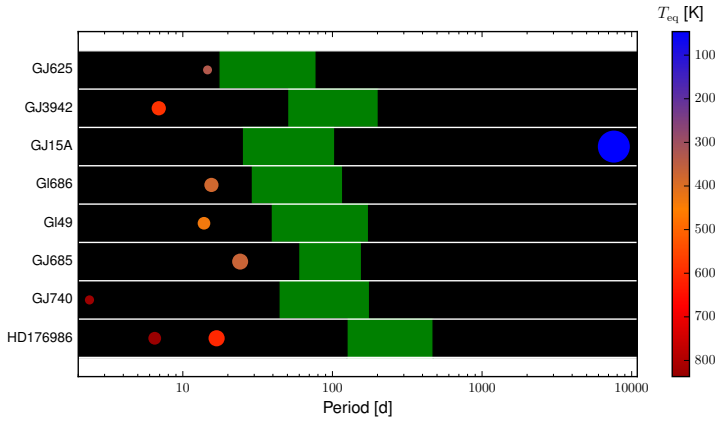

FIGURE 5.2— Orbital period distribution of the planetary discoveries within the HADES and RoPES program during the course of this thesis. The size of the planet symbols represents their mass distribution, and the color indicates their equilibrium temperature according to the color bar on the right side. The green regions represent the habitable zone of the host stars computed following Kopparapu (2013).

The six planets detected within the HADES programs add to the two planets previously discovered by the collaboration (Affer et al. 2016). The ninth and last detection from this program is one of the main results of this thesis.

5.2 The discovery of GJ 740 b

5.2.1 GJ 740

GJ 740 is a nearby (d = 11.1 pc) bright ($m_V = 9.2$) M-type (M1V) star that is included in the sample of stars from the HADES program. The search for companions of this star has produced null detections (Carson et al. 2005; Lamman et al. 2020), with only some faint field background objects reported (Carson et al. 2005). The main stellar parameters of this star are shown in Table 5.2.

TABLE 5.2— Stellar properties of GJ 740.

Parameter	GJ 740	Reference
RA (J2000)	18:58:00.14	[1]
Dec (J2000)	+05:54:29.24	[1]
$\mu_\alpha \cos\delta$ [mas yr^{-1}]	-196.301 ± 0.087	[1]
μ_δ [mas yr^{-1}]	-1220.467 ± 0.092	[1]
Distance [pc]	11.1017 ± 0.0061	[2]
m_B	10.639	[3]
m_V	9.367	[3]
Spectral type	M1V	[4]
T_{eff} [K]	3913 ± 51	[5]
$\log g$ [cgs]	4.68 ± 0.07	[5]
[Fe/H] [dex]	0.08 ± 0.16	[5]
$M_\star$ [$M_\odot$]	0.58 ± 0.06	[4]
$R_\star$ [$R_\odot$]	0.56 ± 0.06	[4]
$\log(L_\star/L_\odot)$	-1.206 ± 0.097	[4]
$\log(L_x/L_{bol})$	-4.85 ± 0.17	[6]
$v \sin i$ [km s^{-1}]	0.92 ± 0.59	[4]
i [deg]	> 25	[7]
a_{sec} [m s^{-1} yr^{-1}]	0.3903 ± 0.0005	[8]
$\log_{10}(R'_{HK})$	-4.88 ± 0.05	[9]

References: [1] Gaia Collaboration et al. (2018); [2] Bailer-Jones et al. (2018) [3] Cifuentes et al. (2020); [4] Maldonado et al. (2017); [5] Passegger et al. (2018); [6] González-Álvarez et al. (2019); [7] Suárez Mascareño et al. (2018a) ; [8] Calculated following Zechmeister et al. (2009); [9] Toledo-Padrón et al. (2021)

The previous activity studies of this star carried out by Astudillo-Defru et al. (2017a), Giacobbe et al. (2020), Díez Alonso et al. (2019), and Suárez Mascareño et al. (2018a) revealed a rotation period of 24 d, 35.6422 ± 0.0063 d, 35.20 ± 0.30 d, and 36.3 ± 1.7 d based on the analysis of 55 HARPS spectra,

765 d of APACHE photometry, 451 ASAS datapoints, and 93 HARPS-N spectra along with 53 HARPS spectra and 458 ASAS datapoints, respectively. Suárez Mascareño et al. (2018a) provided a mean level of chromospheric activity of $\log_{10}(R'_{\rm HK}) = -4.88 \pm 0.04$, along with a magnetic cycle of 2044 d detected in several stellar activity indicators. We extend this stellar activity study with new HARPS-N and CARMENES spectra in order to model the chromospheric effects on the RV measurements.

5.2.2 Data

Our HARPS-N dataset contains 129 spectra taken over a time-span of 6 years within the HADES program. This dataset is characterized by an average S/N of 110 at 5500 Å, enough to ensure a good exposure level of the blue part of the spectra where the Ca II H&K lines are located, which are especially weak for M-type stars (Giampapa et al. 1989; Lovis et al. 2011). The wavelength calibration of these spectra was provided by either a Fabry-Pérot interferometer or a ThAr lamp depending on their availability.

The HARPS dataset consists of 57 archive spectra covering a time-span of 4.3 years. The average S/N achieved in this dataset at 5500 Å is 81.5, lower than in the HARPS-N case. The wavelength solution for these spectra was computed using an FP interferometer.

The RVs of these two datasets were calculated using the TERRA (Template-Enhanced Radial velocity Re-analysis Application) reduction software (Angladа-Escudé & Butler 2012), which performs a computation similar to the one described in Sect. 2.4.1. This tool carries out a blaze, secular acceleration, barycentric velocity, and stellar RV corrections before using the highest S/N spectra to perform a template matching that provides the final RV value. We used TERRA instead of the RV calculation module developed in this thesis because TERRA yields a better mean uncertainty error, which is explained by the better performance of the TERRA pipeline for M dwarfs (Perger et al. 2017b).

In addition to the HARPS-N and HARPS datasets, we also acquired 32 CARMENES spectra across a time-span of 1.3 yr, overlapping the epoch when the HARPS-N observations were carried out. These spectra were calibrated with an FP etalon. The reduction was done using the CARACAL (CArmenes Reduction And CALibration software) pipeline (Caballero et al. 2016), and the RVs were computed using the SERVAL (SpEctrum Radial Velocity AnaLyser) tool (Zechmeister et al. 2018), which is the equivalent of the TERRA software for the CARMENES spectrograph.

The stellar activity indicators (namely Hα, $S_{\rm mw}$, NaD, and FWHM) and their errors were computed following the methodology described in Sect. 3.3.

To avoid any wavelength shifts that can affect the indices measurements, we correlated the spectra using the first spectrum taken by each spectrograph as a reference. We calibrated the Mount-Wilson S-index and modified the continuum passbands of the NaD index from the standard values as described in Sect. 3.5.4. We also studied the BIS measurements provided by the DRS pipeline, although this time series did not provide any relevant information to our general analysis.

We then removed the outliers in all of the time series that can be related to stellar flares, which are especially important in the case of active M-type stars (Reiners 2009; Hawley et al. 2014). We applied a 3σ-clipping in values and another 3σ-clipping in errors to each one of the time series, using the median value and error as a reference. For consistency, a measurement cataloged as an outlier in one of the time series is discarded in the rest of the time series. The final measurements resulting from this process are shown in Fig. 5.3 (spectroscopic time series) and Fig. 5.4 (photometric time series).

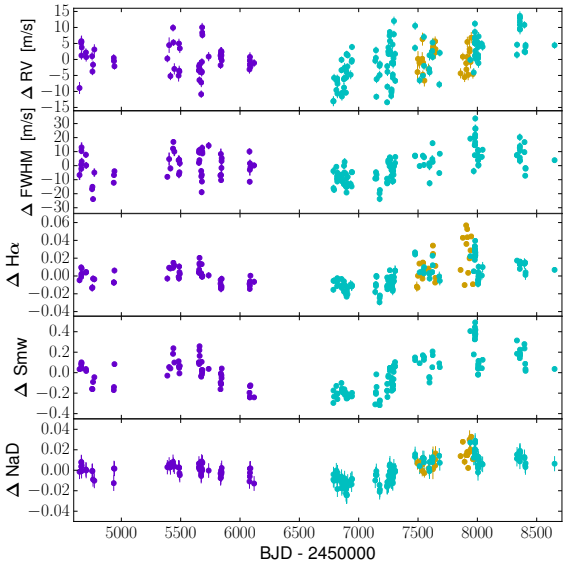

FIGURE 5.3— Time series of the RV and the activity indicators with combined measurements from HARPS (represented in violet), HARPS-N (represented in cyan), and CARMENES (represented in yellow). Figure taken from Toledo-Padrón et al. (2021).

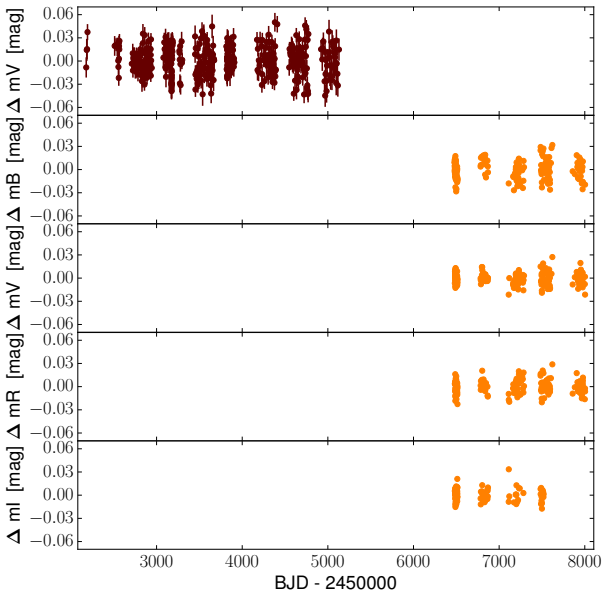

FIGURE 5.4— Time series of the photometric magnitudes taken with ASAS (represented in dark red) and EXORAP (represented in orange) in the B, V, R, and I filters. Figure taken from Toledo-Padrón et al. (2021).

The photometric datapoints shown in Fig. 5.4 come from two different surveys: ASAS and EXORAP.

The ASAS photometric measurements were obtained during a time-span of 8.1 yrs with the ASAS-S station, which is characterized by an average accuracy of ~ 0.05 mag per exposure and achieved its best results in the $V \sim 8$–12 mag range (which includes the magnitude of GJ 740). From the original 474 ASAS datapoints, we discarded 15 values labeled as low-quality data and finally made a time conversion from HJD (Heliocentric Julian Date) to BJD.

The EXORAP project is based on photometric monitoring of a broad catalog of M-type stars (including GJ 740) using the APT2 telescope from the INAF-Catania Astrophysical Observatory in Italy. For GJ 740, we count with ~ 200 photometric measurements in the B, V, R, and I bands distributed over 5 yr (in the case of the I-band data, only 100 datapoints were collected due to tech-

nical reasons). These measurements were obtained after performing a reduction process through IRAF that includes overscan and bias corrections, dark subtraction, and flat fielded (see Affer et al. 2016 for details). The errors were calculated including the intrinsic noise (photon noise and sky noise) and the RMS of the ensemble stars used for computing the differential photometry.

We also relied on the publicly available light curve from the SuperWASP database, which consists of 2350 photometric datapoints with a time-span of 2.1 yr. Similar to the ASAS dataset, this survey achieves its better performance on the $V \sim 7.0$–11.5 range and requires a time conversion from HJD to BJD. Nevertheless, the analysis of this dataset did not reveal any clear information about GJ 740, mainly because the majority of the datapoints were measured in a time-span of 130 d, with only 9 days of observations outside this range. This short time coverage does not allow to have a good characterization of the long-term behavior of the star. This problem was also encountered by Giacobbe et al. (2020) in their analysis of 81 photometric nights of GJ 740 from the APACHE survey.

5.2.3 Analysis

We first computed the GLS periodograms of all the previously mentioned time series. We show these periodograms in Fig. 5.5, marking in yellow the estimation of the stellar rotation related to the mean chromospheric activity level of $\log_{10}(R'_{\rm HK}) = -4.88 \pm 0.05$ calculated from the S-index values. All the periodograms present significant peaks around this estimation, along with two bumps at 330 d and 440 d. In the spectroscopic periodograms, the statistical significance of these signals is only exceeded by a long-period signal marked in brown in Fig. 5.5.

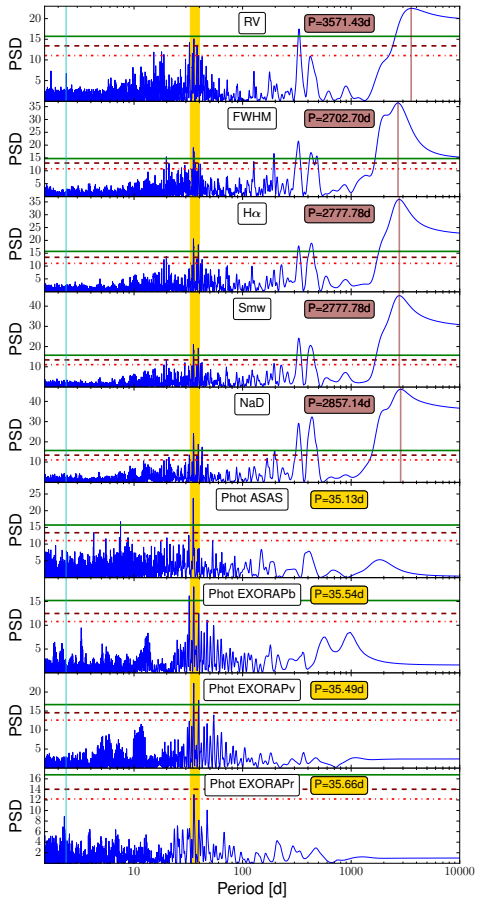

FIGURE 5.5— Periodograms of the RV, FWHM, Hα, S_{mw}, NaD, ASAS V, EXORAP B, EXORAP V, and EXORAP R-band magnitude time series. The periods related to stellar rotation, planetary companion, and possible magnetic cycle have been represented as yellow, cyan, and brown vertical lines, respectively. The green, brown, and red horizontal lines indicate the 0.1 %, 1 %, and 10 % FAP levels, respectively. Figure taken from Toledo-Padrón et al. (2021).

Long-term variation

The most significant peak in all the spectroscopic periodograms of Fig. 5.5 is related to a long-term signal with a significance much greater than the 0.1 % FAP level and whose periodicity around 8 yr makes it compatible with a magnetic cycle. This signal does not appear in the individual photometric periodograms owing to their insufficient time-coverage. The combined ASAS-EXORAP time series neither displays any significant long-term signal due to the zero-point and dispersion differences between instruments. We fitted this signal in the spectroscopic time series with a sinusoidal model that includes offset and jitter terms for each spectrograph. We first used an implementation of the Broyden–Fletcher–Goldfarb–Shanno (BFGS) algorithm (Schraudolph 2007) available in the `minimize` package from the `scipy` library to optimize the parameters of this model. Then we carried out an MCMC analysis based on the results of the BFGS algorithm using the `emcee` package. We established 10 000 steps for the burn-in stage, 50 000 steps for the construction stage, and 512 walkers to sample the parameter space, which provides the results shown in Fig. 5.6.

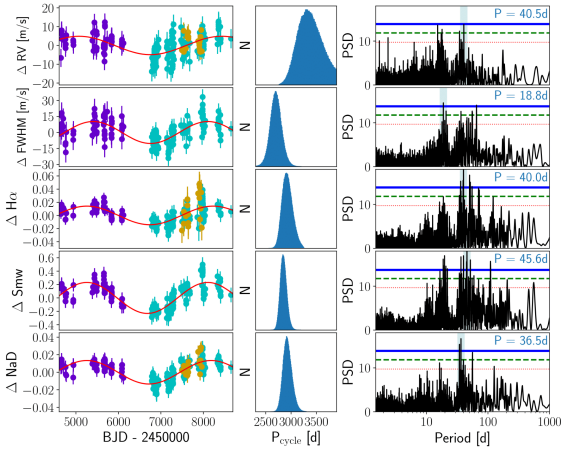

FIGURE 5.6— **Left:** RV, FWHM, Hα, S_{mw}, and NaD time series with their respective model of the long-term signal. **Center:** Posterior distribution for the periodicity of the long-term signal. **Right:** Periodograms of the residuals after subtracting the model. The blue, green, and red horizontal lines indicate the 0.1 %, 1 %, and 10 % FAP levels, respectively. The highest peak of the periodogram is marked with a blue shaded area. Figure taken from Toledo-Padrón et al. (2021).

The middle panels of Fig. 5.6 illustrate how the long-term signal in the RV time series presents a shift in periodicity with respect to the value detected in the activity indicators. The periodicity of this signal in the activity indices is around 2820 d (2701^{+110}_{-107} in FWHM, 2832^{+105}_{-94} in Hα, 2848^{+65}_{-59} in S_{mw}, and 2913^{+91}_{-81} in NaD), while in the RV time series is located at 3363^{+252}_{-215} d.

The periodograms shown in the right panels of Fig. 5.6 are related to the residuals obtained after subtracting the models represented in the left panels from each time series, applying the offset correction to all the measurements, and adding quadratically the jitter terms provided by the MCMC to the errors of each dataset. In these periodograms, the bumps at 330 d and 440 d from Fig. 5.5 have completely disappeared, which indicates that these signals were aliases of the long-term signal. The signals around 40 d related to the rotation of the star that were previously displayed in Fig. 5.5 are now the main peaks in all the spectroscopic periodograms, except for the FWHM case, where the signal related to the first harmonic of the stellar rotation shows the greatest significance.

Rotation period

We then returned to the original time series to characterize the stellar rotation through a GP regression using the quasi-periodic kernel from Eq. 3.5. We fitted the parameters of this kernel using the `celerite` code with the same setup of steps and walkers as the one previously described. We simultaneously recompute the activity cycle model previously used and obtained the parameters listed in Table 5.3 and the results shown in Fig. 5.7.

TABLE 5.3— MCMC parameters related to the long-term and rotation signals in all the time series. K_{cycle} and K_{rot} denote the amplitude of both signals, respectively.

Parameter	RV	FWHM	Hα	S_{mw}	NaD
			Long-term signal		
K_{cycle}	$4.2^{+1.1}_{-1.0}$ m s^{-1}	$8.3^{+2.3}_{-2.3}$ m s^{-1}	$0.0113^{+0.0036}_{-0.0036}$	$0.205^{+0.037}_{-0.039}$	$0.1247^{+0.0018}_{-0.0019}$
P_{cycle} [d]	3363^{+230}_{-217}	2640^{+268}_{-296}	2860^{+203}_{-204}	2849^{+178}_{-146}	2877^{+206}_{-186}
T [d]	2976^{+205}_{-182}	2860^{+134}_{-118}	2818^{+114}_{-127}	2751^{+95}_{-80}	2801^{+92}_{-76}
			Rotation signal		
K_{rot}	$4.5^{+2.0}_{-1.8}$ m s^{-1}	$7.4^{+4.3}_{-3.7}$ m s^{-1}	$0.0102^{+0.0057}_{-0.0050}$	$0.108^{+0.059}_{-0.050}$	$0.0043^{+0.0030}_{-0.0026}$
P_{rot} [d]	$18.6^{+6.0}_{-1.8}$	$36.9^{+2.0}_{-1.4}$	$36.1^{+1.9}_{-0.7}$	$37.1^{+2.0}_{-1.9}$	$36.5^{+3.0}_{-2.0}$
t_s [d]	$12.0^{+3.9}_{-1.5}$	93^{+82}_{-49}	170^{+76}_{-66}	92^{+50}_{-36}	109^{+58}_{-51}
$\log C$	-21^{+14}_{-14}	-21^{+14}_{-13}	-21^{+14}_{-14}	-21^{+14}_{-14}	-20^{+14}_{-14}

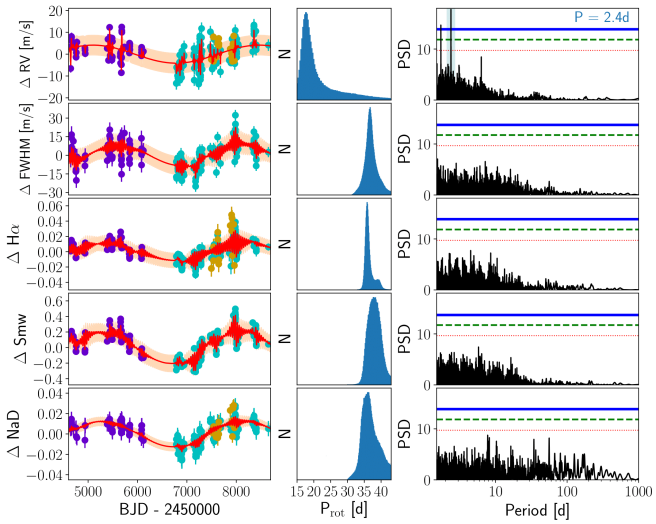

FIGURE 5.7— **Left:** RV, FWHM, Hα, S_{mw}, and NaD time series with their respective model of the long-term signal and the rotation signal. The shaded regions indicate the 1σ confidence band of the GP model. **Center:** Posterior distribution for the periodicity of the rotation signal. **Right:** Periodograms of the residuals after subtracting the model. Figure taken from Toledo-Padrón et al. (2021).

The middle panels of Fig. 5.7 show that the rotation period in the RV time series is not well-constrained, with a wide distribution that reaches its maximum peak close to the first harmonic of the stellar rotation. In the chromospheric activity-indicator time series, the rotation signal is detected with a periodicity of ~ 37 d ($36.9\,^{+2.0}_{-1.4}$ in FWHM, $36.1\,^{+1.9}_{-0.7}$ in Hα, $37.1\,^{+2.0}_{-1.9}$ in S_{mw}, and $36.5\,^{+3.0}_{-2.0}$ in NaD). The coherence time recovered from the RV kernel is much shorter than the one obtained in the rest of the time series. The fact that this parameter is a few stellar rotations in the activity indices is consistent with the evolutionary timescale of the active regions (Scandariato et al. 2017).

The Bayesian evidence $\log Z$ computed for all the time series indicates that the rotation+long-term signal model is preferred over the long-term signal model. The first model is characterized by greater $\log Z$ values in all the time series, presenting a difference greater than 30 with respect to the values computed for the second model (a difference greater than 10 already indicates

a significant preference for the model with the higher $\log Z$). This Bayesian parameter is shown in Table 5.4 for all the models considered in this work.

TABLE 5.4— $\log Z$ values computed for the different models implemented in the spectroscopic analysis of GJ 740 within their corresponding time series.

Model	RV	FWHM	Hα	S_{mw}	NaD
Cycle	−590	−632	625	141	672
Cycle+Rotation	−555	−601	683	208	721
Cycle+Rotation+Keplerian Planet	−533	···	···	···	···
Cycle+Rotation+Circular Planet	−535	···	···	···	···

Regarding the photometric time series, we previously observed in Fig. 5.5 how the ASAS dataset exhibit the same rotation signal as the one found in the chromospheric time series. The GP regression using the rotation kernel reveals a periodicity of $P_{\rm rot} = 35.60^{+0.89}_{-0.55}$ d for this signal. No additional significant signals were detected after this model was subtracted.

The pre-whitening analysis of the four EXORAP light curves revealed a similar result to the one found in the ASAS light curve. The main feature of the periodograms of the pre-whitened B and V time series is a forest of strong peaks between 20 and 60 days, which are aliases of the strongest peak at $\sim$36 days with FAP $< 0.1\,\%$. The same applies to the R-band light curve, where the 36 d period signal is characterized by FAP $\sim 1\,\%$. In the I-band all the signals are non-statistically significant (i.e., FAP $> 10\,\%$) due to the short time-span of the light curve. The MCMC analysis of the B, V, and R light curves shows that the correlated noise is consistent with the periodicity of 36 days returned by the periodograms. The combination of the posterior distributions from these time series provides an orbital period of 35.563 ± 0.071 d. The I-band light curve does not lead to any conclusive result due to its shorter time coverage with fewer data, and the expected lower amplitude of the rotation signal in this red band in comparison with the other photometric bands.

The periodograms of the stellar indices residuals in the right panels of Fig. 5.7 show that after the rotation subtraction, no more signals were detected with a statistical significance higher than the 10 % FAP level (except in the RV case). This indicates that the signals previously detected at $\sim$19 d were related to the first harmonic of the rotation period. In the case of the RV time series, we found a short-period signal of 2.4 d with a significance greater than the 0.1 % level of FAP, which could have a planetary origin since it is not present in the activity proxy time series.

Planetary signal

We explored the possible presence of a planetary signal at 2.38 d in the RV time series by adding a Keplerian component to our previous MCMC model that included the stellar rotation and long-term signal terms. The MCMC analysis provided the posterior distributions displayed in Fig. 5.8 for the Keplerian parameters of the candidate planet (we included the distribution of the derived planetary-mass computed using Eq. 4.2).

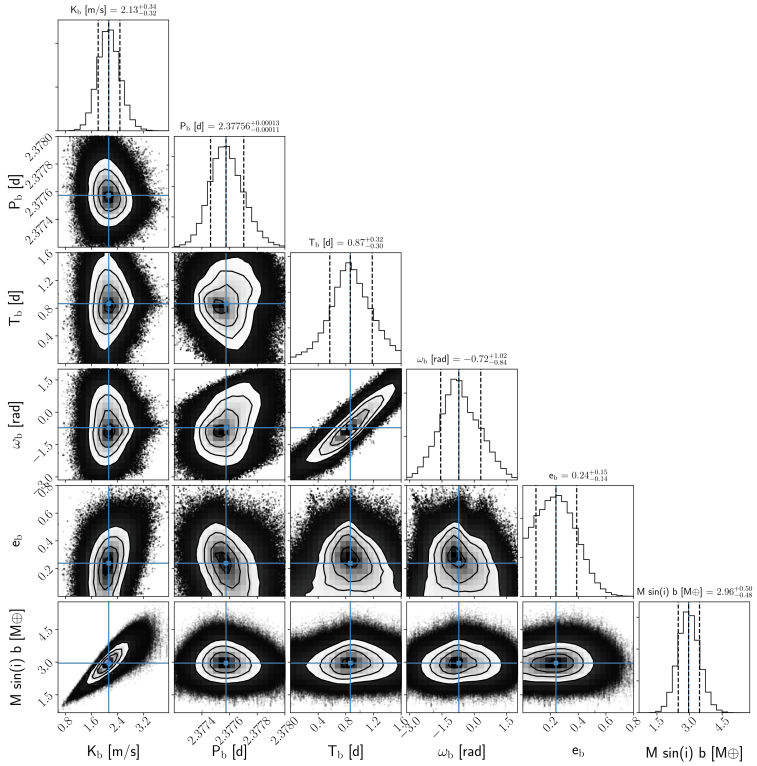

FIGURE 5.8— Posterior distributions of the GJ 740 b fitted parameters. The 16th-84th percentiles are represented through vertical dashed lines. Figure taken from Toledo-Padrón et al. (2021).

As it is shown in Fig. 5.8, we obtained a good convergence based on the autocorrelation of the chains to an orbital period of $2.37756\,^{+0.00013}_{-0.00011}$ d for GJ 740 b. As previously listed in Table 5.4, the $\log Z$ value of this model indicates a significantly better Bayesian result than the one obtained for the previous models implemented for the RV time series, with a $\Delta \log Z$ greater than 20 in favor of the planetary model. The planetary nature of this signal is further supported by the steady increase of its statistical significance and the consistency of the RV semi-amplitude with the number of measurements, which is shown in Fig. 5.9.

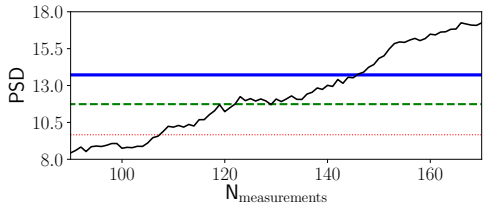

FIGURE 5.9— Evolution of the PSD associated with the planetary signal along the number of RV measurements considered. The blue, green, and red horizontal lines indicate the 0.1 %, 1 %, and 10 % FAP levels, respectively. Figure taken from Toledo-Padrón et al. (2021).

Using the orbital period of GJ 740 b and the mass of its host star from Table 5.2 we computed the planetary semi-axis through Eq. 4.4. This parameter allowed us to calculate the flux received by the planet (Eq. 4.5), its equilibrium temperature (Eq. 4.6), and the probability that the planet could transit its host star (Eq. 5.1). All these derived properties are listed in Table 5.5.

$$Transit\ Probability = \frac{R_\star + R_\mathrm{p}}{a} \simeq \frac{R_\star}{a} \tag{5.1}$$

TABLE 5.5— Derived planetary parameters of GJ 740 b.

Parameter	Value
$M_\mathrm{p} \sin$ i [$\mathrm{M}_\oplus$]	$2.96\,^{+0.50}_{-0.48}$
a [AU]	$0.029\,^{+0.001}_{-0.001}$
T_eq [K] (*)	$829\,^{+40}_{-50}$
Insolation Flux [$\mathrm{S}_\oplus$]	$79\,^{+16}_{-17}$
Transit Probability	9.0 %

Note: (*) Computed assuming null bond albedo.

The nominal eccentricity of $0.24^{+0.15}_{-0.14}$ is larger than the one expected for a short orbital period planet such as GJ 740 b, but consistent with zero at the 2σ level. For this reason, we tried an additional model using a sinusoidal function to represent the planetary signal. As it is shown in Table 5.4, this model is characterized by a Bayesian evidence slightly worse than the one related to the Keplerian model, but the difference between the two models is not enough to consider one of them more significant than the other. In Fig. 5.10 we displayed the RV time series phased to the period of the planetary signal along with the Keplerian model.

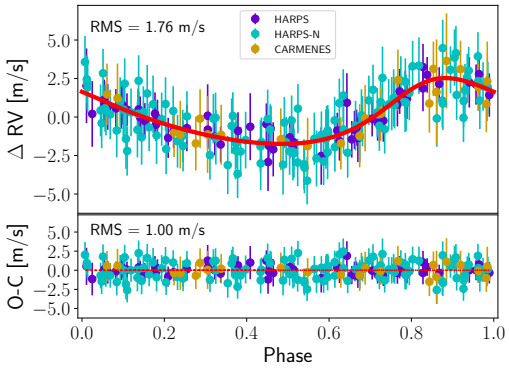

FIGURE 5.10— **Top:** Phase-folded curve of the RV time series using the GJ 740 b orbital period after subtracting the long-term signal and the rotation period. The jitter terms of each spectrograph have been added to the original RV errors. The red solid line represents the planetary model. **Bottom:** Residuals after subtracting the planetary model. Figure taken from Toledo-Padrón et al. (2021).

Figure 5.10 shows how the RV values are fitted nicely by the Keplerian model, leaving minor residuals with an RMS of $1\,\mathrm{m\,s^{-1}}$. The periodogram of these residuals shows a distribution similar to the one found in the other activity indices after subtracting the rotation and the long-term signal, with signals whose statistical significance is lower than the PSD value related to the 10 % level of FAP. We tried to track the presence of an additional planetary signal in the RV residuals by adding both a Keplerian and a sinusoidal model to our final model, but the simulations did not match the convergence criteria.

Photometric transits

Taking into account the high transit probability shown in Table 5.5, we search for the planetary signal in the photometric time series. We first computed the BoxLeastSquares (BLS) periodogram (Kovács et al. 2002) for the ASAS time series and carried out an MCMC analysis similar to the one performed in the RV time series (without modeling any long-term signal since it was not detected in photometry). The posterior distribution of the planetary parameters did not meet the convergence criteria and therefore there is no evidence of detection. The SuperWASP and EXORAP datasets do not show any hint of a short-period signal in the $P < 10$ d region with enough statistical significance to be reliable.

Additional signals

To ensure that the GP regression is not overfitting and absorbing signals not related to stellar activity, we replaced the GP rotation model with a double sinusoidal function. The periodogram of the RV residuals after subtracting this simpler model reveals the presence of a previously non-detected 15 d signal. The inclusion of an additional sinusoidal function in our MCMC model to fit this signal (along with the long-term sinusoidal, the GP rotation term, and the GJ 740 b Keplerian) provides a slightly greater $\log Z$ value than the one related to the previous model (without the short-term sinusoidal). However, the amplitude of this signal is below the 3σ significance level and its periodicity requires a narrow prior to be constrained. Additionally, this 15 d signal is also present in the Hα and S_{mw} indicators. We performed the same MCMC analysis on these time series, and we obtained a good convergence which indicates that this signal is most likely caused by stellar activity.

5.2.4 Dissertation

Activity pattern

In Suárez Mascareño et al. (2018a), the long-term signal of GJ 740 was detected in the FWHM, Hα, and S_{mw} time series with a periodicity of 2040 d and lower semi-amplitudes (2.58 m s^{-1}, 0.165, and 0.00658, respectively). The larger dataset used in our analysis produced a shift in periodicity and increased the amplitude of this signal. Although the baseline of our data is sufficient to have a good estimation of the period of the presumed magnetic cycle, the most significant long-term peak differs between the different time series. Merging the probability distribution of the FWHM, Hα, S_{mw}, and NaD datasets, we obtain a mean value of 2800 ± 150 d.

Suárez Mascareño et al. (2018a) also reported a rotation period of 38 d for GJ 740 based on the analysis of the Hα and S_{mw} time series. This analysis also showed an additional signal at $\sim$19 d related to the first harmonic which could be caused by the geometric distribution of active regions. In the FWHM time series, these two signals were detected at 35 and 18 d, respectively. The photometry analysis carried out in the article supported the detection of the rotation signal at 35 d. The average results from our analysis including new measurements and the NaD time series provide a more precise stellar rotation of 36.5 ± 1.0 d.

Regarding the photometric variability of GJ 740, the EXORAP results suggest a scenario where this variability is affected by the effects of an irregularly spotted stellar surface coupled with stellar rotation. This scenario is consistent with the greater intensity of the activity signal at bluer wavelengths, where the contrast between the photosphere and cool spots is larger. Furthermore, we notice that B and V photometry get dimmer with time, suggesting that the spot coverage increased during the observation campaign. This is consistent with an increasing level of stellar activity as also suggested by the chromospheric indices shown in Fig. 5.3.

The rotation parameters provided by the EXORAP analysis indicates that the coherence time is comparable with the stellar rotation, which contrasts with the results obtained in (Scandariato et al. 2017), where the evolutionary timescale of active regions found shows typically longer values (on the order of a few stellar rotations). This indicates that the photosphere of GJ 740 is more dynamic than what is normally found for field M dwarfs that do not belong to any stellar cluster. The decrease of the amplitude of the correlated noise with the wavelength increase suggests that the correlated signal is caused by the presence of cool spots co-rotating with the stellar surface. The stellar dimming during the observing campaign supports the scenario where the spot coverage (and the activity level) increases with time.

Planetary properties

The semi-major axis of GJ 740 b shown in Table 5.5 positions this planet in a close-in orbit to its parent star. We computed the habitable zone of GJ 740 using the methodologies published in Selsis et al. (2007) and Kopparapu (2013). The first one provides a range between 0.14 and 0.66 AU, while the second one results in a conservative range between 0.25 and 0.48 AU, and an optimistic range between 0.20 and 0.51 AU. These ranges indicate that GJ 740 b is located out of the habitable zone of its host star. The lack of a radius measurement does not allow a precise study of the composition of GJ 740 b through theoretical

models, but its mass and short orbital period suggest a rocky composition (Weiss & Marcy 2014). The eccentricity of the planet shows compatibility with a null value at 2σ (see Fig. 5.8). This has been proven to be usual for short-period Keplerian orbits (Kipping 2013) and cases similar to the one of GJ 740 b can be found in the literature (Astudillo-Defru et al. 2017b; Meléndez et al. 2017; Feng et al. 2019). To compare GJ 740 b with other detected planets around M dwarfs with measured masses we created the mass-period diagram represented in Fig. 5.11.

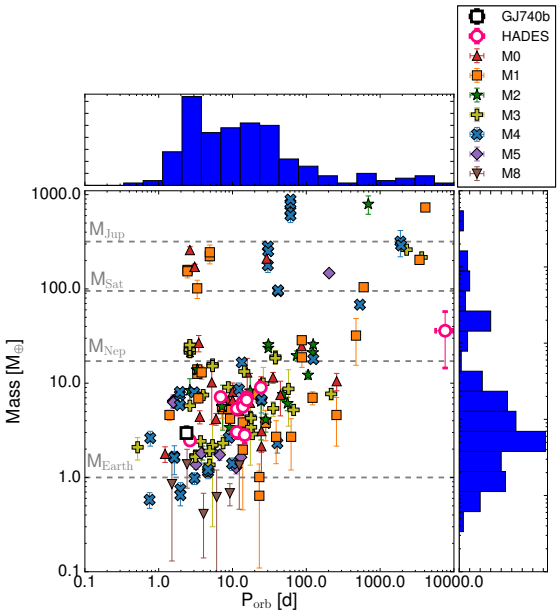

FIGURE 5.11— Mass-period diagram of the detected exoplanets from NASA exoplanets archive with published masses and orbital periods orbiting around M-type stars. The sub-spectral type of the parent star is indicated with a unique symbol and color. GJ 740 b has been represented with an unfilled black square, and the HADES detections have been marked with pink unfilled dots. The four horizontal dashed lines indicate the mass of Jupiter, Saturn, Neptune, and the Earth as a reference. The top and right panels contain the mass and orbital period distribution of the sample. Figure taken from Toledo-Padrón et al. (2021).

Figure 5.11 displays how GJ 740 b falls within the peak of the orbital period distribution and is very close to the mass peak. It is positioned as the second planet with the shortest orbital period around an M1 star after L 168-9 b (Astudillo-Defru et al. 2020). The most crowded zone in the diagram shown in Fig. 5.11 is the super-Earth region (between 2 and 10 $M_\oplus$), which contrasts with the lack of sub-Neptunes, Neptune-like, and Jovian planets detected at short periods. The diagram also shows a gap of low-mass planets with long periods due to instrument limitations.

The search for a photometric counterpart of the planetary signal caused by the transits of the planet did not reveal any match within our photometric datasets. Using the mass-radius relation for exoplanets found by Otegi et al. (2020) and assuming a density of $\rho_p > 3.3\,g\,cm^{-3}$, we estimate a radius of $1.43^{+0.12}_{-0.11}\,R_\oplus$ for GJ 740 b. Such a planetary radius implies a transit depth of 0.5 mmag, which is out of the precision range provided by the photometric instruments used in our analysis. The lack of a TESS light curve for this target precludes a deeper analysis of this possible photometric signal. Future TESS observations on this target are scheduled between 9 July and 5 August of 2022 within Sector 54. The CHEOPS telescope would be an ideal instrument to check for the occurrence of transits.

Search of a second planetary companion

The ∼3400 d signal detected in the RV time series presents a notable difference in periodicity with respect to the long-term signal detected in the activity indicators. This difference makes it difficult to discern whether the RV signal is related to the presumed activity cycle of the star or if it is caused by a second planetary companion. In the second case, the mass associated with the plausible orbital period of the planet would be ∼100 $M_\oplus$. The existence of this high-mass companion is favored by the greater statistical possibility of finding super-Earths like GJ 740 b in multi-planetary systems (Batalha et al. 2013; Ribas et al. 2018). Nevertheless, super-Earths with short orbital periods have been proven to be more likely to be on single-planetary systems than their analogs with longer orbital periods (Weiss et al. 2018), and the probability of detecting Jovian planets around M dwarfs is $< 1.27\,\%$ (Endl et al. 2006). In Fig. 5.11, only two planets with $P > 1000$ d orbiting a M1 star are shown: GJ 328 b (Robertson et al. 2013b) and GJ 832 b (Bailey et al. 2009). Both of them are Jupiter-like planets with a mass of 2.30 ± 0.13 M_{Jup} and 0.64 ± 0.06 M_{Jup}, and an orbital separation of 4.5 ± 0.2 AU and 3.4 ± 0.4 AU, respectively. Implementing a Keplerian model to trace the long-term RV signal of GJ 740 results in a not well-defined eccentricity for the model due to the long

periodicity of the signal in comparison with the time-span of the observations.

We also performed a correlation study between the RV and the stellar activity indicators to explore the possible origins of the long-term RV signal. We calculated the Pearson coefficient along with the p-value crossing all the time series for each spectrograph. We obtained a low non-significant correlation in HARPS and an intermediate significant correlation in HARPS-N, which indicates a different behavior in the stellar activity in the epoch when the HARPS-N measurements were taken. The subtraction of the S_{mw} contribution to the RV time series causes a decrease in the PSD associated with the long-term RV signal, although it maintains a FAP below the 0.1 % level. Therefore, we cannot conclude that this signal is entirely related to the stellar activity of GJ 740.

Considering that GJ 740 is bright enough to be observed by both *Gaia* and *Hipparcos*, we quantified the detection limits in a mass-separation diagram based on the proper motion difference method. Using the formalism presented in Kervella et al. (2019), we produced the diagram shown in Fig. 5.12.

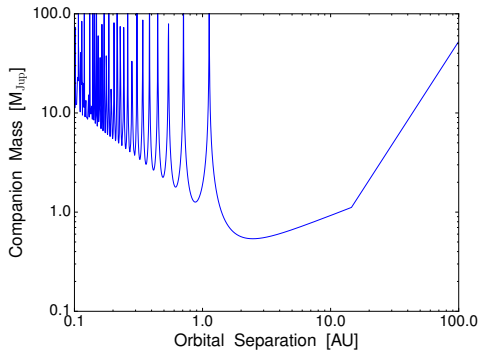

FIGURE 5.12— Diagram of the minimum mass of a planetary companion for GJ 740 at different orbital radius based on the proper motion difference technique. Figure taken from Toledo-Padrón et al. (2021).

Although there is no evidence for a statistically significant proper motion anomaly in GJ 740, Fig. 5.12 indicates that an object at 3–4 AU (encompassing the orbital period of 9.3 yr of the candidate planet) with a mass of ~ 0.6 M_{Jup} can be ruled out at the 1σ level. This means that we can place an approximate limit on the inclination of the possible companion around 30°. To acquire sensitivity to a Saturn-mass object, such as the one we might be seeing in the RV time series, we will have to wait for future *Gaia* data releases, starting with

DR3 in 2022. An improvement in mass sensitivity of a factor of 2 is likely to be achieved at the aforementioned period by combining improved calibration schemes for bright stars such as GJ 740 and more data undergoing processing.

Considering the mass of the candidate planet, the moderately old age of the system, and a favorable projected separation of ~ 0.3", this target is still out of reach for current instrumentation such as SPHERE or GPI (unless the planet is much brighter than expected, like in the case of the possible detection of Proxima Centauri c with SPHERE presented in Gratton et al. 2020). The new generation instruments at 30–40 m class telescopes presents much better perspectives for this kind of detection.

The possibility that the long-term RV signal is connected with the magnetic cycle of the star is not clear due to the uncertainties in its periodicity from all the time series and the time coverage of our dataset, which is not enough to trace two periods of the cycle. This explanation for the origin of the signal is difficult to prove if we look at the low number of M dwarfs with published and well-measured long-period cycles in the literature (Gomes da Silva et al. 2012; Savanov 2012; Robertson et al. 2013a; Toledo-Padrón et al. 2019), along with the probability that an M-dwarf that presents long-term activity variability may not present RV changes related to its magnetic cycle (Gomes da Silva et al. 2012). The peak of the cycle length for early M-type stars has been located around 6 yr (Gomes da Silva et al. 2012; Suárez Mascareño et al. 2016). The case of BD-114672, studied by Barbato et al. (2020), is a similar case to GJ 740, showing how a late K-type star with a mass similar to GJ 740 can exhibit both a long-period planet and cycle. Consequently, we conclude that the origin of the long-term RV signal is unclear until further observations are carried out.

6

Conclusions and future work

I thought up an ending for my book:
'And he lives happily ever after,
till the end of his days.'
Bilbo Baggins, The Lord of the Rings

6.1 Conclusions

Among the results produced in this thesis, we first highlight the Laser Frequency Comb (LFC) analysis described in Probst et al. (2020), for which a mastering of the calibration techniques was required. To obtain the results presented in this article, it was necessary to develop a calibration pipeline that performs all the steps necessary to obtain the wavelength solution (including line modeling, wavelength calibration, and drift computation) and the radial velocity (RV) calculation (including Cross-Correlation Function (CCF) building and Jet Propulsion Laboratory (JPL) comparison). The pipeline allows to carry out this process using two different calibration sources: the LFC and the ThAr lamp. We tested the pipeline with 9022 HARPS spectra, and studied the differences between these two sources. We observed a better performance by the LFC, with greater short-term stability and lower root-mean-square (RMS) of the residuals with respect to the theoretical solution. In comparison with the ThAr lamp, the LFC is able to account for the small physical separation between the subchips of the CCD detector. We then tested the LFC performance in terms of stellar RV precision using a sample of 179 spectra from

different target stars. By allowing the user to select between masks from different sub-spectral types within G2 and M4, the pipeline is able to provide very precise and customized RV values for the considered spectra. When comparing these results with absolute RVs provided by the JPL for 5 Solar system objects (Ceres, Herculina, Massalia, and Parthenope), we obtained a difference of $\sim 3\ \mathrm{m\,s^{-1}}$ for the dwarf planet Ceres. Currently, the calibration pipeline is designed to perform the RV calculation based on auto-built CCFs using spectra from HARPS, HARPS-N, STELLA, and HERMES.

We also highlight the stellar activity study of Barnard's Star (Toledo-Padrón et al. 2019) and the discovery of its first candidate exoplanetary companion (Ribas et al. 2018). The first article required the extension of the aforementioned pipeline with new modules to compute chromospheric activity indicators, both those related with spectral lines (Hα, S_{mw}, and NaD) and those related with CCF properties (FWHM, BIS, and CRX) for several spectrographs (HARPS, HARPS-N, CARMENES, HIRES, UVES, APF, and PFS). Considering the importance of Barnard's Star as the closest single star to our Solar system, and its previous lack of planetary companions, we exhaustively analyzed the Generalized Lomb-Scargle (GLS) periodograms of all the time series from the 964 spectra considered to discard any activity footprint in the planetary signal presented in Ribas et al. (2018). We complemented this analysis with an extensive photometric dataset of 1390 measurements coming from eight different sources (ASAS, FCAPT, RCT, SNO, AAVSO, LCO, ASH2, and MEarth). The large time-span of these spectroscopic and photometric datasets (14.5 yr and 15.1 yr, respectively) allowed us to have a good characterization of the activity cycle of the star at 3800 ± 600 d. Our computed level of chromospheric emission for this star indicates a very low level of stellar activity. We determined a stellar rotation of 145 ± 15 d, with a tentative detection of differential rotation between 130 and 180 days. This value is in good agreement with the expected rotation period predicted by the theoretical activity-rotation relations, which also predicts an upper limit to the induced RV rotation signal of $1\ \mathrm{m\,s^{-1}}$. We found no evidence that the signals detected in the time series of the chromospheric activity indicators are causing the planetary signal detected in RV.

Using the tools previously described, we have analyzed 15 000 high-resolution spectra of 57 M dwarfs from the HADES program and 25 GK-type stars from the RoPES program taken with HARPS-N and HARPS. We have measured the level of chromospheric activity of these stars and carried out a preliminary stellar activity study searching for possible planetary signals. This analysis served to cross-correlate the results published in Suárez Mascareño et al. (2018a), where we present the rotation periods and magnetic cycles detected within the

complete HADES sample, helping us to refine the activity-rotation and activity-RV semi-amplitude relations. Within the HADES collaboration, we also tested the relation between the X-ray emission and the stellar rotation for M dwarfs using the HADES sample in González-Álvarez et al. (2019).

We have explored the planetary modeling techniques by analyzing the two-planet system K2-38 with the new-generation echelle spectrograph ESPRESSO (complemented with HIRES observations) in Toledo-Padrón et al. (2020). The extreme RV precision provided by this instrument has allowed us to improve significantly the planetary parameters of the companion pair and explore the photoevaporation scenario through the photometric analysis of the available K2 light curve (supported by ASAS-SN). Through an extensive MCMC analysis we have characterized K2-38 b as a super-Earth with $R_{\rm p} = 1.54 \pm 0.14$ $R_\oplus$ and $M_{\rm p} = 7.3^{+1.1}_{-1.0}$ $M_\oplus$, and K2-38 c as a sub-Neptune with $R_{\rm p} = 2.29 \pm 0.26$ $R_\oplus$ and $M_{\rm p} = 8.3^{+1.3}_{-1.3}$ $M_\oplus$. These planets orbit their parent star at $0.04994^{+0.00048}_{-0.00049}$ AU and $0.09514^{+0.00091}_{-0.00094}$ AU, respectively, with high-inclination orbits and equilibrium temperatures of 1266^{+44}_{-50} K and 916^{+32}_{-37} K, respectively. The density of K2-38 b ($11.0^{+4.1}_{-2.8}$ g cm^{-3}) confirms this planet as one of the densest planets known to date. This density could be explained through the mantle stripping theory based on giants collisions. The composition study reveals that K2-38 b is better described by an iron-rich Mercury-like model, while K2-38 c resembles more a rocky model with an H2 envelope. According to their derived irradiances, each planet is located on a different side of the radius valley, resulting from the different irradiation levels and evaporation processes at which they are exposed, along with core-powered mass loss mechanisms. The stellar activity analysis of this star did not reveal a clear rotation signal due to its low chromospheric activity, advanced age, and intrinsic RV errors.

Our search of planetary companions within the HADES and RoPES samples led to the discovery of the super-Earth GJ 740 b published in Toledo-Padrón et al. (2021). This detection was based on a combined spectroscopic dataset from HARPS-N, HARPS, and CARMENES with a time-span of 11 yr, along with separate photometric datasets from ASAS, SuperWASP, and EXORAP. We characterized the planet with a minimum mass of $M_{\rm p} \sin i = 2.96^{+0.50}_{-0.48}$ $M_\oplus$, an orbital period of $2.37756^{+0.00013}_{-0.00011}$ d, and a transit probability of 9 %. The photometric time series did not show any significant signals around the orbital period of the planet, but the ASAS and EXORAP present a stellar rotation signal at $35.60^{+0.89}_{-0.55}$ d and 35.563 ± 0.071 d, respectively. The spectroscopic time series confirmed the rotation signal at 36.5 ± 1.0 d, and the chromospheric indices revealed the existence of a long-term activity cycle of 7.67 ± 0.41 yr. The RV time series presents hints of a possible second planetary signal at 9.3 yr

related to a Saturn-like planet of ~ 100 $M_\oplus$ that is also compatible with the presumed cycle signal at 2σ. The MCMC analysis carried out on this signal did not converge to a clear eccentricity value and its origin cannot be determined given the time-span of our current dataset.

The analysis of the complete HADES and RoPES samples helped to confirm the presence of another 8 new planetary companions around other stars from both programs. The HADES search led to the discovery of GJ 625 b (Suárez Mascareño et al. 2017c) and Gl 686 b (Affer et al. 2019), two super-Earths with orbital periods of 14.628 ± 0.013 d and $15.53209^{+0.00166}_{-0.00167}$ d and projected masses of 2.82 ± 0.51 $M_\oplus$ and 7.1 ± 0.9 $M_\oplus$, respectively, located in the inner edge of their parent star. Within the program we also discovered the super-Earth GJ 3942 b (Perger et al. 2017a), which orbits its parent star with a period of 6.905 ± 0.040 d and presents a minimum mass of 7.14 ± 0.59 $M_\oplus$, along with a possible second candidate in mean-motion resonance at 10.378 ± 0.089 d with a mass of 6.33 ± 0.50 $M_\oplus$. The analysis of the binary star Gl 15 A which is orbited by a previously reported companion (Gl 15 A b) revealed the existence of a second planet (Gl 15 A c) characterized by the one longest orbital periods detected to date (7600^{+2200}_{-1700} d) and a planetary mass of 36^{+25}_{-18} $M_\oplus$ (Pinamonti et al. 2018). Thanks to the collaboration with the CARMENES consortium (Perger et al. 2019), we were able to correctly detect and characterize the RV signal of a super-Earth ($M_\mathrm{p} \sin i = 5.63^{+0.67}_{-0.68}$ $M_\oplus$) at $13.8508^{+0.0053}_{-0.0051}$ d within the complex activity pattern of the star Gl 49. Finally, the study of the high-dispersion RV time series of GJ 685 revealed the presence of a massive super-Earth ($M_\mathrm{p} \sin i = 9.0^{+1.7}_{-1.8}$ $M_\oplus$) with an orbital period of $24.160^{+0.061}_{-0.047}$ d (Pinamonti et al. 2019). Within the RoPES program, we have detected a two-planet system around the active K2.5V star HD 176986 (Suárez Mascareño et al. 2018b), which are characterized by minimum masses of 5.74 ± 0.66 $M_\oplus$ and 9.18 ± 0.97 $M_\oplus$, and orbital periods of 6.48980 ± 0.00086 d and 16.8191 ± 0.0044 d, respectively.

6.2 Future work

In the next few months, we expect to publish two new papers within the HADES collaboration.

The first article (González-Álvarez et al. 2021) describes the discovery of a sub-Neptune companion to the M0.5V star GJ 720 A. Similar to the case of Gl 15 A, GJ 720 A has an M2.5V companion with a projected orbital separation of 112°. Our HARPS-N dataset revealed the presence of a planetary signal with a periodicity of 19.466 ± 0.005 d related to a minimum planetary mass

of 13.64 ± 0.79 $M_\oplus$. The planet would be located in the inner boundary of the habitable zone of its parent star. The stellar activity analysis is supported by photometric observations from TESS, APACHE, EXORAP, MEarth, and SuperWASP.

The second paper (Maldonado et al. 2021) includes the detection of a super-Earth with an orbital period of 18.27 ± 0.01 d and a minimum mass of 9.65 ± 1.41 $M_\oplus$ around GJ 9689 using HARPS-N. This discovery is quite challenging due to the coincidence between the periodicities of the planet and the first harmonic of the stellar rotation, which requires a careful analysis of all the considered time series.

Apart from these two papers, we will continue working on the stellar activity analysis of the HADES and RoPES samples. Especially in the RoPES sample, there are still signals susceptible to have a planetary origin. We expect to carry out new observations with HARPS and HARPS-N in order to study the evolution of the statistical significance of all these signals along with the tentative detections within the HADES sample, and discard those originated by chromospheric activity.

We will extend our analysis of Barnard's Star with new measurements from ESPRESSO. The pipeline modules oriented to the calculation of the chromospheric activity indicators and CCF properties still require some adaptation to be fully functional for this spectrograph. Once the modifications have been completed, we would make a comparison study with the results reported by the DACE pipeline using the stellar catalog selected by the ESPRESSO consortium in which the IAC is involved. This catalog contains plenty of interesting targets to be studied (especially K- and M-type stars), not only for the search of new planetary candidates but also for characterizing those already confirmed with better precision (like the case of K2-38).

From the last semester of observing campaigns, we have entered into a scientific collaboration with experts in the study of stellar activity from eight different countries. Our goal is to create a program focused on the search of super-Earths orbiting K-type stars that will allow us to extend our current catalog from the RoPES program. We are planning to search for short-period low-mass companions in planetary systems that already contain a confirmed long-period giant planet, using HARPS-N, STELLA, and FIES. Another new collaboration in which we have been recently involved is the KOFEE program, in which we aim to detect low-mass planets orbiting around a sample of 10 Mid-K (K4 to K7) stars located within 15 pc away from the Solar system.

Finally, the calibration pipeline developed in this thesis still needs to be adapted to other remarkable spectrographs such as ESPRESSO or CARMENES. We are currently working on a new drift calculation technique that is based on

measuring the shift experienced by the LFC lines with sub-pixel precision but still lacks a proper weight of the different lines involved according to their properties. Another feature that would improve the RV precision obtained is the addition of a triple Gaussian fit that models simultaneously the line considered along with the adjacent ones. The exploitation of the LFC as a calibration instrument will be key to seize the increase in RV precision that is expected from the upcoming spectrographs HARPS3, NIRPS, and ELT-HIRES. This will help us improve our activity and planetary characterization, allowing the detection of lower induced signals related to small Earth-like planets like ours.

Bibliography

Adelman, S. J., Boyd, L., Dukes, R. J., et al. 2001, IAU General Assembly

Adibekyan, V. Z., Sousa, S. G., Santos, N. C., et al. 2012, A&A, 545, A32

Adibekyan, V., Figueira, P., Santos, N. C., et al. 2015, A&A, 583, A94

Adibekyan, V., Delgado-Mena, E., Figueira, P., et al. 2016, A&A, 591, A34

Affer, L., Micela, G., Damasso, M., et al. 2016, A&A, 593, A117

Affer, L., Damasso, M., Micela, G., et al. 2019, A&A, 622, A193

Aigrain, S., Llama, J., Ceillier, T., et al. 2015, MNRAS, 450, 3211

Albrow, M., Birch, P., Caldwell, J., et al. 1996, Astrophysical Applications of Gravitational Lensing, 173, 227

Almenara, J. M., Deeg, H. J., Aigrain, S., et al. 2009, A&A, 506, 337

Alonso-Floriano, F. J., Morales, J. C., Caballero, J. A., et al. 2015, A&A, 577, A128

Ambikasaran, S., Foreman-Mackey, D., Greengard, L., et al. 2015, IEEE Transactions on Pattern Analysis and Machine Intelligence, 38, 252

Anglada-Escudé, G. & Butler, R. P. 2012, ApJS, 200, 15

Anglada-Escudé, G., Tuomi, M., Gerlach, E., et al. 2013, A&A, 556, A126

Asplund, M., Grevesse, N., Sauval, A. J., et al. 2009, Annual Review of Astron and Astrophys, 47, 481

Astudillo-Defru, N., Delfosse, X., Bonfils, X., et al. 2017, A&A, 600, A13

Astudillo-Defru, N., Forveille, T., Bonfils, X., et al. 2017, A&A, 602, A88

Astudillo-Defru, N., Cloutier, R., Wang, S. X., et al. 2020, A&A, 636, A58

Baglin, A., Auvergne, M., Boisnard, L., et al. 2006, 36th COSPAR Scientific Assembly, 36, 3749

Bailer-Jones, C. A. L., Rybizki, J., Fouesneau, M., et al. 2018, AJ, 156, 58

Bailey, J., Butler, R. P., Tinney, C. G., et al. 2009, ApJ, 690, 743

Baranne, A., Queloz, D., Mayor, M., et al. 1996, A&AS, 119, 373

Barbato, D., Pinamonti, M., Sozzetti, A., et al. 2020, A&A, 641, A68

Barnard, E. E. 1916, AJ, 29, 181

Barragán, O. & Gandolfi, D. 2017, Astrophysics Source Code Library. ascl:1706.001

Batalha, N. M., Rowe, J. F., Bryson, S. T., et al. 2013, ApJS, 204, 24

Beaulieu, J.-P., Bennett, D. P., Fouqué, P., et al. 2006, Nature, 439, 437

Berdyugina, S. V. & Järvinen, S. P. 2005, Astronomische Nachrichten, 326, 283

Berta, Z. K., Irwin, J., Charbonneau, D., et al. 2012, AJ, 144, 145

Bertran de Lis, S., Delgado Mena, E., Adibekyan, V. Z., et al. 2015, A&A, 576, A89

Beuzit, J. L., Feldt, M., Dohlen, K., et al. 2008, Proceedings of the SPIE, 7014, 701418

Bohn, A. J., Southworth, J., Ginski, C., et al. 2020, A&A, 635, A73

Boisse, I., Bouchy, F., Hébrard, G., et al. 2011, A&A, 528, A4

Bonfils, X., Mayor, M., Delfosse, X., et al. 2007, A&A, 474, 293

Bonomo, A. S., Zeng, L., Damasso, M., et al. 2019, Nature Astronomy, 3, 416

Borucki, W. J., Koch, D., Basri, G., et al. 2010, Science, 327, 977

Borucki, W. J., Koch, D. G., Basri, G., et al. 2011, ApJ, 736, 19

Bouchy, F., Pepe, F., & Queloz, D. 2001, A&A, 374, 733

Bouchy, F. & Sophie Team 2006, Tenth Anniversary of 51 Peg-b: Status of and prospects for hot Jupiter studies, 319

Bouchy, F., Doyon, R., Artigau, É., et al. 2017, The Messenger, 169, 21

Bortle, A., Fausey, H., Ji, J., et al. 2021, AJ, 161, 230

Boyajian, T. S., LaCourse, D. M., Rappaport, S. A., et al. 2016, MNRAS, 457, 3988

Bressan, A., Marigo, P., Girardi, L., et al. 2012, MNRAS, 427, 127

Brown, B. P., Oishi, J. S., Vasil, G. M., et al. 2020, ApJL, 902, L3

Browning, M. K. 2008, ApJ, 676, 1262

Bryson, S., Coughlin, J., Batalha, N. M., et al. 2020, AJ, 159, 279

Bryson, S., Kunimoto, M., Kopparapu, R. K., et al. 2021, AJ, 161, 36

Butler, R. P., Marcy, G. W., Williams, E., et al. 1996, PASP, 108, 500

Caballero, J. A., Guàrdia, J., López del Fresno, M., et al. 2016, Proceedings of the SPIE, 9910, 99100E

Campbell, B., Walker, G. A. H., & Yang, S. 1988, ApJ, 331, 902

Carlsson, M., Stein, R. F., Nordlund, Å., et al. 2004, ApJL, 610, L137

Carson, J. C., Eikenberry, S. S., Brandl, B. R., et al. 2005, AJ, 130, 1212.

Chabrier, G. & Baraffe, I. 2000, Annual Review of Astron and Astrophys, 38, 337

Chabrier, G. & Küker, M. 2006, A&A, 446, 1027

Charbonneau, D., Brown, T. M., Latham, D. W., et al. 2000, ApJL, 529, L45

Charbonneau, D., Allen, L. E., Megeath, S. T., et al. 2005, ApJ, 626, 523

Chauvin, G., Lagrange, A.-M., Dumas, C., et al. 2004, A&A, 425, L29

Chen, H. & Rogers, L. A. 2016, ApJ, 831, 180

Christensen-Dalsgaard, J. 2002, Reviews of Modern Physics, 74, 1073

Cifuentes, C., Caballero, J. A., Cortés-Contreras, M., et al. 2020, A&A, 642, A115

Claret, A. 2000, A&A, 363, 1081

Cloutier, R., Eastman, J. D., Rodriguez, J. E., et al. 2020, AJ, 160, 3

Collier Cameron, A., Bouchy, F., Hébrard, G., et al. 2007, MNRAS, 375, 951

Cosentino, R., Lovis, C., Pepe, F., et al. 2012, Proceedings of the SPIE, 8446, 84461V

Covino, E., Esposito, M., Barbieri, M., et al. 2013, A&A, 554, A28

Crane, J. D., Shectman, S. A., Butler, R. P., et al. 2010, Proceedings of the SPIE, 7735, 773553

Crossfield, I. J. M., Ciardi, D. R., Petigura, E. A., et al. 2016, ApJS, 226, 7

Cumming, A., Marcy, G. W., & Butler, R. P. 1999, ApJ, 526, 890

Cumming, A. 2004, MNRAS, 354, 1165

Cumming, A., Butler, R. P., Marcy, G. W., et al. 2008, PASP, 120, 531

Curiel, S., Ortiz-León, G. N., Mioduszewski, A. J., et al. 2020, AJ, 160, 97

da Silva, L., Girardi, L., Pasquini, L., et al. 2006, A&A, 458, 609

Dawes, W. R. 1864, MNRAS, 24, 161

Dawson, R. I. & Fabrycky, D. C. 2010, ApJ, 722, 937

Dekker, H., D'Odorico, S., Kaufer, A., et al. 2000, Proceedings of the SPIE, 4008, 534

Delisle, J.-B., Ségransan, D., Buchschacher, N., et al. 2016, A&A, 590, A134

Deubner, F.-L. 1975, A&A, 44, 371

Díaz, R. F., Cincunegui, C., & Mauas, P. J. D. 2007, MNRAS, 378, 1007

Díez Alonso, E., Caballero, J. A., Montes, D., et al. 2019, A&A, 621, A126

Di Marcantonio, P., Sosnowska, D., Cupani, G., et al. 2018, Proceedings of the SPIE, 10704, 107040F

Dorn, C., Khan, A., Heng, K., et al. 2015, A&A, 577, A83

Dravins, D. 1985, Stellar Radial Velocities, 311

Dressing, C. D. & Charbonneau, D. 2015, ApJ, 807, 45

Dumusque, X., Santos, N. C., Udry, S., et al. 2011, The Astrophysics of Planetary Systems: Formation, Structure, and Dynamical Evolution, 276, 527

Einstein, A. 1916, Annalen der Physik, 354, 769

Endl, M., Kürster, M., Els, S., et al. 2001, A&A, 374, 675

Endl, M., Cochran, W. D., Kürster, M., et al. 2006, ApJ, 649, 436

Evans, D. F., Southworth, J., Smalley, B., et al. 2018, A&A, 610, A20

Foreman-Mackey, D., Hogg, D. W., Lang, D., et al. 2013, PASP, 125, 306

Foreman-Mackey, D., Agol, E., Ambikasaran, S., et al. 2017, AJ, 154, 220

Feng, F., Crane, J. D., Xuesong Wang, S., et al. 2019, ApJS, 242, 25

Fressin, F., Torres, G., Charbonneau, D., et al. 2013, ApJ, 766, 81

Fulton, B. J., Petigura, E. A., Howard, A. W., et al. 2017, AJ, 154, 109

Fulton, B. J. & Petigura, E. A. 2018, AJ, 156, 264

Gaia Collaboration, Prusti, T., de Bruijne, J. H. J., et al. 2016, A&A, 595, A1

Gaia Collaboration, Brown, A. G. A., Vallenari, A., et al. 2018, A&A, 616, A1

Gaidos, E., Mann, A. W., Kraus, A. L., et al. 2016, MNRAS, 457, 2877

García, R. A. & Ballot, J. 2019, Living Reviews in Solar Physics, 16, 4

Gelderman, R. 2001, IAU Colloq. 183: Small Telescope Astronomy on Global Scales, 246, 89

Giacobbe, P., Benedetto, M., Damasso, M., et al. 2020, MNRAS, 491, 5216

Giampapa, M. S., Cram, L. E., & Wild, W. J. 1989, ApJ, 345, 536

Giles, H. A. C., Collier Cameron, A., & Haywood, R. D. 2017, MNRAS, 472, 1618

Goldreich, P. & Schubert, G. 1967, ApJ, 150, 571

Gomes da Silva, J., Santos, N. C., Bonfils, X., et al. 2011, A&A, 534, A30

Gomes da Silva, J., Santos, N. C., Bonfils, X., et al. 2012, A&A, 541, A9

González-Álvarez, E., Micela, G., Maldonado, J., et al. 2019, A&A, 624, A27

González-Álvarez, E., Petralia, A., Micela, G., et al. 2021

González Hernández, J. I., Pepe, F., Molaro, P., et al. 2018, Handbook of Exoplanets, 157

González Hernández, J. I., Rebolo, R., Pasquini, L., et al. 2020, A&A, 643, A146

Goodman, J. & Weare, J. 2010, Communications in Applied Mathematics and Computational Science, 5, 65

Graham, J. R., Macintosh, B., Doyon, R., et al. 2007, American Astronomical Society Meeting Abstracts

Gratton, R., Zurlo, A., Le Coroller, H., et al. 2020, A&A, 638, A120

Gustafsson, B., Edvardsson, B., Eriksson, K., et al. 2008, A&A, 486, 951

Hall, J. L., Ye, J., Diddams, S. A., et al. 2001, IEEE Journal of Quantum Electronics, 37, 1482

Hartmann, L., Soderblom, D. R., Noyes, R. W., et al. 1984, ApJ, 276, 254

Hawley, S. L., Davenport, J. R. A., Kowalski, A. F., et al. 2014, ApJ, 797, 121

Haywood, R. D., Collier Cameron, A., Queloz, D., et al. 2014, MNRAS, 443, 2517

Henden, A. A., Templeton, M., Terrell, D., et al. 2016, VizieR Online Data Catalog, II/336

Henry, G. W., Marcy, G. W., Butler, R. P., et al. 2000, ApJL, 529, L41

Herschel, W. 1801, Philosophical Transactions of the Royal Society of London Series I, 91, 265

Hippke, M. & Angerhausen, D. 2015, ApJ, 811, 1

Hirano, T., Dai, F., Gandolfi, D., et al. 2018, AJ, 155, 127

Horne, J. H. & Baliunas, S. L. 1986, ApJ, 302, 757

Houdebine, E. R., Stempels, H. C., & Oliveira, J. H. 2009, MNRAS, 400, 238

Howard, A. W., Marcy, G. W., Bryson, S. T., et al. 2012, ApJS, 201, 15

Howard, A. W., Marcy, G. W., Fischer, D. A., et al. 2014, ApJ, 794, 51

Howell, S. B., Sobeck, C., Haas, M., et al. 2014, PASP, 126, 398

Hsu, D. C., Ford, E. B., Ragozzine, D., et al. 2019, AJ, 158, 109

Janson, M. 2013, ApJ, 774, 156

Jeffreys, H. 1961, Theory of Probability, 3rd edn. (Oxford, England: Oxford University Press)

Kang, W. & Lee, S.-G. 2012, MNRAS, 425, 3162

Kennedy, G. M. & Kenyon, S. J. 2008, ApJ, 673, 502

Kervella, P., Arenou, F., Mignard, F., et al. 2019, A&A, 623, A72

Kipping, D. M. 2013, MNRAS, 434, L51

Kiraga, M. & Stepien, K. 2007, Acta Astronomica, 57, 149

Kochanek, C. S., Shappee, B. J., Stanek, K. Z., et al. 2017, PASP, 129, 104502

Koen, C., Kilkenny, D., van Wyk, F., et al. 2010, MNRAS, 403, 1949

Kopparapu, R. K. 2013, ApJL, 767, L8

Kovács, G., Zucker, S., & Mazeh, T. 2002, A&A, 391, 369

Kozai, Y. 1962, AJ, 67, 591

Kürster, M., Endl, M., Rouesnel, F., et al. 2003, A&A, 403, 1077

Kurucz, R. L. 1993, IAU Colloq. 138: Peculiar versus Normal Phenomena in A-type and Related Stars, 44, 87

Lamman, C., Baranec, C., Berta-Thompson, Z. K., et al. 2020, AJ, 159, 139

Lanza, A. F., Molaro, P., Monaco, L., et al. 2016, A&A, 587, A103

Latham, D. W., Mazeh, T., Stefanik, R. P., et al. 1989, Nature, 339, 38

Laughlin, G. & Chambers, J. E. 2002, AJ, 124, 592

Lecavelier Des Etangs, A. 2007, A&A, 461, 1185

Lee, J. W., Kim, S.-L., Kim, C.-H., et al. 2009, AJ, 137, 3181

Léger, A., Rouan, D., Schneider, J., et al. 2009, A&A, 506, 287

Leighton, R. B., Noyes, R. W., & Simon, G. W. 1962, ApJ, 135, 474

Leleu, A., Robutel, P., Correia, A. C. M., et al. 2017, A&A, 599, L7

Leleu, A., Lillo-Box, J., Sestovic, M., et al. 2019, A&A, 624, A46

Lendl, M., Csizmadia, S., Deline, A., et al. 2020, A&A, 643, A94

Lidov, M. L. 1962, Planetary Space Science, 9, 719

Lillo-Box, J., Barrado, D., Figueira, P., et al. 2018, A&A, 609, A96

Lo Curto, G., Pepe, F., Avila, G., et al. 2015, The Messenger, 162, 9

Lockwood, G. W., Skiff, B. A., Henry, G. W., et al. 2007, ApJS, 171, 260

Lomb, N. R. 1976, Ap&SS, 39, 447

Lopez, E. D. & Fortney, J. J. 2013, ApJ, 776, 2

Lovis, C., Pepe, F., Bouchy, F., et al. 2006, Proceedings of the SPIE, 6269, 62690P

Lovis, C. & Pepe, F. 2007, A&A, 468, 1115

Lovis, C., Dumusque, X., Santos, N. C., et al. 2011, arXiv:1107.5325

Luger, R., Agol, E., Kruse, E., et al. 2016, AJ, 152, 100

Lundkvist, M. S., Kjeldsen, H., Albrecht, S., et al. 2016, Nature Communications, 7, 11201

Luger, R., Kruse, E., Foreman-Mackey, D., et al. 2018, AJ, 156, 99

Maldonado, J., Scandariato, G., Stelzer, B., et al. 2017, A&A, 598, A27

Maldonado, J., Micela, G., Baratella, M., et al. 2020, A&A, 644, A68

Maldonado, J., Petralia, A., Damasso, M., et al. 2021, arXiv:2105.06155

Mandel, K. & Agol, E. 2002, ApJL, 580, L171

Marconi, A., Abreu, M., Adibekyan, V., et al. 2020, arXiv:2011.12317

Marcus, R. A., Sasselov, D., Hernquist, L., et al. 2010, ApJL, 712, L73

Marcy, G., Butler, R. P., Fischer, D., et al. 2005, Progress of Theoretical Physics Supplement, 158, 24

Markwardt, C. B. 2009, Astronomical Data Analysis Software and Systems XVIII, 411, 251

Marois, C., Macintosh, B., Barman, T., et al. 2008, Science, 322, 1348

Marois, C., Zuckerman, B., Konopacky, Q. M., et al. 2010, Nature, 468, 1080

Mathur, S., Hekker, S., Trampedach, R., et al. 2011, ApJ, 741, 119

Mayor, M. & Queloz, D. 1995, Nature, 378, 355

Mayor, M., Pepe, F., Queloz, D., et al. 2003, The Messenger, 114, 20

Meléndez, J., Bedell, M., Bean, J. L., et al. 2017, A&A, 597, A34

Meschiari, S., Wolf, A. S., Rivera, E., et al. 2009, PASP, 121, 1016

Meunier, N., Lagrange, A.-M., Borgniet, S., et al. 2015, A&A, 583, A118

Middelkoop, F. 1982, A&A, 107, 31

Molaro, P., Esposito, M., Monai, S., et al. 2013, A&A, 560, A61

Montes, D., Crespo-Chacón, I., Gálvez, M. C., et al. 2004, Lecture Notes and Essays in Astrophysics, 119

Murphy, M. T., Udem, T., Holzwarth, R., et al. 2007, MNRAS, 380, 839

Muterspaugh, M. W., Lane, B. F., Kulkarni, S. R., et al. 2010, AJ, 140, 1657

Newton, E. R., Irwin, J., Charbonneau, D., et al. 2016, ApJL, 821, L19

Newton, E. R., Irwin, J., Charbonneau, D., et al. 2016, ApJ, 821, 93

Newton, E. R., Mondrik, N., Irwin, J., et al. 2018, AJ, 156, 217

Nordlund, Å., Stein, R. F., & Asplund, M. 2009, Living Reviews in Solar Physics, 6, 2

Noyes, R. W., Hartmann, L. W., Baliunas, S. L., et al. 1984, ApJ, 279, 763

Oliva, E., Origlia, L., Maiolino, R., et al. 2004, Proceedings of the SPIE, 5492, 1274

Otegi, J. F., Bouchy, F., & Helled, R. 2020, A&A, 634, A43

Owen, J. E. & Wu, Y. 2013, ApJ, 775, 105

Owen, J. E. & Campos Estrada, B. 2020, MNRAS, 491, 5287

Pallavicini, R., Golub, L., Rosner, R., et al. 1981, ApJ, 248, 279

Passegger, V. M., Reiners, A., Jeffers, S. V., et al. 2018, A&A, 615, A6

Paulson, D. B., Allred, J. C., Anderson, R. B., et al. 2006, PASP, 118, 227

Pavlenko, Y., Suárez Mascareño, A., Rebolo, R., et al. 2017, A&A, 606, A49

Pearson, K. 1895, Proceedings of the Royal Society of London Series I, 58, 240

Pepe, F., Bouchy, F., Queloz, D., et al. 2003, Scientific Frontiers in Research on Extrasolar Planets, 294, 39

Pepe, F., Ehrenreich, D., & Meyer, M. R. 2014, Nature, 513, 358

Pepe, F., Molaro, P., Cristiani, S., et al. 2014, Astronomische Nachrichten, 335, 8

Pepe, F., Cristiani, S., Rebolo, R., et al. 2021, A&A, 645, A96

Perger, M., Ribas, I., Damasso, M., et al. 2017, A&A, 608, A63

Perger, M., García-Piquer, A., Ribas, I., et al. 2017, A&A, 598, A26

Perger, M., Scandariato, G., Ribas, I., et al. 2019, A&A, 624, A123

Perrakis, K., Ntzoufras, I., & Tsionas, E. G. 2013, arXiv:1311.0674

Perryman, M. A. C., Lindegren, L., Kovalevsky, J., et al. 1997, A&A, 500, 501

Pinamonti, M., Damasso, M., Marzari, F., et al. 2018, A&A, 617, A104

Pinamonti, M., Sozzetti, A., Giacobbe, P., et al. 2019, A&A, 625, A126

Pizzolato, N., Maggio, A., Micela, G., et al. 2003, A&A, 397, 147

Pojmanski, G. 1997, Acta Astronomica, 47, 467

Pollacco, D. L., Skillen, I., Collier Cameron, A., et al. 2006, PASP, 118, 1407

Probst, R. A., Lo Curto, G., Avila, G., et al. 2014, Proceedings of the SPIE, 9147, 91471C

Probst, R. A., Lo Curto, G., Ávila, G., et al. 2016, Proceedings of the SPIE, 9908, 990864

Probst, R. A., Milaković, D., Toledo-Padrón, B., et al. 2020, Nature Astronomy, 4, 603

Queloz, D., Mayor, M., Naef, D., et al. 2000, From Extrasolar Planets to Cosmology: The VLT Opening Symposium, 548

Queloz, D., Henry, G. W., Sivan, J. P., et al. 2001, A&A, 379, 279

Quirrenbach, A., Amado, P. J., Ribas, I., et al. 2018, Proceedings of the SPIE, 10702, 107020W

Radick, R. R., Lockwood, G. W., Skiff, B. A., et al. 1998, ApJS, 118, 239

Rainer, M., Borsa, F., & Affer, L. 2020, Experimental Astronomy, 49, 73

Rajpaul, V., Aigrain, S., Osborne, M. A., et al. 2015, MNRAS, 452, 2269

Raskin, G., van Winckel, H., Hensberge, H., et al. 2011, A&A, 526, A69

Reiners, A. & Schmitt, J. H. M. M. 2003, A&A, 398, 647

Reiners, A. 2009, A&A, 498, 853

Reiners, A., Schüssler, M., & Passegger, V. M. 2014, ApJ, 794, 144

Reinhold, T., Reiners, A., & Basri, G. 2013, A&A, 560, A4

Reinhold, T. & Gizon, L. 2015, A&A, 583, A65

Ribas, I., Tuomi, M., Reiners, A., et al. 2018, Nature, 563, 365

Ricker, G. R., Winn, J. N., Vanderspek, R., et al. 2015, Journal of Astronomical Telescopes, Instruments, and Systems, 1, 014003

Robertson, P., Endl, M., Cochran, W. D., et al. 2013, ApJ, 764, 3

Robertson, P., Endl, M., Cochran, W. D., et al. 2013, ApJ, 774, 147

Robertson, P., Mahadevan, S., Endl, M., et al. 2014, Science, 345, 440

Rodrigues, D. C., de Oliveira, P. L., Fabris, J. C., et al. 2014, MNRAS, 445, 3823

Rodrigues, T. S., Bossini, D., Miglio, A., et al. 2017, MNRAS, 467, 1433

Saar, S. H. & Testa, P. 2012, Comparative Magnetic Minima: Characterizing Quiet Times in the Sun and Stars, 286, 335

Santerne, A., Brugger, B., Armstrong, D. J., et al. 2018, Nature Astronomy, 2, 393

Santos, N. C., Adibekyan, V., Mordasini, C., et al. 2015, A&A, 580, L13

Santos, N. C., Adibekyan, V., Dorn, C., et al. 2017, A&A, 608, A94

Savanov, I. S. 2012, Astronomy Reports, 56, 716

Scandariato, G., Maldonado, J., Affer, L., et al. 2017, A&A, 598, A28

Schraudolph, N. N., Yu, J., & Günter, S. 2007, in Artificial intelligence and statistics, 436–443

Selsis, F., Kasting, J. F., Levrard, B., et al. 2007, A&A, 476, 1373

Shajn, G. & Struve, O. 1929, MNRAS, 89, 222

Shappee, B. J., Prieto, J. L., Grupe, D., et al. 2014, ApJ, 788, 48

Simon, T. & Fekel, F. C. 1987, ApJ, 316, 434

Sinukoff, E., Howard, A. W., Petigura, E. A., et al. 2016, ApJ, 827, 78

Sneden, C. A. 1973, Ph.D. Thesis

Snodgrass, H. B. & Ulrich, R. K. 1990, ApJ, 351, 309

Sousa, S. G., Santos, N. C., Israelian, G., et al. 2007, A&A, 469, 783

Sousa, S. G., Santos, N. C., Mayor, M., et al. 2008, A&A, 487, 373

Sousa, S. G. 2014, Determination of Atmospheric Parameters of B, 297

Sousa, S. G., Santos, N. C., Adibekyan, V., et al. 2015, A&A, 577, A67

Sozzetti, A., Bernagozzi, A., Bertolini, E., et al. 2013, European Physical Journal Web of Conferences, 47, 03006

Stassun, K. G., Oelkers, R. J., Pepper, J., et al. 2018, AJ, 156, 102

Stumpff, P. 1985, A&A, 144, 232

Suárez-Andrés, L., Israelian, G., González Hernández, J. I., et al. 2017, A&A, 599, A96

Suárez Mascareño, A., Rebolo, R., González Hernández, J. I., et al. 2015, MNRAS, 452, 2745

Suárez Mascareño, A., Rebolo, R., & González Hernández, J. I. 2016, A&A, 595, A12

Suárez Mascareño, A., González Hernández, J. I., Rebolo, R., et al. 2017, A&A, 597, A108

Suárez Mascareño, A., Rebolo, R., González Hernández, J. I., et al. 2017, MNRAS, 468, 4772

Suárez Mascareño, A., González Hernández, J. I., Rebolo, R., et al. 2017, A&A, 605, A92

Suárez Mascareño, A., Rebolo, R., González Hernández, J. I., et al. 2018, A&A, 612, A89

Suárez Mascareño, A., González Hernández, J. I., Rebolo, R., et al. 2018, A&A, 612, A41

Suárez Mascareño, A., Faria, J. P., Figueira, P., et al. 2020, A&A, 639, A77

Tabernero, H. M., Marfil, E., Montes, D., et al. 2019, A&A, 628, A131

Takeda, Y., Sato, B., Kambe, E., et al. 2002, Publications of the ASJ, 54, 113

Taylor, J. R. 1982, A Series of Books in Physics, Oxford: University Press, and Mill Valley: University Science Books, 1982

Thompson, S. J., Queloz, D., Baraffe, I., et al. 2016, Proceedings of the SPIE, 9908, 99086F

Toledo-Padrón, B., González Hernández, J. I., Rodríguez-López, C., et al. 2019, MNRAS, 488, 5145

Toledo-Padrón, B., Lovis, C., Suárez Mascareño, A., et al. 2020, A&A, 641, A92

Toledo-Padrón, B., Suárez Mascareño, A., González Hernández, J. I., et al. 2021, A&A, 648, A20

Torres, G., Andersen, J., & Giménez, A. 2010, Astronomy and Astrophysics Review, 18, 67

Udem, T., Holzwarth, R., & Hänsch, T. W. 2002, Nature, 416, 233

Vanderburg, A., Plavchan, P., Johnson, J. A., et al. 2016, MNRAS, 459, 3565

Vaughan, A. H., Preston, G. W., & Wilson, O. C. 1978, PASP, 90, 267

Vaughan, A. H., Baliunas, S. L., Middelkoop, F., et al. 1981, ApJ, 250, 276

Vogt, S. S. 1987, PASP, 99, 1214

Vogt, S. S., Allen, S. L., Bigelow, B. C., et al. 1994, Proceedings of the SPIE, 2198, 362

Vogt, S. S., Radovan, M., Kibrick, R., et al. 2014, PASP, 126, 359

Walter, F. M. & Bowyer, S. 1981, ApJ, 245, 671

Walter, F. M. 1996, Stellar Surface Structure, 176, 355

Wang, Y., Khardon, R., & Protopapas, P. 2012, ApJ, 756, 67

Wargelin, B. J., Saar, S. H., Pojmański, G., et al. 2017, MNRAS, 464, 3281

Weber, M., Granzer, T., & Strassmeier, K. G. 2012, Proceedings of the SPIE, 8451, 84510K

Weiss, L. M. & Marcy, G. W. 2014, ApJL, 783, L6

Weiss, L. M., Isaacson, H. T., Marcy, G. W., et al. 2018, AJ, 156, 254

Wildi, F., Pepe, F., Chazelas, B., et al. 2010, Proceedings of the SPIE, 7735, 77354X

Wilken, T., Lovis, C., Manescau, A., et al. 2010, Proceedings of the SPIE, 7735, 77350T

Wilken, T., Curto, G. L., Probst, R. A., et al. 2012, Nature, 485, 611

Winters, J. G., Henry, T. J., Lurie, J. C., et al. 2015, AJ, 149, 5

Wolszczan, A. & Frail, D. A. 1992, Nature, 355, 145

Wolszczan, A. 1994, Science, 264, 538

Wright, N. J., Drake, J. J., Mamajek, E. E., et al. 2011, ApJ, 743, 48

Wright, J. & Howard, A. 2012, Astrophysics Source Code Library. ascl:1210.031

Wright, N. J. & Drake, J. J. 2016, Nature, 535, 526

Wurm, G., Trieloff, M., & Rauer, H. 2013, ApJ, 769, 78

Zechmeister, M. & Kürster, M. 2009, A&A, 496, 577

Zechmeister, M., Kürster, M., & Endl, M. 2009, A&A, 505, 859

Zechmeister, M., Reiners, A., Amado, P. J., et al. 2018, A&A, 609, A12

Zeng, L. & Sasselov, D. 2013, PASP, 125, 227

Zeng, L., Sasselov, D. D., & Jacobsen, S. B. 2016, ApJ, 819, 127

Zeng, L., Jacobsen, S. B., Sasselov, D. D., et al. 2019, Proceedings of the National Academy of Science, 116, 9723

Agradecimientos

Y al fin he acabado mi doctorado. Estos cincos años han sido difíciles en muchos aspectos, pero aquí estoy, escribiendo lo que será el epílogo de mi tesis doctoral. Recuerdo que hace años en una clase de mi instituto nuestra profesora nos preguntó qué queríamos ser de mayor, y yo le respondí que quería ser feliz. Esa respuesta no arrojaba demasiada certidumbre sobre mi futuro laboral, así que decidí guiarme por la curiosidad que me generó de niño un pequeño libro blanco de Larousse sobre el sistema Solar que detallaba las características de los planetas que lo componían, y por la sensación de inmensidad que siempre me ha generado el ver la bóveda celeste en las noches más oscuras. El gusto por las matemáticas y el desafío que suponía aplicarlas a la Física terminaron de pavimentar el camino que me ha llevado aquí. Sin embargo no habría podido recorrerlo sin mis seres queridos y personas más cercanas que me han apoyado y ayudado a salir adelante.

Esta tesis va dedicada a mi hermano Altai. Ya no estás conmigo físicamente, pero siempre te llevaré en mi corazón todos los días de mi vida. A mis padres Juan Ángel y María del Cristo, por haber sido los mejores padres que un niño pueda desear y haber sido un apoyo fundamental frente a cualquier obstáculo que he tenido que superar. A mi abuelo Juan y mi abuela Emérita por habernos dando tantos momentos felices en el Hierro. A Nuria por haber estado siempre ahí para escucharme y apoyarme cuando más lo necesitaba. A Elena por haber pasado conmigo los momentos más difíciles y haberme ayudado a salir adelante. A Maytte por su gran corazón e inconmensurable amabilidad. A Karolina por haber compartido mil y una experiencias juntos y hacerme pasar tantos momentos inolvidables. A mi familia por siempre haber estado pendientes de mí: tia Maruca, Marce, Nely, July, Pedro Julio, Alexander, Paola, Miguel, Mariela, Manolo, Mariana, Irene, ..., os tengo siempre muy presentes. A toda la familia Jatczak por haberme acogido y haberme hecho sentir como uno más: Jarek, Ania, Maciej, Paulina, Andrzej, Marysia, ..., dziękuję bardzo. A Alejandro,

Esteban, Nuria, Sergio, Álvaro y el resto de amigos de Altai, sabéis que él estaría orgulloso de lo que habéis logrado. A mi tutor Jonay por haberme guiado durante estos cincos años y haberme incluido en tantísimos papers. A Alejandro por haber sido mi mentor y haberme resuelto tantísimas dudas. A los compañeros del máster que compartieron conmigo esta etapa de mi vida y a toda la gente increíble que he conocido gracias al IAC. A Rachelle, Mario, Matteo, Alessandro y toda la gente de Turín que me hicieron sentir como en casa. A toda la gente del Language Café por haber compartido pateos y aventuras.

A todas las bandas y artistas que me acompañaron durante mis noches de observación y mis días de programación.

A todos, gracias.

Borja Toledo Padrón